

EFFECT OF CONFINED ROLLING ON STRUCTURE-PROPERTY
RELATIONSHIPS OF Mg-Al ALLOYS

by

Pavitra Krishnan

A dissertation submitted to the faculty of
The University of North Carolina at Charlotte
in partial fulfillment of the requirements
for the degree of Doctor of Philosophy in
Mechanical Engineering

Charlotte

2021

Approved by:

Dr. Qiuming Wei

Dr. Harish Cherukuri

Dr. Youxing Chen

Dr. Laszlo Kecskes

Dr. Don Chen

ABSTRACT

PAVITRA KRISHNAN. Effect of confined rolling on structure-property relationships of Mg-Al based alloys
(Under the direction of Dr. QIUMING WEI)

High performance, light weight alloys are need-of-the particularly in the defense, automotive and aerospace sectors. Magnesium is a prime candidate since it is the lightest structural metal having a mass density of 1.74g/cm^3 and is the sixth most abundant element in the Earth's crust. But, as a metal with a Hexagonal close packed (HCP) crystal structure, it exhibits poor formability, yield asymmetry, edge cracking in rolling, and low ductility at room temperature. Activation of non-basal slip planes, suppression of twinning, and promotion of recrystallization mechanisms leading to texture randomization have been a few key strategies incorporated during alloy design to achieve better properties. In this study, the effect of thermo-mechanical processing i.e., confined rolling on three Mg-Al alloys namely AZ31B, Mg-6%Al and Mg-9%Al was analyzed. Extensive microstructural analysis using advanced electron microscopy techniques revealed the occurrence of either partial (in case of Mg-9%Al) or complete dynamic recrystallization which in turn refined the grain size, improved both strength and ductility under compression and randomized texture. Correlation of rolling temperature, strain rate, %Al content with texture, twinning, recrystallization kinetics, deformation mechanisms, precipitation kinetics and morphology have shed light on creating the best processing route for each of these alloys to achieve optimal microstructure and improved compressive mechanical behavior.

DEDICATION

To Appa, Amma, Bala, Vrushank, TKS, Pradyu and Yamini

ACKNOWLEDGEMENTS

I sincerely thank Dr. Qiuming Wei for advising my PhD work. His trust in me and the liberty he provided encouraged me to think freely. This dissertation would not have been possible without his consistent encouragement and guidance.

I would express my sincere gratitude to Dr. Laszlo J. Kecskes for being my mentor and one of the committee members. I am also thankful to Dr. Harish Cherukuri, Dr. Don Chen and Dr. Youxing Chen for being a part of my doctoral dissertation committee and providing valuable suggestions on my research. I would also extend my appreciation to Dr. Terry Xu for her valuable advice, Mr. Franklin Greene for his assistance during experimental works, Dr. Xiaoxue Chen for the fantastic research discussion and my other friends in my research group and in the department for their support and encouragement.

My sincere thanks go to the MEDE program (US-ARL) and GASP program (UNC Charlotte) for their financial support during my tenure at UNC Charlotte. Also, my thanks to Dr. KT Ramesh (JHU), Dr. Tim Weihs (JHU), Dr. Vignesh Kannan, Mr. Suhas E. Prameela and Dr. Vincent Hammond (US-ARL) for their support during my JHU visit and sharing their knowledge.

Words are not enough to express my gratitude to Dr. Zhigang Xu, Dr. Sergey Yarmolenko, Dr. Jag Sankar and Mr. Honglin Zhang from NC A&T for training, letting me use their experimental set-up and helping me with interpretation of the results.

Last but definitely not the least, I would like to express my gratefulness to my beloved parents, V.R Krishnan and Poornakala for believing in me, my husband, Balaji for his unconditional support and my lovely son Vrushank for teaching me perseverance and tenacity. Thanks for all their encouragement.

TABLE OF CONTENTS

LIST OF TABLES	x
LIST OF FIGURES	xi
LIST OF ABBREVIATIONS	xvii
CHAPTER 1: INTRODUCTION	1
1.1 History and development of Magnesium alloys	1
1.2 Physical metallurgy of Magnesium	3
1.2.1 Crystal structure	3
1.2.2 Effect of alloying	5
1.2.3 Effect of severe plastic deformation (SPD)	11
1.2.4 Dynamic recrystallization	17
1.2.5 Precipitation in Mg-Al alloys	26
1.3 SEM- EBSD studies	31
1.4 Scope and Objective of the Dissertation	35
1.5 Organization of the Dissertation	39
CHAPTER 2: EXPERIMENTAL METHODS	41
2.1 Material processing	41
2.1.1 Melting and casting of binary alloys	41
2.1.2 Solution Treatment	42
2.2 Material characterization and mechanical testing	41
2.2.1 Optical microscopy	44
2.2.2 Scanning electron microscopy (SEM)- Electron Backscattered Diffraction (EBSD)	45

2.2.3 Transmission Electron Microscopy	46
2.2.4 Mechanical testing	46
CHAPTER 3 AZ31B	52
3.1 Optical Microstructure:	52
3.2 SEM-EBSD studies	55
3.2.1 Texture	58
3.2.2. Grain Boundary Character Distribution (GBCD):	60
3.2.3 Average misorientation	61
3.3 Deformation mechanism:	62
3.3.1 Grain Orientation Spread (GOS)	62
3.3.2 DRX mechanism	64
3.3.3 The special case of confined rolling at 175°C	68
3.4 Mechanical properties under compression	69
3.4.1 Stress-strain behavior at different strain rates under compression	69
3.4.2 Strain hardening rate and coefficient	71
3.4.3 Strain Rate Sensitivity (SRS)	72
3.4.4 Fracture surface analysis under quasi-static compression	73
3.5 Chapter summary	75
CHAPTER 4: Mg-6%Al	77
4.1 Optical Microstructure	78
4.2 SEM - EBSD studies	79
4.2.1 Texture	80

4.2.2 Grain Boundary Character Distribution (GBCD)	82
4.2.3 Average Misorientation	84
4.3 Deformation mechanism	85
4.3.1 Grain Orientation Spread (GOS)	85
4.3.2 Schmid factor	87
4.3.3 DRX mechanism	90
4.4 Effect of Precipitation	92
4.4.1 Continuous and discontinuous precipitation	92
4.4.2 Particle Stimulated Nucleation and Zener pinning	96
4.4.3 Precipitate Morphology	99
4.5 Mechanical properties under compression	102
4.5.1 Stress-strain behavior at different strain rates under compression	102
4.5.2 Strain hardening rate and coefficient	103
4.5.3 Strain Rate Sensitivity (SRS)	104
4.5.4 Fracture surface analysis under quasi-static compression	105
4.6 Chapter summary	107
CHAPTER 5 Mg-9%Al	109
5.1 Optical Microstructure	109
5.2 SEM- EBSD studies	110
5.2.1 Texture	112
5.2.2 Grain Boundary Character Distribution (GBCD)	113
5.2.3 Average misorientation	114

5.2.4 Twin induced recrystallization	117
5.3 Deformation mechanism:	119
5.3.1 Grain Orientation Spread (GOS)	119
5.3.2 Schmid factor	122
5.3.3 DRX mechanism	124
5.4 Effect of Precipitation	125
5.4.1 Continuous and discontinuous precipitation	125
5.4.2 Particle Stimulated Nucleation (PSN) and Zener pinning	127
5.4.3 Precipitate Morphology	133
5.5 Mechanical properties under compression	135
5.5.1 Stress-strain behavior at different strain rates under compression	135
5.5.2 Strain hardening rate and coefficient	139
5.5.3 Strain Rate Sensitivity	139
5.5.4 Fracture surface analysis under quasi-static compression:	141
5.6 Chapter summary	143
CHAPTER 6: SUMMARY AND CONCLUDING REMARKS	144
6.1 Discussion and conclusion	144
CHAPTER 7 FUTURE WORK	152
References	153

LIST OF TABLES

Table 1.1	CRSS values of basal and non-basal slip systems of Mg-Al based alloys	5
Table 1.2	Comparison of DDRX and CDRX characteristics	21
Table 1.3	Physical properties of different canister materials	37
Table 2.1	Size of samples required for microscopy and mechanical property testing	44
Table 6.1	Comparison of average grain size of AZ31B, A6 and A9 alloys	145
Table 6.2	Comparison of average recrystallized grain size of AZ31B, A6 and A9 alloys	146
Table 6.3	Comparison of texture intensity of AZ31B, A6 and A9 alloys	146

LIST OF FIGURES

Figure 1.1:	Schematic of the HCP unit cell showing all possible slip and twin systems.	4
Figure 1.2:	Effect of temperature on the CRSS values of basal and non-basal slip systems	6
Figure 1.3	Phase diagram of Mg-Al binary phase diagram	8
Figure 1.4:	Stress-strain curves of annealed/ECAPed AZ31B compared to the same alloy processed by direct extrusion	13
Figure 1.5:	Nominal stress vs strain for cast Mg-9%Al specimens processed by HPT for 5 turns at 423K and tested at different strain rates	14
Figure 1.6:	Semi-quantitative diagram showing the variation of deformation as a function of temperature and strain	18
Figure 1.7:	Schematic diagram representing discontinuous static recrystallization (DSRX) taking place during annealing of strain hardened material	19
Figure 1.8:	Schematic diagram of continuous static recrystallization (CSRX)	19
Figure 1.9:	Schematic diagram showing the nucleation of DDRX grain	20
Figure 1.10:	Schematic diagram of deformation and dynamic recrystallization in grain boundaries	21
Figure 1.11:	Schematic diagram showing GDRX with (a) The grain boundaries flattening (b) the serrated grain boundaries becoming close; and (c) a microstructure consisting of mainly HAGBs forming	22
Figure 1.12:	Summary of various dynamic recrystallization mechanisms in a nutshell	23
Figure 1.13:	Schematic diagram showing deformation and DRX mechanisms	25
Figure 1.14	Schematic of computation of (a) GOS and (b) KAM where g and θ represent the orientation and misorientation angle respectively	33
Figure 1.15	Sample reference axes	34
Figure 1.16	(a) Schematic principle of pole figure projections and (b) orientation distribution in a highly populated pole figure	34
Figure 1.17	Inverse pole figure color key	35

Figure 2.1	Schematic of the steel permanent mold used for casting binary alloys	39
Figure 2.2	Schematic illustration of confined sample in brass tube	42
Figure 2.3	Schematic illustration of sectioning of sample from rolled samples	44
Figure 2.4	Schematic diagram of the major components of the kolsky bar system	48
Figure 2.5	Schematic diagram of the strain components in Kolsky bar system	50
Figure 3.1	Optical micrographs of AZ31B alloys (a) before rolling and after confined rolling at (b) 150°C, (c) 200°C, (d) 250°C and (e) 300°C	53
Figure 3.2	Schematic representation of microstructural evolution by necklace formation: (a) Only the parent grain is present at strain $\varepsilon < \varepsilon_c$ (b) First layer of necklace structure forms at grain boundaries (c) Second layer of necklace structure expands the recrystallization to the core of the grain (d), (e) expansion of necklace structure to consume whole interior of the grain and (f) the corresponding flow stress curve.	54
Figure 3.3	ND- Inverse Pole Figure (IPF) map of AZ31B alloys confined rolled at (a) before rolling and after confined rolling at (b) 150°C, (c) 200°C, (d) 250°C and (e) 300°C	56
Figure 3.4	Grain size measurements along ND plane of AZ31B alloy confined rolled at (a) before rolling and after confined rolling at (b) 150°C, (c) 200°C, (d) 250°C and (e) 300°C.	57
Figure 3.5	Relationship between various thermo-mechanical processing techniques with Z parameter and grain size.	58
Figure 3.6	Texture intensity of and $\{10\bar{1}0\}$ planes of AZ31B alloys (a) before and after confined rolling at (b) 150°C, (c) 200°C, (d) 250°C and (e) 300°C along ND	59
Figure 3.7	(a) Grain boundary distribution and (b) KAM distribution of AZ31B samples rolled at 200°C, 250°C and 300°C along ND	60
Figure 3.8	Misorientation angle distribution showing progressive increase and decrease of $30 \pm 5^\circ$ misorientation and $86 \pm 5^\circ$ twin boundaries respectively as rolling temperature increases.	62
Figure 3.9	(a) – (d) GOS map and (e) – (h) corresponding recrystallized area partitioned using GOS $< 5^\circ$ criterion of samples along ND rolled at 150°C, 200°C, 250°C, and 300°C respectively	63

Figure 3.10	(a), (c), (e), (g) HAGB map of AZ31B samples rolled at 150°C, 200°C, 250°C and 300°C and (b), (d), (f), (h) the corresponding line profile of misorientations along the line AB in (a)-(d) respectively along ND	65
Figure 3.11	Evidence of recrystallization inside twins (marked) in AZ31B alloys (a) extruded at 200°C and (b) confined rolled at 150°C along RD.	67
Figure 3.12	Optical micrograph (b) grain boundary distribution (c) inverse pole figures with deformed and fine DRX grains along ND of AZ31B alloys rolled at 175°C	69
Figure 3.13	(a) Quasi-static and (b) dynamic compressive behavior of AZ31B alloys rolled at different temperatures along ND	70
Figure 3.14	(a) Strain hardening rate and (b) Strain hardening coefficient of AZ31B alloy under quasi-static conditions along ND	71
Figure 3.15	Strain Rate Sensitivity (SRS) of AZ31B alloy rolled at different temperatures along ND.	73
Figure 3.16	Fracture surface SEM macro (a,c,e,g,i) and micrographs (b,d,f,h,j) of AZ31B samples confined rolled at 200°C,250°C,300°C respectively after quasi-static compression along ND	74
Figure 4.1	Optical micrographs of A6 alloys (a) before rolling and after confined rolling at (b) 200°C, (c) 250°C and (d) 300°C along ND	78
Figure 4.2	Inverse Pole Figure (IPF) map and corresponding grain size measurements along ND plane of A6 alloys confined rolled at (a)&(d) 200°C, (b)&(e) 250°C and (c)&(f) 300°C respectively.	79
Figure 4.3	(a) –(c) Texture intensity along ND of {0001} and $\{10\bar{1}0\}$ planes of A6 alloys confined rolled at (a) 200°C, (b) 250°C and (c) 300°C	81
Figure 4.4	(a) Grain boundary distribution and (b) Kernel average misorientation distribution of A6 samples rolled at 200°C,250°C and 300°C along ND	83
Figure 4.5	Misorientation angle distribution showing progressive increase of $30\pm 5^\circ$ boundaries with increase in rolling temperature	84
Figure 4.6	(a) – (c) GOS map and (d) – (f) corresponding recrystallized area along ND partitioned using GOS $< 2^\circ$ criterion of samples rolled at 200°C,250°C and 300°C respectively	86
Figure 4.7	Variation of Schmid factor with rolling temperature along ND.	87

Figure 4.8	Basal slip Schmid factor maps along ND for samples rolled at 200°C, 250°C and 300°C respectively	89
Figure 4.9	Grain boundary map along ND (a-c) and corresponding line profiles of misorientation indicated by black arrow A-B (d-f) for samples rolled at 200°C, 250°C and 300°C respectively.	92
Figure 4.10	EBSD maps along ND showing continuous and discontinuous precipitates in samples rolled at (a)200°C (b)250°C (c)300°C. Green color represents Mg ₁₇ Al ₁₂ precipitates.	94
Figure 4.11	TEM micrographs showing continuous and discontinuous precipitates in samples rolled at (a), (d) 200°C (b), (e) 250°C (c), (f) 300°C.	95
Figure 4.12	Particle stimulated nucleation observed in A6 samples rolled in bright field (a), dark field (b) and selected area diffraction (SAD) pattern (c) at 250°C and 300°C respectively	97
Figure 4.13	Variation of DRXed grain size with Zener-Hollomon parameter	99
Figure 4.14	(a)Particle structure in metals, (b) Particles having an ellipsoidal shape with rotational symmetry around RD axis and (c) drag force as a function of particle aspect ratio based on geometry given in (a)	100
Figure 4.15	Precipitate morphologies of samples rolled at 200°C,250°C and 300°C	100
Figure 4.16	(a) Recrystallized grain aspect ratio as a function of pressure ratio, q, with δ and e as variables and (b) short transverse-longitudinal section of a recrystallized grains.	101
Figure 4.17	(a) Quasi-static and (b) dynamic compressive behavior of A6 alloy rolled at different temperatures along ND	103
Figure 4.18	(a) Strain hardening rate and (b) Strain hardening coefficient of A6 alloy along ND.	104
Figure 4.19	Strain Rate Sensitivity (SRS) of A6 alloy along ND.	105
Figure 4.20	Fracture surface SEM macro (a, c, e) and micrographs (b, d, f) of A6 samples confined rolled at 200°C, 250°C and 300°C respectively after quasi-static compression along ND	106
Figure 5.1	Optical micrographs of A9 alloys (a) before rolling and after confined rolling at (b) 200°C, (c) 250°C and (d) 300°C along normal direction (ND)	110
Figure 5.2	Inverse Pole Figure (IPF) map and the corresponding grain size measurements along ND plane of A9 alloys confined rolled at (a)&(d) 200°C, (b)&(e) 250°C and (c)&(f) 300°C respectively.	111

Figure 5.3	(a) –(c) Texture intensity along the ND of {0001} and {10 $\bar{1}$ 0} planes of A9 alloys confined rolled at (a) 200°C, (b) 250°C and (c) 300°C	112
Figure 5.4	(a) Grain boundary distribution and (b) Kernel average misorientation distribution of A9 samples rolled at 200°C, 250°C and 300°C along ND	113
Figure 5.5	Misorientation angle distribution showing a progressive increase and decrease of 30 \pm 5° misorientation and 86 \pm 5° twin boundaries, respectively, as the rolling temperature increases	115
Figure 5.6	a) EBSD map showing DTWs(red), TTWs(blue), and CTWs(green); (b) evidence of recrystallization in twins and (c) grain boundary character distribution showing the twin distribution	117
Figure 5.7	KAM map showing the distribution of stored strain energy in (a), and in (b) a close-up illustration of the stored strain energy in the twinned location marked by the yellow box in (a)	118
Figure 5.8	(a) – (c) GOS map and (d) – (f) corresponding recrystallized area partitioned using GOS <2° criterion of samples rolled at 200°C,250°C and 300°C respectively	121
Figure 5.9	Variation of Schmid factor along ND with rolling temperature	122
Figure 5.10	Schmid factor maps for basal and non-basal slip systems for samples rolled at 200°C, 250°C and 300°C respectively	123
Figure 5.11	(a)-(c) HAGB map of A9 samples rolled at 200°C, 250°C and 300°C and (d) –(f) the corresponding line profile of misorientations along the line AB in (a)-(c) respectively	125
Figure 5.12	(a-c) EBSD images of continuous and discontinuous precipitation in samples rolled at (a) 200°C, (b) 250°C and (c) 300°C respectively	126
Figure 5.13	(a)-(c) LAGBs forming in contact with precipitates in samples rolled at 200°C,250°C and 300°C respectively	127
Figure 5.14	Particles pinning grain boundaries in samples rolled at (a) 250°C and (b) 300°C respectively	129
Figure 5.15	Nano-scale precipitates dispersed inside coarse deformed unrecrystallized grains at (a,b) 200°C, (c,d) 250°C, and (e,f) 300°C at higher (with SAD patterns as inset) and lower magnifications, respectively. A higher magnification was chosen for A9 samples at 300°C (c) to for visualizing precipitate morphology due to the larger precipitate sizes at that temperature.	130

Figure 5.16	Effect of particle parameters on recrystallized grain size.	133
Figure 5.17	Precipitate morphology in samples rolled at (a) 200°C, (b)250°C and (c,d) 300°C respectively	134
Figure 5.18	(a) Effective inter-particle spacing and (b) Orowan stress of various precipitate morphologies	134
Figure 5.19	(a) Quasi-static and (b) dynamic compressive behavior of A9 alloys rolled at different temperatures	137
Figure 5.20	(a) Strain hardening rate and (b) Strain hardening coefficient of A9 alloy along ND.	139
Figure 5.21	Strain Rate Sensitivity (SRS) of A9 alloy along ND.	140
Figure 5.22	Fracture surface SEM macro (a,b,d) and micrographs (c,e) of A9 alloys confined rolled at 200°C, 250°C and 300°C respectively after quasi-static compression along ND	141
Figure 6.1	Volume fraction of β - $Mg_{17}Al_{12}$ precipitates with varying Al contents in Mg-Al alloys using NMR spectroscopy	145
Figure 6.2	Typical stress-strain behavior of Mg-Al alloys as a function of %Al.	149
Figure 6.3	Typical compressive stress-strain curves of Magnesium alloys varying %Al observed in (a) literature [4] versus (b) current work at quasi-static strain rates.	150

LIST OF ABBREVIATIONS

A6	Mg-6%Al
A9	Mg-9%Al
HCP	Hexagonal close-packed
FCC	Face centered cubic
BCC	Body centered cubic
CRSS	Critical resolved shear stress
ECAE	Equal channel angular extrusion
ARB	Accumulative roll bonding
DSR	Differential speed rolling
SPD	Severe plastic deformation
SHPB	Split Hopkinson pressure bar
EDM	Electrical discharge machining
LAGB	Low angle grain boundaries
HAGB	High angle grain boundaries
SIBM	Strain induced boundary migration
DRX	Dynamic recrystallization
SRX	Static recrystallization
DSRX	Discontinuous static recrystallization
CSRX	Continuous static recrystallization
DDRX	Discontinuous dynamic recrystallization
CDRX	Continuous dynamic recrystallization
GDRX	Geometric dynamic recrystallization

TDRX	Twin dynamic recrystallization
CP	Continuous precipitation
DP	Discontinuous precipitation
OM	Optical microscopy
SEM	Scanning electron microscopy
TEM	Transmission electron microscopy
EDS	Electron dispersive spectroscopy
EBSD	Electron backscattered diffraction
QS	Quasi-static
SRS	Strain rate sensitivity

CHAPTER 1: INTRODUCTION

High performance, light weight alloys are required particularly in the automotive, aerospace, and sports industries. A lot of effort has gone into developing strong and light-weight alloys in the materials research community. Magnesium (Mg) becomes a prime candidate since it is the sixth most abundant element in the Earth's crust and lightest structural metal with a mass density of 1.74 g/cm^3 giving it high specific strength. This chapter discusses about the history and development, physical metallurgy, deformation, recrystallization and precipitation mechanisms of magnesium and its alloys. Towards the end of this chapter, the scope and objectives of this dissertation will be discussed.

1.1 History and development of magnesium alloys

Magnesium is a unique structural element which can be extracted from the hydrosphere (ocean) or the lithosphere (Earth's crust). Humphrey Davy, in 1808, first produced magnesium amalgam by electrolyzing magnesium sulphate on a Mercury cathode from which magnesium metal was distilled. Later, in 1828, Bussy produced small globules of magnesium by reducing magnesium chloride with potassium metal. It was a German scientist, named Robert W. Bunsen who demonstrated commercial production of magnesium through electrolysis by dehydrating magnesium chloride in a KCl bath in 1852. Commercial production on a larger scale was started in 1886 about the same time as the beginnings of Hall-Heroult cell process for aluminum. Molten carnallite electrolysis which is still used for its production till date was initiated by Aluminum and Magnesium Fabrik, Germany in 1886 and further developed by I.G. Farben in the twentieth century [1, 2].

WWII brought the silico-thermic reduction of magnesium oxide to the forefront. At that time, production of magnesium was almost $\frac{1^{rd}}{3}$ of that of aluminum worldwide after which the demand for it took a precipitous drop due to stringent performance requirements. Advanced steels and age hardenable aluminum alloys took precedence over magnesium alloys in a variety of applications. Due to the ever-increasing need for light weight structures, magnesium alloys became the focus of renewed research since the 1990s. Initially, research was channeled towards alloy design and development with alloying elements ranging from aluminum to more recently, rare earth (RE) elements. In parallel, efforts have turned to novel processing methods such as equal channel angular extrusion (ECAE), accumulative roll bonding (ARB), high pressure torsion (HPT) etc.[2].

Although there is an appreciable interest in the use of magnesium alloys in the automobile industry (~10-15% increase in usage per year over the past 15 years), the percentage of use in a vehicle (for example, a passenger vehicle) seems to only be around 3%. Some magnesium alloys have managed to find use in structural applications, but their use in ballistic applications has not yet been easily accepted. Hence, much scientific effort has been directed towards understanding the role of deformation mechanisms, alloying elements, fabrication processes and heat treatment for achieving optimal mechanical properties suitable for certain applications. In these upcoming sub-sections, all the above research aspects that were studied and discussed in literature by the materials community will be discussed.

1.2 Physical metallurgy of magnesium

1.2.1 Crystal structure

Magnesium has a hexagonal close packed (HCP) crystal structure with a c/a ratio of 1.62354 and a small stacking fault energy (SFE), for example, 36 ergs/cm² for the basal plane. Due to the low SFE of magnesium, activation energies of climb and cross-slip of dislocations [1, 2] are high. Also, having a lower SFE leads to a broader dislocation core width and restricted ease of dislocation motion thereby favoring twinning deformation. Thus, any attempt to impart ductility to magnesium through alloying or thermo-mechanical processing must involve an understanding of SFE and dislocation core properties. Having an HCP crystal structure, Mg doesn't meet the von-Mises criterion at room temperature. That is, it lacks at least five independent slip systems required for plastic deformation for uniform plasticity for polycrystalline aggregates, hence giving rise to mechanical anisotropy and preferred texture. Additionally, its low symmetry hinders plastic compatibility thereby inhibiting slip across the grain boundaries. A detailed explanation of various slip systems, deformation mechanisms and the reasons for lack of isotropy of magnesium alloys is provided in the upcoming sections [3].

There are six slip systems available in HCP metals : basal $\{0001\} \langle 11\bar{2}0 \rangle$, $\langle a \rangle \{10\bar{1}0\} \langle 11\bar{2}0 \rangle$, $\langle a \rangle \{10\bar{1}1\} \langle 11\bar{2}0 \rangle$, $\langle c+a \rangle \{11\bar{2}2\} \langle 11\bar{2}3 \rangle$, $\langle c \rangle \{10\bar{1}0\} \langle 0001 \rangle$ and $\langle c \rangle \{11\bar{2}0\} \langle 0001 \rangle$ as shown in fig. 1.1. The predominant slip mechanism during room temperature (RT) deformation is the basal slip. However, it provides only two independent slip systems which are insufficient for uniform plastic deformation of polycrystalline metals. Non-basal slip systems such as prismatic or pyramidal slips

either get activated at elevated temperatures or at higher stresses [4, 5]. For example, ECAE processed AZ31B samples have shown tremendous room temperature ductility (~45% [6, 7] and even 55% [7, 8]) in specific orientations but exhibit much lower ductility in other directions due to its mechanical anisotropy.

Besides deformation by slip, HCP metals also deform by deformation twinning. The relatively large interatomic distances in the magnesium lattice and the low Peierls stress between the slip planes and larger Burgers vectors facilitate twinning.

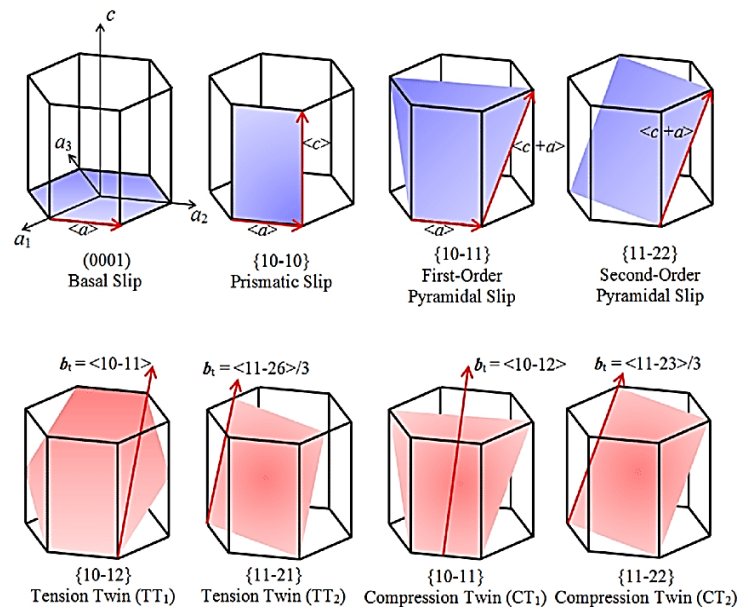


Figure 1.1: Schematic of the HCP unit cell showing all possible slip and twin systems [10].

The following twin modes $\{10\bar{1}1\}$, $\{10\bar{1}2\}$, $\{10\bar{1}3\}$, $\{10\bar{1}4\}$, $\{10\bar{1}5\}$, $\{30\bar{3}4\}$, $\{11\bar{2}1\}$ and $\{11\bar{2}4\}$ can operate in magnesium alloys [9, 10]. However, formation and growth of the commonly observed $\{10\bar{1}1\}$ extension twins lead to an extension along the c -axis and $\{10\bar{1}1\}$, $\{10\bar{1}3\}$ and $\{10\bar{1}4\}$ twins cause contraction along c -axis and hence, referred to as contraction twins. Also, secondary twin nucleation within the primary twin lamella can also accommodate large strains during deformation and is referred to as double-twinning.

There is no clarity in literature to see if twinning is detrimental or beneficial to the mechanical behavior of HCP alloys. Some researchers claim that twinning deformation is unfavorable since twin boundaries act as a barrier to slip movement in the grain structure and limit their ductility. They also suggest that twinning causes rotation of basal poles towards the loading direction resulting in rapid hardening and nonlinear mechanical response of materials [11-13]. However, few other researchers claim that mechanical twins can also result in improved mechanical properties due to grain refinement due to twin lamellae subdividing grains [13]. Table 1.1 represents the critical resolved shear stress, i.e., the component of shear stress required to initiate slip in that direction (CRSS) of various deformation modes of pure magnesium and magnesium alloys [14].

Table 1.1: CRSS values of basal and non-basal slip systems of Mg-Al based alloys

[14]

Metals	Conditions	CRSS _{basal} (Mpa)	CRSS _{twin} (Mpa)	CRSS _{prism} (Mpa)	CRSS _{twin} / CRSS _{basal}	CRSS _{prism} / CRSS _{basal}
Mg	SC	0.81 ^a ; 0.76 ^b ; 0.45 ^c ; 0.65 ^d ; 0.52 ^e	2 ^f	39.2 ^g	2.5 – 4.4	48 – 87
Mg 0.5 at. pct Zn	SC		2.7–2.8 ^h			
AZ31B	PC, VPSC, XRD	45 ⁱ	15 ⁱ	110 ⁱ	0.33 ⁱ	2.4 ⁱ
AZ31B	PC, EPSC, ND	10 ^j	30 ^j	55 ^j	3 ^j	5.5 ^j
AZ31B	PC, Taylor, XRD				2 ^k	1–2.4 ^k
AZ31B	PC, TEM					1.1 ^l
AZ31B	PC, ND, Schmid factor		25–35 ^m			
AZ61	PC, XRD					1.5–2 ⁿ
Mg 7.7 at. pct Al	PC, ND		65–75 ^o			

SC, single crystal; PC, polycrystal; XRD, X-ray diffraction; ND, neutron diffraction; VPSC, visco-plastic self-consistent model; EPSC, elasto-plastic self-consistent model; Taylor, Taylor model.

1.2.2 Effect of alloying

Several studies have indicated the effect of alloying elements either as micro or macro quantities in increasing the plasticity of Mg alloys by reducing the differences in CRSS

between slip modes or influencing twinning response within grains during deformation. Mg alloys are designated based on their alloying elements into different series based on ASTM standard alloy designation system. This comprises of four parts. For example, consider the Mg alloy, AZ61E-T6 where the first part designates the two primary alloying elements (Aluminum and Zinc in this case), second part designates the percentage of primary alloying elements (6% Al and 1% Zn in this case), third part E, differentiates alloys with the same amount of primary alloying elements and the fourth part refers to heat treatment condition of the alloy (tempered in this case). Some primary alloying elements and respective alloy designations are as follows: AZ (Aluminum-Zinc), AM (Aluminum-Manganese), AE (Aluminum- Rare earth), ZE (Zinc- Rare earth), ZK (Zinc-Zirconium) and WE (Zirconium- Rare earth) etc. [15, 16].

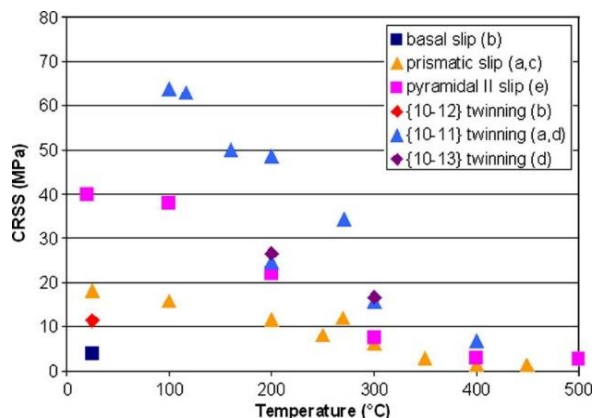


Figure 1.2 Effect of temperature on the CRSS values of basal and non-basal slip systems [17]

From table 1.1, it can be inferred that addition of alloying elements such as Al and Zn increases the CRSS of all slip/twin modes. However, it reduces the ratio between them. For instance, CRSS of basal slip (10-45 MPa) and twinning (15-35 MPa) is roughly equal whereas for pure Mg, CRSS of twinning is twice as that of basal slip. Similarly,

CRSS of prismatic slip is 1-5 times that of basal slip for AZ31B in comparison to 48-87 times in case of pure Mg. CRSS is also dependent on temperature. CRSS values obtained during channel-die compression at various temperatures is given in fig. 1.2. Previously published data suggested that the CRSS values are evidently temperature dependent going from widely distributed at RT-100°C to a narrow distribution above 350°C [17-22].

Various measures to improve formability of Mg alloys target any or combination of these factors: grain refinement, texture modification, reduction in c/a ratio, and activation of non-basal slip through alloying, severe plastic deformation, shear deformation methods, etc. Alloying with elements such as Li, Ca, Y, Gd, Ce, Nd, La and Sm has shown to improve ductility by modification of c/a ratio [21-23]. Addition of RE elements have been reported to modify the texture of Mg alloys by promoting non-basal slip during deformation retarding dynamic recovery and recrystallization processes and promoting the growth of non-basal oriented grains. [24]. However, the role of non-RE alloying elements such as Al, Zn, Mn in the formation of initial deformation texture is not completely understood. Additionally, alloying also helps in modification of texture by modifying deformation behavior especially, the twinning response [25-28].

Addition of aluminum (Al) promotes the formation of the β -Mg₁₇Al₁₂ phase. This intermetallic phase which forms at higher concentration of aluminum affects formability by weakening basal texture through pinning of grain boundaries and resisting the movement of twin boundaries. Hence, alloys with higher concentration of Al are most preferred for engineering applications [29, 30]. The effect of Al addition

on the formability of various AM alloys was studied by Huang et al. It was observed that alloys with higher concentration of Al (>6%) improved strength while lower concentrations of Al (<6%) improved in formability and exhibited weak texture [31]. Fig. 1.3 shows the binary Mg-Al phase diagram. The melting point of pure Mg is 650°C and pure Al is 660.45°C. Due to the relative atomic radii of Al and Mg atoms (ratio of radius of Al to Mg is 1.12), suggesting high solid solubility. The maximum solubility of Al in Mg is 12.7wt.% at 710K and 0.5wt.% at room temperature. Mg-Al alloys system shows eutectic behavior and eutectic reaction (as given in equation (1.1)) takes place at 437°C. The most common phases available in γ -Mg₁₇Al₁₂ and β -Mg₂Al₃.

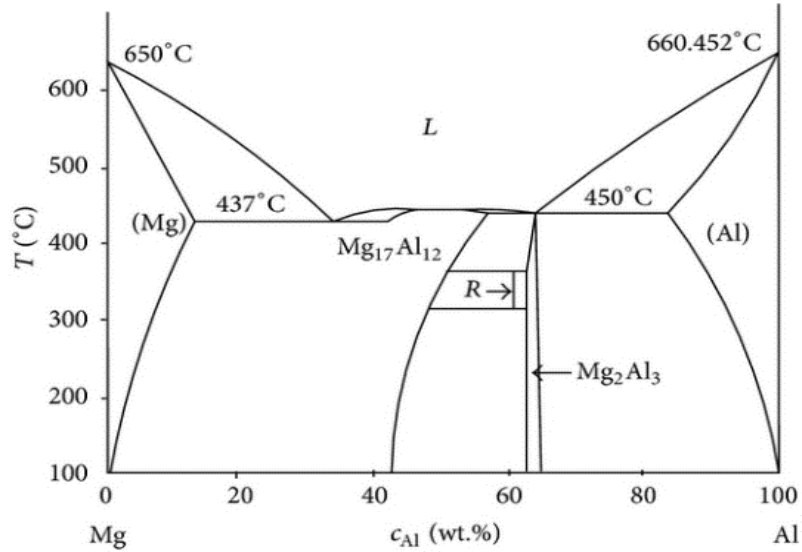
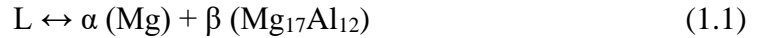


Figure 1.3: Phase diagram of Mg-Al binary phase diagram

Zheng et al. studied the effect of adding varying amounts of aluminum to magnesium through gradient hot rolling and found that grain refinement occurred much faster due

to dynamic recrystallization in pure Mg than AZ31 alloy. Additionally, they also found that due to finer size and higher volume fraction of $Mg_{17}Al_{12}$ precipitates in AZ91, Zener pinning pressure increases significantly thereby affecting dynamic recrystallization adversely.

Presence of zinc (Zn) in AZ series influences the extrudability of these alloys. The ternary Mg-Al-Zn phase in these alloys has a low eutectic temperature and therefore, affects the processing temperature of the alloy [32]. Also, the addition of Zn to this system reduces the solid solubility of Al in Mg thereby increasing the number of precipitates formed during aging and causing a moderate increase in strength [32-34]. Yu et al. observed the effect of Zn content on laser welded ZK alloys. With increase in Zn content, the amount and mean size of $Mg_{51}Zn_{20}$ precipitates along grain boundaries in the fusion zone increased coupled with a change in morphology from cellular to equiaxed to dendritic. Also, mean grain size in the fusion zone decreased, thereby achieving higher tensile strength of 312 MPa [35]. AM series alloys containing aluminum and manganese such as AM30, AM40, AM50, or AM60 generally have higher extrudability in comparison to AZ alloys due to the absence of Zn containing eutectic ternary phases and show better mechanical properties in comparison to alloys with the same Al contents (AZ31 and AM30 for instance) [36]. Huang et al. reported higher stretch formability in AM60 alloys compared to AZ61 alloys due to weak basal textures and basal pole splitting in AM60 [31, 36].

Addition of RE elements has been reported in the literature to improve mechanical properties by promoting the growth of non-basal oriented grains through retardation of dynamic recovery and recrystallization processes [27, 28, 37-40]. Wang et al. [37]

reported the improvement in mechanical properties of AM50 alloys by addition of Y and Ce both at room and elevated temperatures. $\text{Al}_{11}\text{Ce}_3$ and Al_2Y precipitates formed during processing promoted grain refinement by retarding grain growth. Li et al. studied the effect of Y on the mechanical properties of an $\text{Mg}_{97}\text{Y}_2\text{Zn}_1$ alloy (processed by ECAE) at different strain rates. They noted an improvement in strength and isotropic deformation behavior due to reduction in texture intensity by randomized orientation of grains in the Mg matrix and presence of fragmented LPSO phases [38]. Several Mg alloys were developed with a combination of RE elements known as misch-metal (MM) following their success as alloying elements. On studying the microstructural and mechanical properties of Mg-5Y-5Gd-xNd-0.5Zr alloy, Li et al. found island compounds along grain boundaries such as Mg_{24}Y_5 , $\text{Mg}_{41}\text{Nd}_5$, Mg_5Gd led to an improved tensile strength and elongation of 380 MPa and 9% respectively through precipitation hardening [39]. The quasi-static and dynamic compression behavior of Lanthanum doped Mg alloy, AZXE7111 was studied by Shen et al. They attributed the significant increase in strength to nanoscale Al_2Ca and $\text{Al}_{11}\text{La}_3$ intermetallic compounds acting as dislocation barriers leading to finer grains. Additionally, the extensive twinning observed in these alloys has been attributed as the major reason for the increased strain hardening at higher strain rates than lower strain rates [41].

Magnesium- lithium (Li) based alloys with high concentration of lithium (>11%) are also light weight and can be made with 25% lesser density compared to other Mg alloy series [42]. Drozd et al. [43] observed the decrease in c-axis lattice parameter making non-basal slip activities easier thereby reducing the flow stress required for

deformation in LA43 and LA45 alloys. A few lithium lean alloys were also studied in the literature. One such interesting research was done by Zou et al. [44] on texture development in dual phase Mg-Li alloys (low Li content such that both α and β phases coexist). The strength and ductility of these alloys were improved by thermo-mechanical processing mainly due to the basal and non-basal activities in the Mg-rich σ phase during hot deformation and contribution of fiber texture from the β phase. Also, ternary alloy additions to Mg-Li alloys have been reported to form coherent metastable precipitates thereby improving mechanical and chemical properties [42, 45]. Although other elements such as Ca etc. are also used, the alloying elements discussed above are the most predominantly used and structurally effective.

1.2.3 Effect of severe plastic deformation (SPD)

Severe plastic deformation is defined as “any method of metal forming under an extensive hydrostatic pressure that may be used to impose a very high strain on a bulk solid without introducing a significant change in the overall dimensions of the sample and able to produce exceptional grain refinement” [46]. The seminal work by P.W. Bridgeman developed the scientific grounds for materials processing through a combination of hydrostatic pressure and shear deformation [47, 48]. Such techniques have evolved and gained popularity owing to their ability to produce considerable grain refinement and better properties in bulk form, which are some promising aspects when used as structural materials. Several SPD techniques such as equi-channel angular extrusion (ECAE), hot forging, high pressure torsion, cold/hot rolling have been extensively researched in the previous years. ECAP has proved to improve

ductility in Mg alloys since simple shear evokes a specific kind of texture in HCP metals [7, 49-51].

Ding et al. reported improved strength through ECAP route A due to the absence of texture softening components unlike routes B_c and C where these components cancel the grain refining effect [52]. A combination of higher tensile strength and better ductility was achieved by Valiev et al. in Titanium processed through ECAP [51]. Similar results (~50% elongation-to-failure) have been reported by Mukai et al. with annealed/ECAPed AZ31 [7]. Significant strain hardening and large uniform elongation was achieved in comparison to the extruded alloy as shown in fig. 1.4. However, the associated texture-related reduction in the yield strength acts against the Hall-Petch-type strength enhancement due to grain refinement [53, 54]. Similarly, ZK60 alloys responded with tensile elongations stretching to superplastic deformation regime primarily due to randomization in texture [55-57]. Some authors also recorded superplastic behavior of AZ91 alloy processed through ECAE at a lower temperature of 448K. Although this behavior was attributed to grain boundary sliding and viscous glide of dislocations, the stronger dependence of mechanical properties on initial grain size (sample with small grain size of 1 μ m exhibited much lower flow stress and much larger elongation in comparison to the sample with grain size of 37 μ m) remained unclear [57].

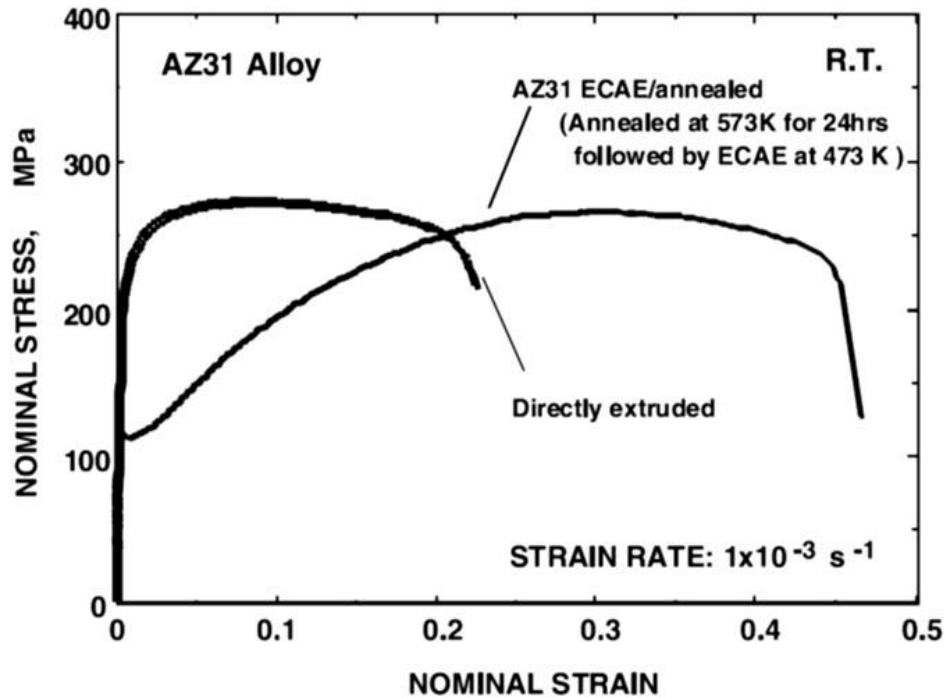


Figure 1.4 Stress-strain curves of annealed/ECAPed AZ31B compared to the same alloy processed by direct extrusion [57]

The potential to improve the strength of Mg alloys through high pressure torsion was explored by Livia et al. who studied the process on commercially pure Mg (CP-Mg) and three alloys namely, AZ31, AZ91 and ZK60. Peak hardness values of the alloys were larger than any sample processed by conventional techniques and comparable to that obtained with alloys containing RE elements [58]. Similarly, increase in hardness and tensile strength has been reported by a few authors in pure Mg (99.9%) and Mg - 9%Al alloy (measured elongation of 810% during tensile testing as shown in fig. 1.5) [59, 60]. Despite the efficiency in grain refinement and improvement in mechanical properties, this method is primarily used for research purposes due to the limitation in the size of samples that can be processed (typically 10-15mm in diameter and 1mm in thickness).

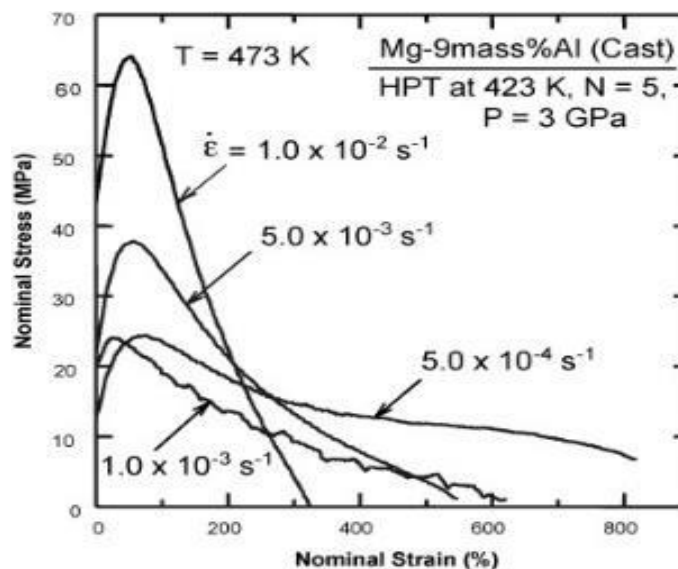


Figure 1.5 Nominal stress vs strain for cast Mg-9%Al specimens processed by HPT for 5 turns at and tested at different strain rates [59].

Although ECAP process poses a lot of advantages, the shortcoming of ECAP as a batch process (unless integrated with extrusion as suggested by Orlov et al. [57]) and the process' inability to produce nanocrystalline (<100nm grain size) material increased the prospect of rolling as a severe plastic deformation (SPD) method for manufacturing Mg alloys. Flat rolling is considered as the most feasible deformation processes for continuous production of bulk sheets. Currently, approximately 90% of all metals are rolled at some point during the manufacturing process. Conventional rolling or extrusion are proven methods that produce highly textured alloys. Therefore, the predominant mechanisms depend on direction of loading as well as loading mode (tension or compression) with respect to the c-axis of the polycrystalline material [61-64]. Zarandi et al. studied the effect of varying Al content on the rollability of AZ series alloys. They determined that increasing the Al content to 6% promotes edge cracking and ~3-4% Al addition is ideal for rolling satisfactorily. They pointed out that dislocation creep at lower temperatures and solute drag creep/grain boundary

sliding at high temperatures were the primary operating deformation mechanisms. They also concluded that ~3-4% Al in low Mn alloys improved tensile elongation at low strain rates and yield strength at high strain rates due to different mechanisms (dislocation creep and grain boundary sliding at low and high strain rates respectively) operating at those regimes whereas increasing the Al content to 6% degraded both the properties [65]. Some studies that compare ECAP with conventional rolling reveal that the former method produces a homogeneous microstructure but a higher average grain size whereas latter produces bimodal structure with lesser average grain size in comparison. Although the textural intensity is reduced, basal texture is still preserved in hot rolled AZ31 and AZ61 alloys [66-68].

Zheng et al.[69] studied the effect of varying thickness reduction on the competition between twinning induced nucleation and inhibition of recrystallization by Zener pinning of second phase particles in hot rolled AZ31 and AZ91 alloys. They found that twin dynamic recrystallization occurred in $\{10\bar{1}1\} - \{10\bar{1}2\}$ double twins but as Al content was increased, propensity of twin nucleation decreased due to Zener pinning pressure (F_z) increasing significantly due to the presence of increase in volume fraction of fine $Mg_{17}Al_{12}$ precipitates. Wang et al. investigated the effect of initial texture related to rolling geometry on dynamic recrystallization of AZ31 alloy during rolling at 573K. They found that in plates aligned perpendicular to the normal direction (ND plates), dislocation glide and $\{10\bar{1}1\} - \{10\bar{1}2\}$ double twins were the main deformation mechanisms whereas for the plated aligned perpendicular to the Transverse direction (TD plates), $\{10\bar{1}2\}$ extension twins were the dominant

deformation mechanism. Dynamic recrystallization was retarded in TD plates due to the reduced dislocation glide and hence, stored energy [70].

In addition to symmetric rolling, asymmetric rolling was also studied extensively in the literature. Asymmetric rolling introduces a shear component shifting the texture by 5-10° in addition to the plane strain compression of conventional rolling thereby giving rise to better ductility at the cost of giving up some strength [71-74]. A relatively new technique called as differential speed rolling (DSR) involves deformation by varying the rotational speed of the upper and lower rolls imposing unequal rolling velocity and shear strain on the sheet. This method is proven to achieve both grain refinement and control of deformation texture affecting the anisotropy of mechanical properties. Various researchers have found the great impact DSR has on reducing the intensity of basal texture and improvement in the ductility of these alloys. They established that by increasing the shear deformation either by changing the roll speed ratio or rolling reduction, random texture was generated by weakening the basal slip and activating non-basal slips [73-77]. Several other conventional hot rolling studies where samples have been successfully rolled to 80% reduction in a single pass have been effective in reducing the grain size from 12µm to 2.2µm along with increase in tensile strength from 275 to 300MPa along with improvement in elongation [78]. A recent paper by Xu and coworkers compared and effects of different rolling methods on the microstructural evolution and mechanical properties of various binary Mg-alloys and concluded that differential speed rolling has a number of advantages[79].

1.2.4 Dynamic recrystallization

Recrystallization is the formation of strain-free new grain structure in a deformed material by the formation and migration of high-angle grain boundaries (HAGBs) driven by stored energy introduced during plastic deformation [80]. It may occur heterogeneously with (i.e., discontinuous) or homogeneously without (i.e., continuous) clear nucleation and growth stages. The recrystallization process during annealing is commonly referred to as static recrystallization (SRX) whereas that occurring during deformation at elevated temperature is referred to as dynamic recrystallization (DRX). The driving force for recrystallization is the amount of stored energy within the metallic material. This energy (a bulk of which dissipates as heat with only a fraction of remaining energy getting stored) arises from the crystalline imperfections especially, dislocations and lattice strains due to crystal defects generated in the material during its processing [81]. For sub-grains to become new grains, it is necessary to have a high angle of misorientation as well as an energy advantage (a larger sub-grain created by strain induced boundary migration, SIBM, due to bulging of part of pre-existing HAGB leading to sub-grain growth or sub-grain coalescence). Incubation time, that is, the time needed to form these larger sub-grains such that the stored energy is sufficient to overcome the boundary curvature was initially coined by Bailey and Hirsch [82] to indicate the initiation of recrystallization during SRX became no longer convenient for defining DRX. Thus, critical strain (ϵ_{cr}) or critical dislocation density (ρ_{cr}) is used as the key terminology to indicate onset of recrystallization.

Ion et al. studied the microstructural evolution during hot deformation of Mg-0.8%Al alloys and found that dynamic recrystallization occurred only above 425K. They determined the mechanism to be dynamic polygonization of rotated lattice regions along the grain boundaries, a similar mechanism observed in minerals especially quartzite. At temperatures $<600\text{K}$ and higher rates, deformation became macroscopically inhomogeneous leading to finer grain regions being confined to shear zones and geometrically softer than the rest of the specimen [83].

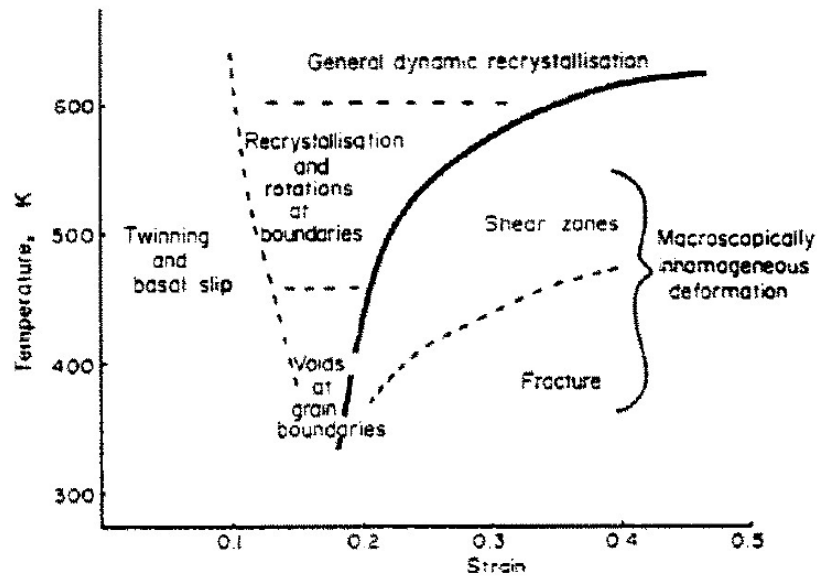


Figure 1.6 Semi-quantitative diagram showing the variation of deformation as a function of temperature and strain [83]

There are two types of static recrystallization, (a) discontinuous and (b) continuous static recrystallization:

a. Discontinuous static recrystallization (DSRX) is where fine dislocation free crystallites are formed by static recovery during early stages of annealing.

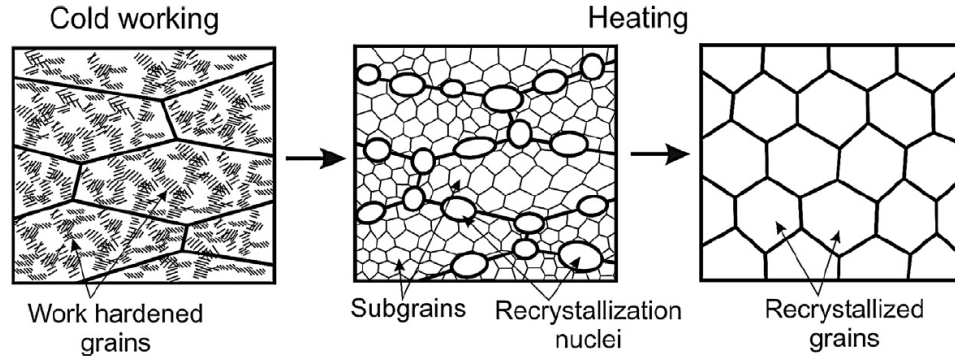


Figure 1.7 Schematic diagram representing discontinuous static recrystallization (DSRX) taking place during annealing of strain hardened materials [86]

These nuclei then grow and consume the entire strain hardened matrix driven by stored energy associated with dislocations and/or sub-grains (fig. 1.7) [84-86].

b. Continuous static recrystallization (CSRX) is where grains are formed by gradual localized migration of sub-grains formed during severe deformation when subjected to annealing as shown in fig. 1.8 [84-86].

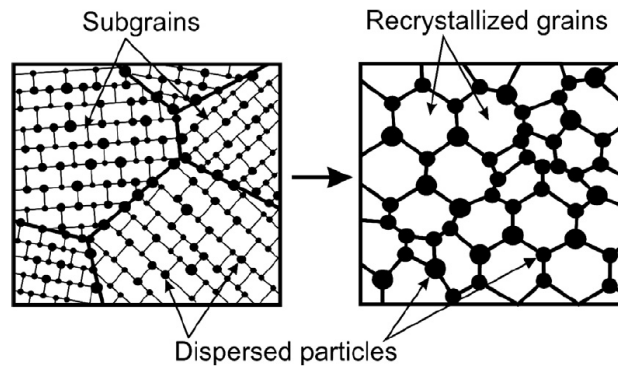


Figure 1.8 Schematic diagram of continuous static recrystallization (CSRX) [84-86]

In contrast, during deformation, the most common type of recrystallization, that is, dynamic recrystallization (DRX) is categorized into three types, (a) discontinuous DRX, (b) continuous DRX, and (c) geometric DRX.

a. Discontinuous DRX (DDRDX):

The schematic representation of the process of new grain formation is given in fig. 1.9, wherein (a) represents boundary corrugation accompanied by dislocation sub-boundary evolution at low strains; (b) grain boundary sliding leading to further development of local strain gradients during further straining, and (c) part of serrated grain boundaries getting bulged out accompanied by evolution of strain induced sub-boundaries at high Z or twin boundaries at low Z [82, 85-88].

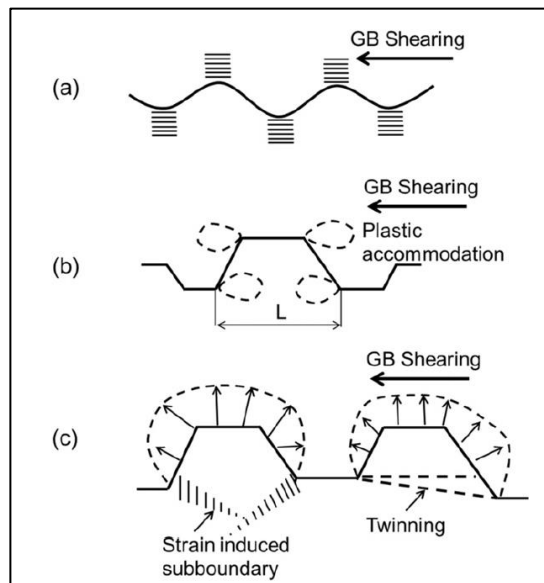


Figure 1.9 Schematic diagram showing the nucleation of DDRX grain [85]

b. Continuous DRX (CDRX):

In CDRX, nucleation of small particles occurs by progressive rotation of sub-grains (fig.1.10).

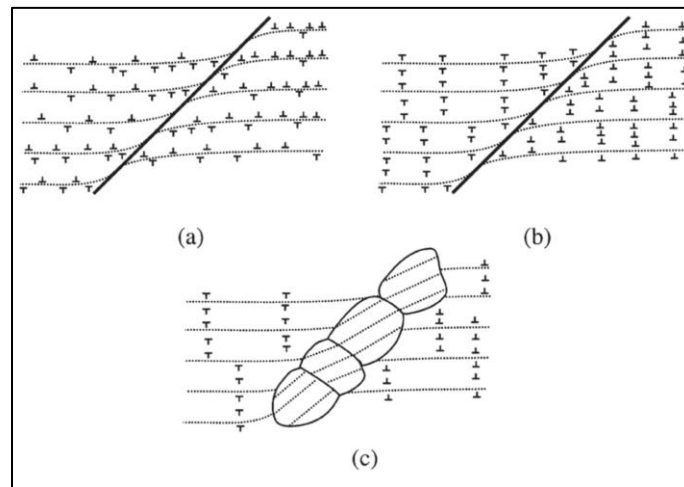


Figure 1.10 Schematic diagram of deformation and dynamic recrystallization in grain boundaries [83, 85]

Local shearing initially develops near grain boundaries due to the onset of non-uniform deformation, as shown in (a). As the shearing proceeds, lattice rotation occurs near grain boundaries and dynamic recovery (DRV) can initiate as shown in (b). Eventually, as observed in (c), small amounts of sub-grain boundary migration led to coalescence of boundaries and formation of new grains with HAGBs [83, 89-91].

A comparison of the characteristics of discontinuous and continuous dynamic recrystallization is given in the table below.

Table 1.2. Comparison of DDRX and CDRX characteristics [86]

Metals	Conditions	CRSS _{basal} (Mpa)	CRSS _{twin} (Mpa)	CRSS _{prism} (Mpa)	CRSS _{twin} / CRSS _{basal}	CRSS _{prism} / CRSS _{basal}
Mg	SC	0.81 ^a ; 0.76 ^b ; 0.45 ^c ; 0.65 ^d ; 0.52 ^e	2 ^f	39.2 ^g	2.5 – 4.4	48 – 87
Mg 0.5 at. pct Zn	SC		2.7–2.8 ^h			
AZ31B	PC, VPSC, XRD	45 ⁱ	15 ⁱ	110 ^j	0.33 ⁱ	2.4 ⁱ
AZ31B	PC, EPSC, ND	10 ^j	30 ^j	55 ^j	3 ^j	5.5 ^j
AZ31B	PC, Taylor, XRD				2 ^k	1–2.4 ^k
AZ31B	PC, TEM					1.1 ^l
AZ31B	PC, ND, Schmid factor		25–35 ^m			
AZ61	PC, XRD					1.5–2 ⁿ
Mg 7.7 at. pct Al	PC, ND		65–75 ^o			

SC, single crystal; PC, polycrystal; XRD, X-ray diffraction; ND, neutron diffraction; VPSC, visco-plastic self-consistent model; EPSC, elasto-plastic self-consistent model; Taylor, Taylor model.

c. Geometric DRX (GDRX):

At small deformations, the grain boundaries flatten with well-defined substructure in the matrix. As deformation progresses, the serrated HAGBs (thick black lines shown in fig. 1.11) become closer, although the size of the sub-grain remains almost constant. Eventually, HAGBs impinge resulting in a microstructure comprising mostly of HAGBs [86]. GDRX aids in formation of equiaxed grains during hot deformation by (a) migration of HAGBs to form serrations. (ii) thinning of grain thickness, and (iii) impingement of serrated grain boundaries when approaching 1-2 μm sub-grain size.

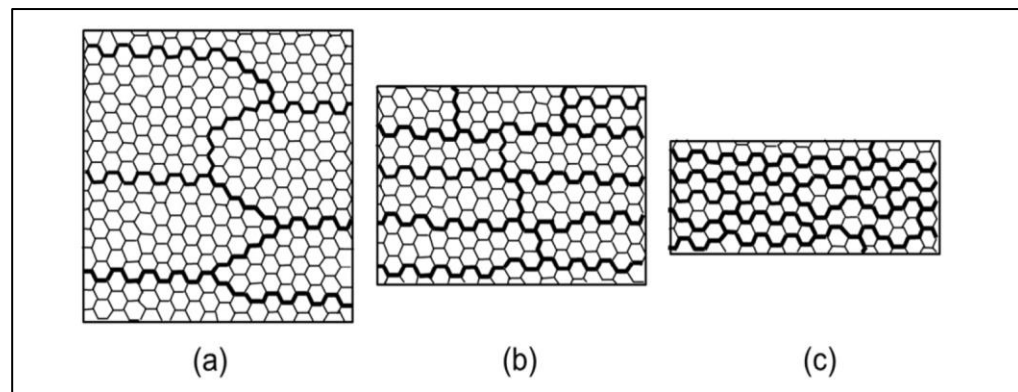


Figure 1.11 Schematic diagram showing GDRX with (a) The grain boundaries flattening (b) the serrated grain boundaries becoming close; and (c) a microstructure consisting of mainly HAGBs forming [86].

Fig. 1.12 summarizes the various DRX mechanisms previously discussed in a nutshell [85]. Ion et al., were the first to provide a mechanism for DRX consisting of a succession of twinning, basal slips, and lattice rotations at grain boundaries forming sub-grain boundaries which lead to the formation of recrystallized grains having HAGBs. They called it rotational DRX (RDRX) since it involves progressive rotation of sub-grains [83].

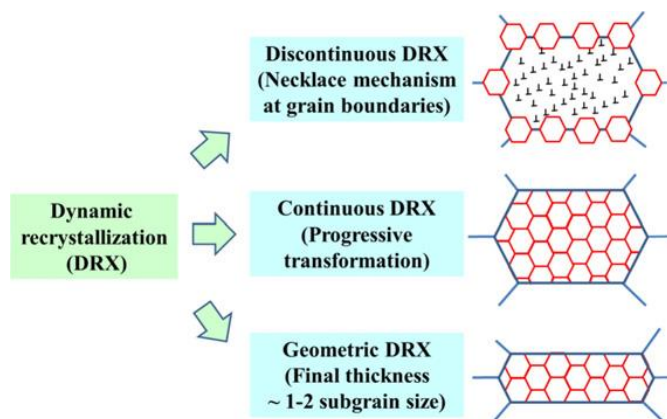


Figure 1.12 Summary of various dynamic recrystallization mechanisms in a nutshell [85]

Humphreys and coworkers identified both CDRX and DDRX mechanisms operating in magnesium alloys and found that the transition temperature for these mechanisms was $\sim 600\text{K}$ [92, 93]. Galiyev et al. and Sitdikov et al. made the best effort to correlate DRX with deformation mechanism. By studying activation energies, they found that CDRX is linked to deformation caused by cross-slip and DDRX is linked to deformation controlled by climb [81, 82, 88]. Microstructure to mechanical property mapping on AZ31B was done by Barnett et al. They found that the progress of recrystallization was dependent on crystalline orientation with respect to the c-axis. While DRX volume fraction was dependent, recrystallized grain size was independent on the deformation conditions [94-97].

Del Valle et al. [98] compared the effect of texture on DRX and deformation mechanisms of rolled and ECAPed AZ31B. They found that at moderate temperatures, deformation induced DRX is significantly higher in rolled samples compared to ECAPed ones while at higher temperatures, DRX tends to be similar in both. It was also found that fiber texture stimulates DRX through enhancement of multiple slip thereby producing heterogeneities in the microstructure which aid in

creation of nucleation for DDRX. While some authors claimed there is no direct link between DRX and deformation mechanism [98], few others strongly correlate the effect of deformation on DRX mechanisms as shown in fig. 1.13 [99]. Although the previous correlation is yet to be clearly established, effect of initial texture on DRX and deformation mechanism during rolling and extrusion was clarified by Wang et al. [98] and Li et al. [99] respectively.

The former study revealed that in the normal direction (ND), dislocation glide associated with $\{10\bar{1}1\}$ - $\{10\bar{1}2\}$ double twins led to a faster stored energy accumulation in comparison to the transverse direction (TD) where the stored energy was small due to $\{10\bar{1}2\}$ extension twins having basal texture with the c-axis nearly parallel to the ND and hence, retarding DRX [82]. The same was confirmed by the latter study revealed that dislocation slip was attributed as the main reason for extensive DRX due to higher stored energy in the extruded annealed alloy in comparison with the lower stored energy in the rolled annealed alloy due to profuse $\{10\bar{1}2\}$ extension twinning in Mg alloys.

Galiyev et al. [99] also did a similar kind of study on ZK60 alloy and the results were interesting. The mechanisms were roughly divided based on similar temperature-strain rate regions. At temperature below 473K, twinning, basal slip, and (c+a) dislocation slip promoted the formation of HAGBs and low temperature DRX (LTDRX). In the intermediate temperature range of 473-523K, a power-law creep regimen was observed associated with cross slip of dislocations according to Friedel-Escaig mechanism resulting in CDRX. At the high temperature range of 523-723K, dislocation climb controlled by self-diffusion was proposed to provide conditions of

DRX [94]. Based on deformation conditions, the deformation mechanisms map are given by fig. 1.13.

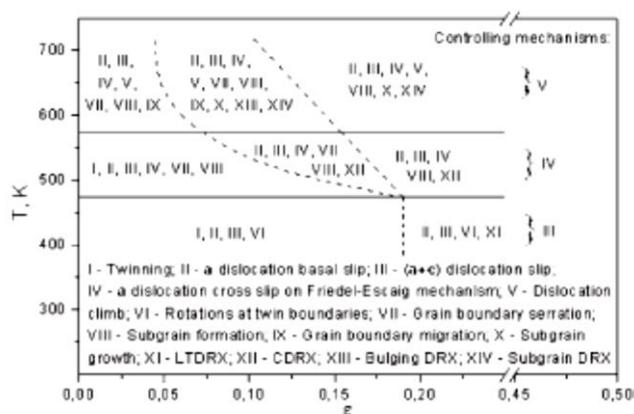


Figure 1.13 Schematic diagram showing deformation and DRX mechanisms [99]

Depending on composition and properties, Mg alloys can be classified into two groups. First group includes Al as alloying element, and second group doesn't. The first group of alloys are characterized by low cost of manufacture and hence, they can be industrialized and commercialized easily. Their properties such as age-hardenability, strength, castability, weldability, corrosion resistance etc. is not satisfying. For example, strength of AZ91 is high but its ductility is low whereas for AM60, it is vice-versa [31, 36]. The second group of alloys contain rare earth elements as predominant alloying elements and generally possess better mechanical properties in comparison to the first group of alloys. But their cost of production is very high and hence, commercialization is quite difficult. Owing to the easier manufacturability and scope of improvement in mechanical properties through additional alloying, heat treatment, thermo-mechanical processing etc. leading to grain refinement, precipitation strengthening, texture randomization etc., Mg- Al system takes precedence and will be discussed further.

1.2.5 Precipitation in Mg-Al alloys

The equilibrium solid solubility of Al in Mg is 11.8 at% at the eutectic temperature and reduces to 3.3 at% at the temperature of 473K. The Mg-rich portion of Mg-Al binary phase diagram has two phases namely α -Mg and β -Mg₁₇Al₁₂. The β phase has a Body Centered Cubic (BCC) crystal structure with a lattice parameter of a \sim 1.06nm [100, 101]. The thermodynamic driving force to generate large number of β precipitates by aging at 473K (equilibrium volume fraction becomes 11.4%) gives a lot of opportunities to exploit. But the distribution of the precipitates remains relatively coarse due to the relatively high diffusion rate of Al atoms in Mg and a probability of defects (vacancies) being higher in the α -Mg matrix, although they are resistant to dislocation movement. As a result, the age-hardening response is not significant as expected [102-105].

Two types of precipitation occur based on the location of their occurrence. Continuous precipitates are those that occur inside the grains and discontinuous precipitation are those which initiate along the grain boundaries and grow towards the center of the grain in a cellular form. The cellular form is formed by the reaction in which the super-saturated solid solution α' decomposes to an α phase, with less concentration of Aluminum and structurally identical to the α' phase and the intermetallic β phase. Both kinds of precipitates compete and occur simultaneously during isothermal aging of Mg-Al alloys [106].

Many researchers have studied the nature of precipitation and found contradicting results. Duly et al. proposed that continuous precipitates were favored at low and high aging temperatures whereas discontinuous precipitates were favored only at

intermediate temperatures. This was due to the dominance of volume diffusion of solute preventing nucleation and growth of the cellular structure at high temperatures and low driving force due to early occurrence of continuous precipitates at lower temperatures [107]. Contrastingly, Braszczyńska-Malik et al. observed only discontinuous and only continuous precipitates at lower temperatures (423K) and higher temperature (623K) respectively. At intermediate temperatures (523K), they recorded the co-existence of both types of precipitates [108].

The β phase adopts the exact Burgers orientation relationship of $(011)_{\beta} \parallel (0001)_{\alpha}$, $(\bar{1}\bar{1}1)_{\beta} \parallel (2\bar{1}\bar{1}0)_{\alpha}$ and usually has a plate morphology with its broad surface parallel to $(0001)_{\alpha}$ [109]. Although this phase is often described as incoherent, experimental evidence suggest otherwise [106, 110, 111]. There is another orientation relationship $(\bar{1}\bar{1}0)_{\beta} \parallel (\bar{1}\bar{1}00)_{\alpha}$, $(111)_{\beta} \parallel (0001)_{\alpha}$ wherein the precipitates presume a rod shape with their long axes parallel to $(0001)_{\alpha}$ and hexagonal cross-section [109]. Precipitates with rod morphology have proven to be better at impeding dislocation than $(0001)_{\alpha}$ precipitates and hence, the methods to promote the former and suppressing the latter is under extensive research.

There are pockets of research which claim success in enhancing the age hardening response by imparting cold work after solution treatment prior to aging. The improvement in aging kinetics was attributed to increased number density of dislocations, twins formed during cold work, and lattice defects where the heterogenous nucleation of β precipitates occurred. Recently some efforts were focused on creating fine precipitates with high number densities in Mg alloys using deformation by introducing defects such as dislocations and vacancies within grain

interiors thereby precipitating fine nanoscale precipitates [112-115]. During thermo-mechanical processing, mobile dislocations form a complex sub-structural environment leading to few and smaller solute clouds which ultimately multiply to produce fine precipitates [116]. Prameela and co-workers correlated the observed enhancement of precipitate nucleation during dislocation driven precipitation to increased rate of dislocation multiplication [117].

Effects of second phase particles on recrystallization are summarized as follows:

1. The stored energy and hence, the driving pressure for recrystallization may be increased.
2. Large particles may act as nucleation sites for recrystallization.
3. Particles, if closely spaced may exert a pinning effect on LAGB and HAGBs.

While the first two effects tend to promote recrystallization, the last effect retards it. The kinetics of recrystallization, that is, the resulting grain size and texture depends on which mechanism dominates. The size, distribution, and volume fraction of precipitates controlled by the chemical composition and processing determine the microstructure and texture of the recrystallized alloy. The effect of particles on the overall dislocation density and inhomogeneity of deformation in the matrix, along with the nature of deformation structure in the particles' vicinity are the three main aspects of deformation which are salient in determining the behavior of material during subsequent processing.

Research indicates that the transition from accelerated to retarded recrystallization is primarily a function of the volume fraction of particles, f_v , and particle radius, r . Ito et al. suggested that $f_v^{1/2}/r$ which is equivalent to the critical value of particle spacing

(λ) may be an indicator for the transition. Acceleration of recrystallization was attributed to increased driving force from dislocations generated by particles during deformation. This kind of acceleration is rarely found in Al alloys with fine grains rather than Cu since the large amount of dynamic recovery in Al leads to reducing the number of geometrically necessary dislocations (GNDs) created at the particles. Particle stimulated nucleation (PSN) is observed in these alloys. PSN is typically defined as recrystallization at or near the surface of coarse ($> 1\mu\text{m}$ diameter) particles caused by the enhanced deformation required to maintain strain compatibility near the particle. Thus, PSN is responsible for either texture weakening or formation of a new texture component depending on the material category and type of processing [92, 118]. Typical PSN features include LAGBs forming in contact with the precipitate connected to other grain boundaries.

In addition to PSN, the presence of a larger volume fraction of particles may pin grain boundaries through the mechanism of Zener drag. Particle pinning due to solute segregation results in reduction of grain boundary mobility which may alter the activity of other recrystallization mechanisms. For example, discontinuous DRX (DDRX) where nucleation occurs at pre-existing grain boundaries through grain boundary serration and rotation of the resulting sub-grains is inhibited due to reduced grain boundary mobility [119]. As such, the improvement in the strength of Mg-9%Al alloys can be attributed to various factors such as refined DRX grains and $\text{Mg}_{17}\text{Al}_{12}$ precipitates. The influence of these precipitates in pinning dislocations through Orowan strengthening mechanism has been studied and reported widely. The presence of $\text{Mg}_{17}\text{Al}_{12}$ particles contribute to accommodate local strain to reduce stored

deformation energy leading to a lack of sufficient stored energy available for stimulating recrystallization. Fine precipitates dispersed in the grain interior or at grain boundaries could also produce the pinning effect on grain boundary migration to restrict recrystallization.

The interface between the matrix and second phase particles is also an important factor for pinning dislocations in Mg alloys. The plate-shaped $Mg_{17}Al_{12}$ phase generated in the grain interiors was almost parallel to the $\{0001\}$ as basal precipitates. However, neither large nor thin basal precipitates are effective for pinning dislocations, but the spherical precipitates refined from rod-shaped particles along grain boundaries have a dominant influence in inhibiting recrystallization [120]. In the case of spherical particles, size and volume fraction are the two important factors. There is an important criteria for the occurrence of recrystallization, i.e., the driving force for recrystallization (F_d) must be greater than the Zener pinning pressure (F_z). In the case of AZ91, as calculated by Jin et al., the F_z value increases from 1.4×10^5 to 8.8×10^5 Nm^{-2} with increase in deformation, but F_d ranges from $0.8-1.0 \times 10^5$ Nm^{-2} . Since the F_z value is higher than F_d during both the initial and subsequent (due to variation in precipitate morphology) deformation stages, it implies that there is a strong pinning effect of precipitates on grain boundaries and consequent inhibition of complete DRX of the microstructure [120].

1.3 SEM- EBSD studies

EBSD is a technique to study crystallographic orientations, misorientation, texture and grain boundary angles on a sub-micron level in the scanning electron microscope. It is a sensitive technique collecting information from only tens of nanometers. In simple terms, incident beam electrons get scattered between crystal planes and form cone of diffracted electrons which when intersecting a phosphor screen appears as pair of lines (Kikuchi patterns). Each pair of lines known as Kikuchi lines represent planes in the crystal. The electron backscattered diffraction (EBSD) Pattern which forms as a result contains information about angular relationship between planes, crystal symmetry, orientation and misorientation between the planes. EBSD data can be presented and visualized at the micro and nano scale using various qualitative and quantitative parameters [121].

A grain is a 3D crystallite that is uniform internally and differs in crystallographic orientation from its neighbors. Grain size is an important attribute to understand the physical and mechanical properties of metallic materials especially through Hall-Petch relationship where strength is inversely proportional to square root of grain size. To measure grain size accurately, all the grain boundaries need to be detected. Therefore, the highest degree of grain delineation is required from the technique. Although, traditionally light optical microscopy was used to measure grain size, there is a limit to its resolution hence making EBSD technique a viable alternative to measuring grain size. Grains can be identified by assigning a critical misorientation angle and grain boundaries are those 'pixel pairs' which have misorientation angle higher than the

critical value. Once individual grains are detected, statistics of grain measurements such as size, aspect ratio etc. can be identified [121].

Generating grain boundary map is also critical in visualizing microstructure. Grain boundaries influence the properties of material in several ways. They can act as a source of corrosion initiation, a site for precipitate nucleation or influence creep mechanisms. Smaller grain size and higher number of grain boundaries can also improve mechanical properties by disrupting dislocation movement and hence, techniques such as grain boundary engineering is employed to improve mechanical properties. Grain boundaries are characterized based on the misorientation angle between the two grains. Generally, LAGBs or sub-grain boundaries and HAGBs are those with misorientations $<5^\circ$ and $>10^\circ$ respectively. In addition to them, special or twin boundaries also called as coincident lattice sites (CSL) occur where the crystal lattice share a fraction of sites on each side of the boundary. In the misorientation distribution plot, distinctive peaks of same misorientation angle will be observed giving a quick overview of the boundary occurrences in the sample. Along with misorientation angle, misorientation axis can also be calculated. This means that EBSD can provide information by using a combination of both misorientation angle and axis such as identifying twin boundaries etc. Other parameters such as Grain orientation spread (GOS) and Kernel average misorientation (KAM) can also provide information on recrystallized area fraction/strain partition between two different grains belonging to different phases and stored strain energy/ strain localization along the grain boundary present in the materials respectively. For GOS calculation, the

average orientation is first calculated for each grain and each pixel in the grain. The spread is the average misorientation between the previously obtained two values [122]. A kernel is a set of points of prescribed size around the scan point of interest. The kernel size is generally described to the n th nearest neighbor. For KAM calculation, the misorientation between the neighboring points of the kernel are averaged. If grain boundary is present inside the kernel, then some of the misorientation values will be quite large. Thus, to exclude the grain boundary effect, misorientation within a specific tolerance value will only be included during the averaging calculation.

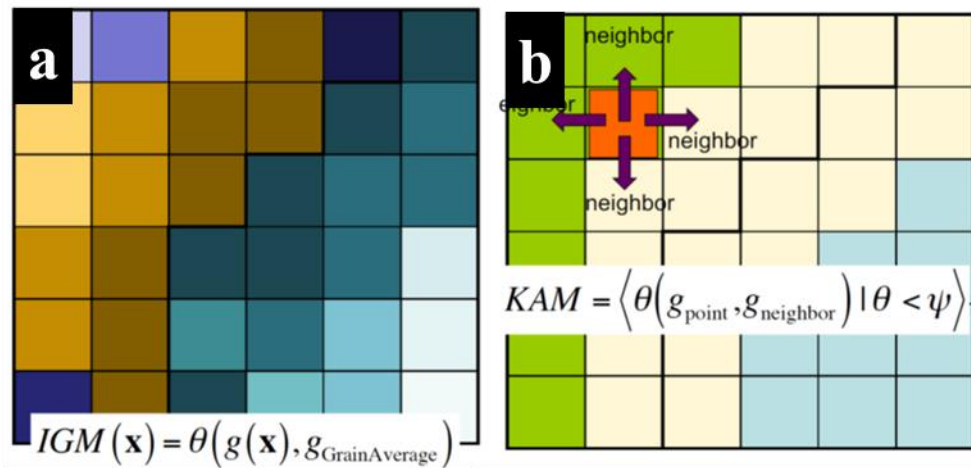


Figure 1.14 Schematic of computation of (a) GOS and (b) KAM where g and θ represent the orientation and misorientation angle respectively [122, 123]

Pole figures are used for displaying the overall sample texture. They enable 2D understanding of orientation instead of 3D by converting crystallographic orientation direction into points. Pole figure is a stereographic projection meaning orientations are plotted as two-dimensional projections. Poles i.e., the normal to a lattice plane for a selected family of planes are plotted with respect to the reference axis of the sample. Reference axes of the sample are given in fig. 1.15 below.

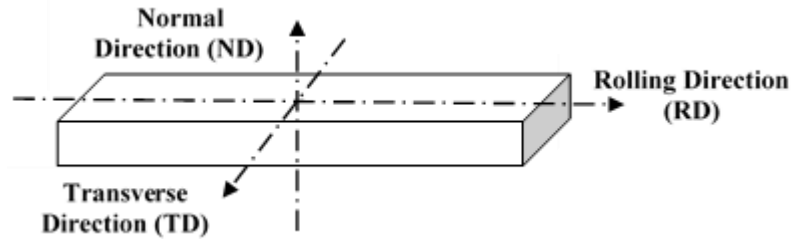


Figure 1.15 Sample reference axes.

This plot can be made for different family of planes. For example, plotting of $\langle 100 \rangle$ poles are shown in fig. 1.16 below. Firstly, lines are projected corresponding to the chosen poles to the hemisphere above the projection plane. Secondly, lines are projected from the point where the poles in the previous step meet the reference sphere to the bottom of the sphere. Lastly, a point is plotted where the lines in the second step meet the equatorial plane. For each measurement on the sample, due to different grain orientations, various points are plotted corresponding to the intersection of projected positions of poles on to the equatorial plane. Hence, a pole figure with many different measurements plotted (highly populated) is very useful for understanding orientation distribution [123].

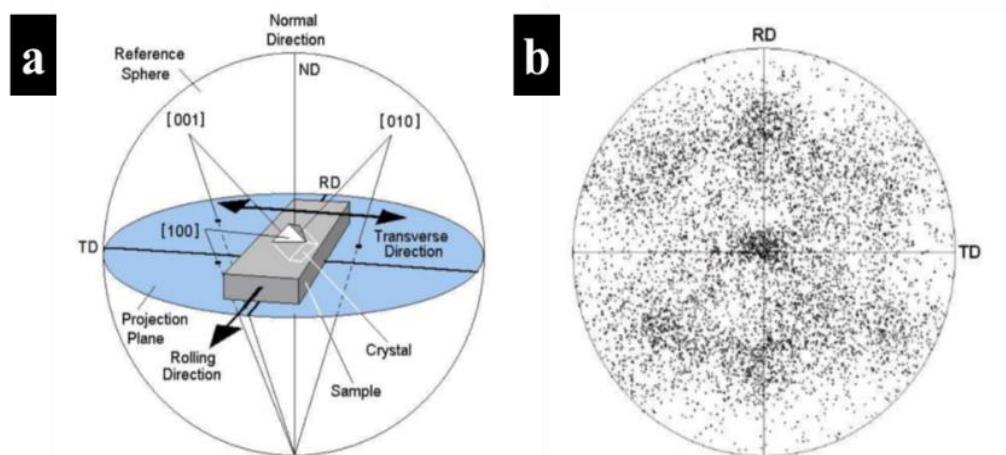


Figure 1.16 (a) Schematic principle of pole figure projections and (b) orientation distribution in a highly populated pole figure [123].

The orientation data can be spatially shown in Euler map or Inverse Pole Figure (IPF) maps. IPF maps can be used as an indicator of favored orientation or texture (characterized by single or similar colors in the map). It is a visualization tool that can be used to understand how specific texture is distributed spatially. They use the color scheme from the IPF color key that is designated based on the viewing direction and computed orientation. The color key has three major corners and colors such as red, blue and green assigned to each corners of the figure with smooth progression of colors in between. Individual orientation measurements can be related to a distinct color in the color key (fig. 1.17). It is easy to visualize the cubic material through following [123]:

- Red color signifies face of the crystal $\{100\}$ lying parallel to the surface.
- Green color signifies edge of the crystal $\{110\}$ lying parallel to the surface.
- Blue color signifies corner of the crystal $\{111\}$ lying parallel to the surface.

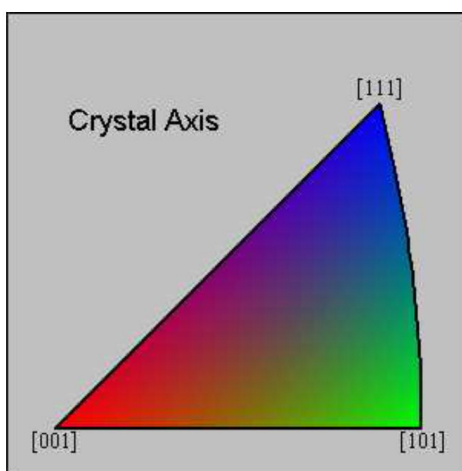


Figure 1.17 Inverse pole figure color key [123]

1.4 Scope and Objective of the Dissertation

In this dissertation, magnesium alloys were investigated since they are promising as lightest structural materials. The three Mg alloys of AZ31B, Mg-6%wt.Al, and Mg-

9% wt. Al were investigated and evaluated in terms of their mechanical behavior under quasi-static and dynamic compressive conditions. All three alloys in the as-cast condition were rolled in a confined manner.

Confined rolling is a novel method where the bar/sample is enclosed inside a hollow tube and sealed on both sides. The tube (with the sample enclosed) was then rolled until 60-65% reduction in thickness was achieved. Two advantages are identified for this method of rolling particularly for hard to work and easy to oxidize metals. First, it provides a confinement to the work piece, mitigating the tendency to cracking during rolling. Second, it provides some protection to the work piece from oxidation. Confined rolling was successfully used to roll tungsten at temperatures as low as 673K without obvious cracking[124-126]. Chen et al. [127] examined the effect of rolling W samples confined in a stainless-steel canister. With the volume of work piece being constant, the following equation can be derived

$$\ln\left(\frac{h}{h_0}\right) + \ln\left(\frac{b}{b_0}\right) + \ln\left(\frac{l}{l_0}\right) = 0 \quad (1.2)$$

where h, b and l are thickness (normal direction (ND)), width (transverse direction (TD)) and length (rolling direction (RD)) respectively. For conventional rolling, the first term i.e., the decrease in thickness is generally compensated by the second and third terms representing width and length increment respectively. But, in the case of confined rolling, due to the constraint along TD, there would be an increase in the third term therefore giving rise to shear stress accumulation. They assumed that this hypothesis combined with the strain accumulation due to thickness reduction and confinement of the canister was large enough to cut the grains along TD leading to grain refinement. They observed the same through the presence of low angle grain

boundaries and sub-grains in W ribbons. They concluded that confined rolling was effective in terms of grain refinement in comparison to conventional rolling [127]. In addition to this, a different micro texture could be generated due to limited grain rotation due to deformation confinement. Also, confined rolling posed other advantages such as inhibition of cracking and oxidation of the specimen. Next, to choose a canister material suitable with the specimen, their physical properties must be compatible as well.

Table 1.3 Physical properties of different canister materials [128]

Material	Density (g/cc)	Coefficient of thermal expansion ($\mu\text{m}/\text{m}\cdot^{\circ}\text{C}$)	Modulus of Elasticity (GPa)	Melting Point ($^{\circ}\text{C}$)	Hardness (HRB)
Mg alloys	1.77	26	44.8	605-630	49
Low Carbon Steel	7.75-8.08	10.1-16.6	183-213	~1430	86-562
Stainless Steel	8	17.3	193-200	1400-1455	123
Aluminum	2.84	24.1	73.1	543-660	117
Brass	8.49	20.5	97	885-927	70-140

After keen observation of the physical properties of various metals in table 1.3, brass was selected as a viable option having higher density and melting point, moderate hardness, and similar coefficient of thermal expansion to that of magnesium. Hence, brass was a chosen canister material for confined rolling of Mg alloys.

After confined rolling, the following aspects were analyzed:

1. Effect of Aluminum content on microstructure evolution in Mg-Al alloys,
2. Effect of second-phase particles (size and volume fraction) on dynamic recrystallization in the material,
3. Macroscopic and microscopic effect of precipitates on the mechanical properties of the material, and
4. Systematic study of the deformation mechanisms and activation of different slip modes in the material.

A multitude of research has happened over the past decades studying the commercial alloys such as AZ series, WE series, etc. But very few researchers have worked on binary alloys, particularly, the Mg-Al system. Even then, the focus has been primarily on the aging studies, particularly aging kinetics and mechanisms to conclude that the age hardening response is poor since they are not oriented to block basal slip effectively and both their inter-particle distance and size are large [102]. They also suggested the use of cold work before aging to enhance the age hardening response since it would increase the number density of the dislocations and number of twins for heterogeneous nucleation in the lattice defects. Also, some research has been oriented towards nucleation and growth, morphology, location and orientation of precipitation [107, 117, 129, 130] and interaction of twinning with the precipitation [131-133]. Only pockets of research have focused on severe plastic deformation of the alloys but very few of them studied the mechanical behavior of the alloys under uniaxial conditions [107, 108, 134, 135]. Hence, a dedicated effort to correlate the effect of strain imposed by thermo-mechanical processing on the precipitation kinetics, dynamic

recrystallization and mechanical properties of these alloys is needed. This research work is intended to give the overall picture of the relationship between thermo-mechanical processing and structure-properties.

The rationale behind choosing to compare a commercial alloy, AZ31B, with the two binary model alloys is that no new phase forms in Mg-Al-Zn alloys if the Al to Zn ratio is greater than 3:1. Beyond this ratio, addition of Zn would aid in the larger scale processing of the AZ61 and AZ91 alloys which are based on the Mg-6 wt.% Al and Mg-9 wt. % Al binary alloys, respectively, with additions of 0.5-1wt% Zn and 0.3wt% Mn [105, 136]. That is, the comparative processing-structure-properties relationships developed herein will be beneficial in delineating similarities and differences among the three systems that will allow for greater commercialization and utilization of magnesium and its alloys.

1.5 Organization of the dissertation

In this section, structure of the chapters of the dissertation will be described. In Chapter 2, the experimental methods used in this study will be discussed which included material preparation, thermo-mechanical processing, specifics of material characterization techniques and mechanical testing along with a description of the physics behind Kolsky/split-Hopkinson Pressure Bar (SHPB). In Chapters 3, 4, and 5, experimental results with respect to AZ31B, Mg-6%Al and Mg-9%Al along with the discussion will be presented, respectively. Each of these chapters would exhibit the results in the following order: (a) optical microscopy (OM), (b) scanning electron microscopy (SEM) with electron back scattered diffraction (SEM-EBSD) results which describe in detail the texture, grain size, grain boundary character distribution

(GBCD), grain orientation spread (GOS), Schmid factor (SF), deformation mechanism, and dynamic recrystallization (DRX), (c) transmission electron microscopy (TEM) results which describe the effect of precipitation such as distinguishing the types of precipitates, particle stimulated nucleation (PSN), Zener pinning and their morphology, and (d) mechanical properties under compression at quasi-static and dynamic strain rates along with the interpretation of strain hardening rate and strain rate sensitivity. The last chapter of the dissertation will include a discussion and conclusions of the dissertation and will provide ideas about potential future work.

CHAPTER 2: EXPERIMENTAL METHODS

In this chapter, the material processing, microstructural characterization and mechanical testing of samples studied in this dissertation will be addressed. This work primarily focuses on three Mg alloys: AZ31B (Mg-3%Al-1%Zn), Mg-6wt.% Al and Mg-9wt.% Al. These materials were solutionized, then hot rolled in a confined manner and quenched. Microstructural characterization using optical microscopy (OM), scanning electron microscopy (SEM) with electron backscattered diffraction technique (EBSD) and mechanical properties under quasi-static (strain rate $\sim 1.0 \times 10^{-3} \text{ s}^{-1}$) and dynamic (strain rate $\sim 1 \times 10^3 \text{ s}^{-1}$) Kolsky bar compressive loading conditions were investigated for samples confined rolled at different temperatures.

2.1 Material processing

Three different Mg alloys were procured, processed through severe plastic deformation, i.e., confined rolling, and analyzed in this study. AZ31B was procured from Magnesium Elektron North America, Inc. as ingots, the binary alloys of Mg-6 wt.% Al and Mg-9 wt.% Al were prepared by Dr. Zhigang Xu's group in NC A&T State University. Although these materials were procured from an external source/collaborator, it is worth mentioning that all the further processing, microstructural characterization, and mechanical testing was done by the author along with the analysis and discussion of results. The detailed processing steps for these alloys are as follows:

2.1.1 Melting and casting of binary alloys

Mg-x Al (x=6,9) alloys were fabricated by melting high purity Mg (99.97%, US Mg) and Al (99.99%, Alfa Aesar) at 1003K and cast into a pre-heated steel permanent mold

(fig. 2.1). Both melting and casting operations were performed in an ultra-high Argon environment chamber (commonly referred to as glove box). Pure Mg ingot was completely melted at 983K before soaking pure Al ingot for 10min without stirring. Then the whole mixture was stirred for 15min continuously for homogenization after which temperature was raised to 1003K and held for a further 30 minutes. After this step, it was poured through a ceramic filter into a horizontal steel mold (preheated at 523K). The cast structure was allowed to cool down in the same argon atmosphere.

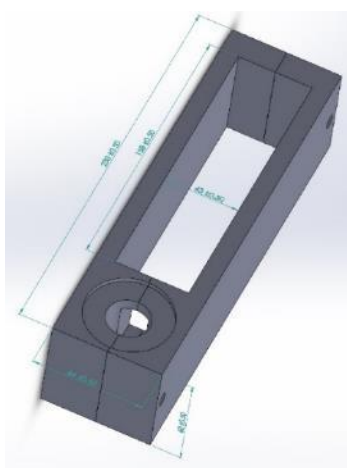


Figure 2.1 Schematic of the steel permanent mold used for casting the binary alloys

2.1.2 Solution treatment

The following procedure was the same for all three ingots. The as-received ingots were first solutionized at 723K for ~24 hours in a muffle furnace under Argon atmosphere (to prevent oxidation of the samples), quenched and checked for microstructural homogeneity in an optical microscope subsequently. Then, they were cut out into 50 mm (L) \times 10mm (W) \times 10mm (H) specimens for the subsequent confined rolling process. It was made sure that the edges of the sample were rounded by grinding to prevent the sharp corners acting as stress concentrators. Each sample was placed inside

a brass tube of ~14mm diameter such that edges of the sample were in contact with the inner surface of the tube and hammered to seal on both the ends.

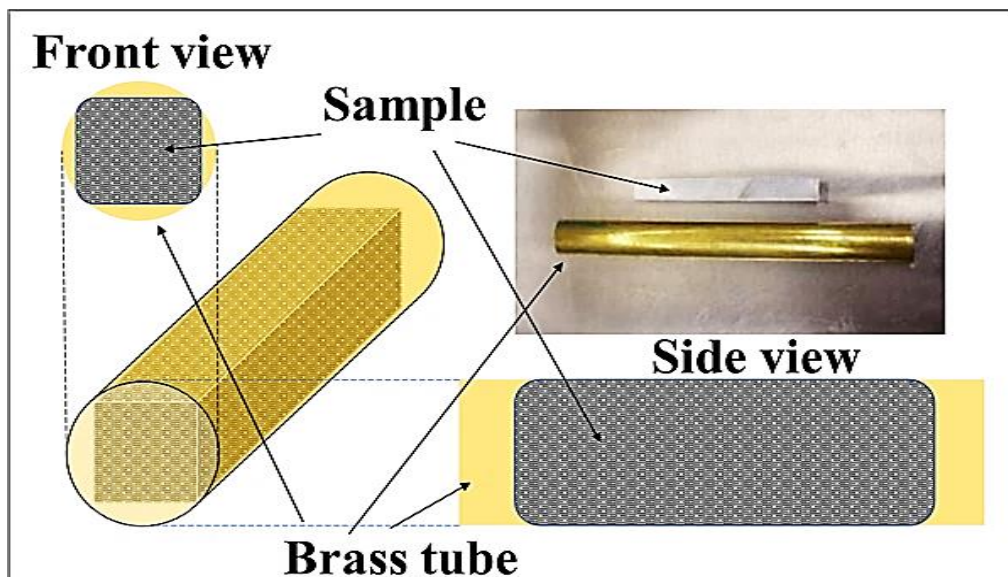


Figure 2.2 Schematic illustration of confined sample in brass tube

A schematic illustration of the confined rolling setup is given in figure 2.2. This sample-tube set-up was then heated in a muffle furnace at various temperatures such as 423K, 448K, 473K, 523K, and 573K for AZ31B; and 473K, 523K, and 573K for the binary alloys respectively. An allowance of 288K was given to account for the temperature drop when the set-up was transferred from furnace to the rolling machine. The samples were rolled until a total of 55%-60% thickness reduction was attained in stages, comprising of 2% thickness reduction per stage, and soaking of samples for 5-10 minutes in the furnace in between the rolling stages to ensure uniformity of temperature throughout the sample and process. Once the rolling was done, the sample was quenched to room temperature. Once the samples were extracted from the tube, they were cut into various sizes as given in table 2.1 below for microstructural observation and mechanical testing from the location provided in fig. 2.2. The sample

from outer 0.5-1mm from all the sides was discarded and not taken for microstructural characterization and mechanical testing as shown in fig. 2.3.

Table 2.1 Size of samples required for microscopy and mechanical property testing

Purpose	Size
Optical microscopy	5×5×5 mm
SEM and EBSD studies	3×3×5 mm
Micro-hardness measurement	3×3×5 mm
Quasi-static compression testing	2.5×2.5×5 mm
Kolsky bar compression testing	2.5×2.5×2 mm

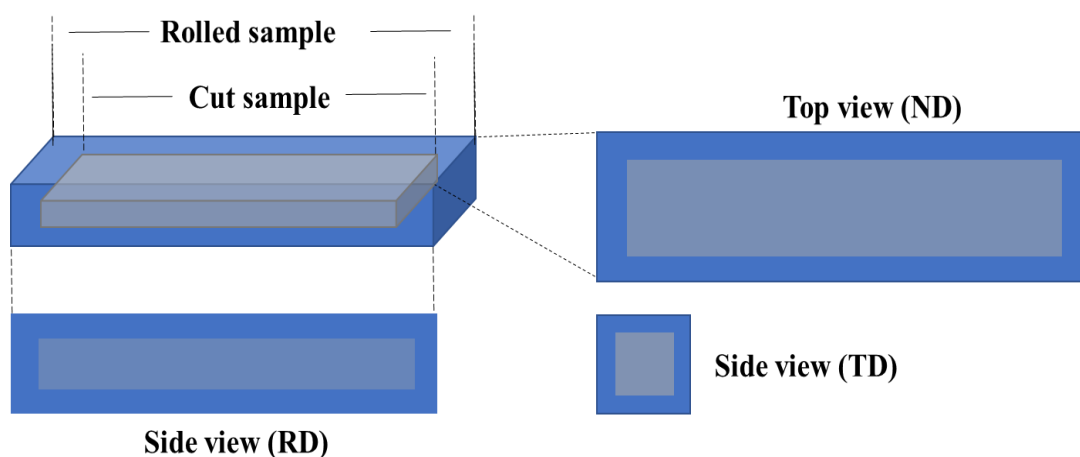


Figure 2.3 Schematic illustration of sectioning of a sample from rolled samples

2.2 Material characterization and mechanical testing

2.2.1 Optical microscopy (OM)

The cut samples underwent grinding and polishing to attain a mirror finish before etching to observe the microstructure through OM. Firstly, the samples were manually ground progressively using abrasive papers purchased from LECO Corporation with

SiC particles from grit size of 320 (~35 μm), 400 (~22 μm) and 600 (~15 μm). They were ground in linear motion in one direction (90° to preexisting scratches) until old scratches were removed and new scratches were formed in the perpendicular direction. Grinding was followed by polishing using Ecomet polishers with a wheel speed of 100rpm. First, the sample was polished with SiC abrasive paper with grit size of 1200 (~5 μm) using anhydrous alcohol (as a water-free polishing lubricant and rinsing agent to prevent oxidation) followed by polishing on an imperial polishing cloth using 0.3 μm Al₂O₃ suspension until a mirror finish was obtained. Both the polishing cloth and suspension were purchased from LECO Corporation. These two steps were followed by etching using picric-acetic solution (10ml acetic acid, 4.2g picric acid, 10ml distilled water, and 70ml Ethanol for AZ31B; 5ml acetic acid, 6g picric acid, 10ml distilled water and 100ml Ethanol for Mg-6%Al; and 1ml Nitric acid, 30ml Isopropyl alcohol for Mg-9%Al). The etched surface was then observed through Olympus BX51 optical microscope.

2.2.2 Scanning electron microscopy (SEM)- Electron Backscattered Diffraction (EBSD)

The procedure for preparing samples for SEM-EBSD was done in 3 steps: polishing, etching, and ion milling. The samples were polished on a diamond lap disc containing 30 μm , 15 μm , 9 μm , 6 μm , 3 μm , and 1 μm particles progressively, followed by polishing using a polishing cloth with 0.3 μm Al₂O₃ particles as suspension using the Allied High Tech Techprep 8" polishing grinding system & Multiprep head #15-2000. These steps were followed by further polishing in the ion milling with an accelerating voltage of 3kV and 3°, and 2kV for 20min (Fischione, Model1061 SEM Mill). EBSD

observation was conducted on a HITACHI SU8000-SEM equipped with an OXFORD SYMMETRY system operating at 15kV with a step size of 0.5~1.5 μ m. Fractography or post-loading examination of the samples was also conducted using JEOL JSM 6480 SEM operated at 20kV. Different failure mechanisms based on deformation mechanisms would be discussed in terms of microstructure and fracture modes of the failed samples.

2.2.3 Transmission electron microscopy (TEM)

The confined rolled samples were examined through a JEOL JEM 2100 TEM operated at 200kV. They were studied in both the bright field (BF) and dark field (DF) mode and selected area diffraction (SAD) patterns were also taken to identify the zone axis and phases. They were first cut into ~1mm thick samples using a diamond saw and followed by mechanical grinding up to a thickness of 60-80 μ m after which they were sectioned into 8mm discs using a mechanical cutter. The discs were dimpled using a Cu wheel with diamond paste containing 9 μ m particles up to a thickness of 25-30 μ m and polished further to mirror finish using a leather wheel with diamond paste containing 0.5 μ m particles (Model 656, Gatan). This was followed by final thinning to electron transparency using a Precision ion polishing system (PIPS, Gatan) with a gun angle of 5°.

2.2.4 Mechanical testing

Three different types of mechanical properties were tested: micro-hardness, quasi-static compression, and dynamic compression. Micro-hardness measurement was done using Wilson series 400 Knoop/Vickers micro-hardness testing system at a load of 0.5kg. Quasi-static (Strain rate of 10⁻³ s⁻¹) compression tests were done using

INSTRON model 5582 Universal Testing Machine. The constant strain rate in this case was achieved by controlling the velocity of lower compression head by giving the desired moving distance and time while holding the upper compression head. Dimension of quasi-static compression sample was 2.00mm×2.00 mm×5.00mm with a gauge length of 5mm. A lubricant was applied at both the loading faces to reduce the effect of friction. MTS Test Suite software was used to record the load and displacement in this experiment. Dynamic compression (strain rate of $\sim 10^3 \text{ s}^{-1}$) tests were done using desktop compression Split-Hopkinson Pressure Bar (SHPB) or Kolsky bar system. Dimension of dynamic compression sample was 2.5mm×2.5 mm×2.00 mm with a gauge length of 2.00mm. A similar lubricant was used for this test as well to prevent friction effects. For each shot, the incident, reflected, and transmitted signals were recorded. To ensure repeatability and minimize experimental error, at least 6-8 samples were tested in the same conditions for both the tests to reduce experimental error. Since the theory behind common optical/electron microscopy techniques and mechanical testing methods are well known, only the working principle of dynamic compression testing is chosen henceforth to be discussed in detail in the upcoming section.

Working principle of SHPB or Kolsky bar system

In quasi-static deformation, a static equilibrium is present, that is, any element in the body has a summation of forces acting on it close to zero. When deformation is imparted from the outside at a higher rate, one portion of the body gets stressed and other portion is not stressed yet (stress must travel through the body). Dynamic deformation involves wave propagation, whereas quasi-static deformation can be

considered as a series of equilibrium states that can be solved by equations of mechanics of materials. The compression version of Kolsky bar was the original set-up by Herbert Kolsky in 1949. The Kolsky bar in compression is also widely known as split-Hopkinson pressure bar (SHPB) in memory of John Hopkinson who conducted rupture tests of an iron wire by impact of drop weight in 1872 and his son, Bertram Hopkinson who invented a pressure bar to measure the pressure produced by high impact explosives or high-speed bullets in 1914. However, Kolsky was the first person to extend the Hopkinson bar technique to measure the stress-strain response under impact loading conditions. At that time, stress waves in the bars were measured using condenser microphones. A standard measurement technique, that is, the strain gage technique was developed to measure the stress waves. Also, the same group used a gun to launch the projectile (striker bar) to impact the incident bar, thereby generating a trapezoidal shaped pulse [137-141].

There are three major components to a Kolsky bar system: a loading device, bar components, and a data acquisition and recording system as schematically shown in fig. 2.4.

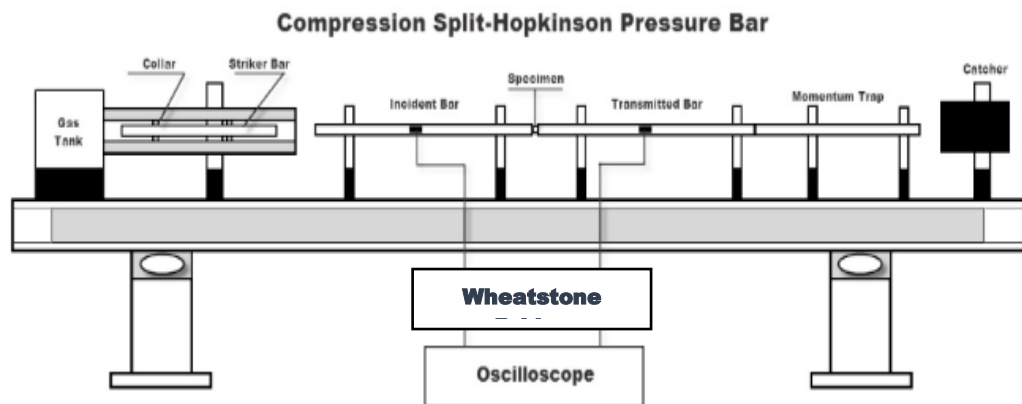


Figure 2.4 Schematic diagram of the major components of the Kolsky bar system [139]

The most common method for dynamic loading is to launch a striker impacting on the incident bar. The striker is launched by a sudden release of compressed air or a light gas in a pressure storage vessel (gas gun) and accelerates in a long gun barrel until it impacts one end of the incident bar. This dynamic loading method provides a controllable and repeatable impact on the incident bar in comparison to the static loading method where the incident bar is preloaded. The loading duration is proportional to the length of the striker. The bar components consist of incident bar, transmission bar and momentum trap device at the end. Since the stress waves in the bars are measured by surface strains, the bar material should be linearly elastic with a high yield strength. The incident bar should be at least twice as the striker to ensure incident and reflected waves do not overlap. The specimen is sandwiched between the incident and the transmitted bars aligned with the common axis of the bar system. For data acquisition, two strain gages attached symmetrically on the incident and transmitted bar conditioned by a Wheatstone bridge in turn connected to an oscilloscope. The incident and the reflected pulses are measured by the strain gages in the incident bar whereas the transmitted pulses are measured by the ones in the transmitted bar [138, 139]

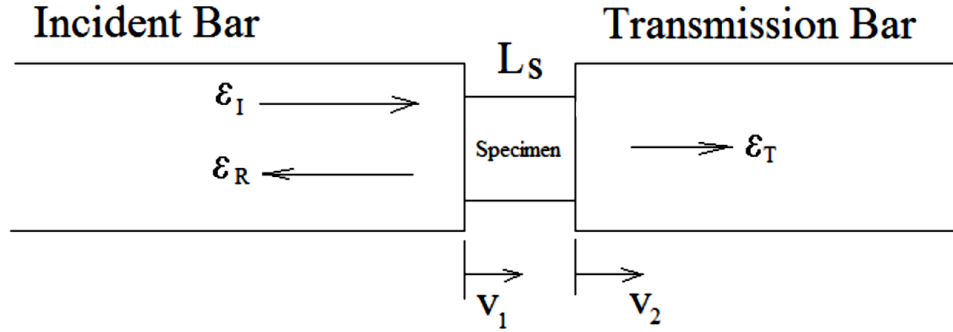


Figure 2.5 Schematic diagram of the strain components in Kolsky bar system [138, 139]

If the stress waves propagate in both the incident and transmission bars without dispersion, particle velocities at both the ends of the specimen related to the three measured strain pulses (through one dimensional stress wave theory)

$$v_1 = C_B(\epsilon_I - \epsilon_R) \quad (2.1)$$

$$v_2 = C_B \epsilon_T \quad (2.2)$$

where I, R, T represent the incident, reflected, and transmitted pulses respectively (fig. 2.5). The average engineering strain rate and strain in the specimen are

$$\epsilon = \frac{v_1 - v_2}{L_s} = \frac{C_B}{L_s} (\epsilon_I - \epsilon_R - \epsilon_T) \quad (2.3)$$

$$\dot{\epsilon} = \int_0^t \epsilon dt = \frac{C_B}{L_s} \int_0^t (\epsilon_I - \epsilon_R - \epsilon_T) dt \quad (2.4)$$

where L_s is the initial length of the specimen. The stresses in both the ends is calculated with the following elastic relations.

$$\sigma_1 = \frac{A_B}{A_S} \cdot E_B (\epsilon_I + \epsilon_R) \quad (2.5)$$

$$\sigma_2 = \frac{A_B}{A_S} \cdot E_B \cdot \epsilon_T \quad (2.6)$$

where A_B and A_S are cross-sectional areas of bar and specimen respectively and E_B is the young's modulus of the bar material. Since the specimen is assumed to be under stress equilibrium in a Kolsky bar test,

$$\sigma_1 = \sigma_2 \quad (2.7)$$

$$\varepsilon_I + \varepsilon_R = \varepsilon_T \quad (2.8)$$

$$\varepsilon = -2 \frac{c_B}{L_S} \varepsilon_R \quad (2.9)$$

$$\varepsilon = -2 \frac{c_B}{L_S} \int_0^t \varepsilon dt \quad (2.10)$$

Thus, averaged specimen stress is given as,

$$\sigma = \frac{1}{2} (\sigma_1 + \sigma_2) = \frac{1}{2} \frac{A_B}{A_S} \cdot E_B (\varepsilon_I + \varepsilon_R + \varepsilon_T) \quad (2.11)$$

All the above equations were derived based on conservation of mass and momentum along with the assumption of one-dimensional wave propagation [137]. It should be noticed that dynamic mechanical properties of Mg alloys have drawn interest from the community only until recently [142-145].

CHAPTER 3: AZ31B

In this chapter, the research work on rolled AZ31B will be discussed in detail in the context of its microstructure using optical and electron microscopy followed by mechanical behavior under compression in quasi-static and dynamic strain rates. The material will also be studied for texture, deformation and dynamic recrystallization mechanisms using EBSD technique. Since volume fraction of precipitates is expected to be quite low for these alloys, effect of precipitation will not be studied elaborately in comparison to the next two chapters about Mg- 6 wt.% Al and Mg- 9 wt.% Al. Also, since it is a commercial alloy, extensive research has already been made on this subject and hence, the results would be specific only to the effect of confined rolling on these alloys.

3.1 Optical microstructure

Fig. 3.1 depicts the optical microstructure of AZ31B before and after rolling at different temperatures ranging from 150°C to 300°C along the normal direction (ND). The average grain size of the baseline solutionized sample was coarse (~100µm). The average grain size of the rolled samples were observed to be smaller in comparison to the baseline sample and progressively increases as rolling temperature increases. Initial observations of samples rolled at lower temperatures ($\leq 200^\circ\text{C}$) showed extensive twinning in the material. The twins can also be noticed to host dynamically recrystallized fine grains. Also, new dynamically recrystallized grains were observed along the grain boundaries. Typically, grain boundaries act as initiation points for recrystallization followed by expansion into the un-recrystallized grain volume. Fluctuations in grain boundaries in the form of

serrations and bulges develop followed by which new grains get generated. This microstructure is commonly known as necklace structure.

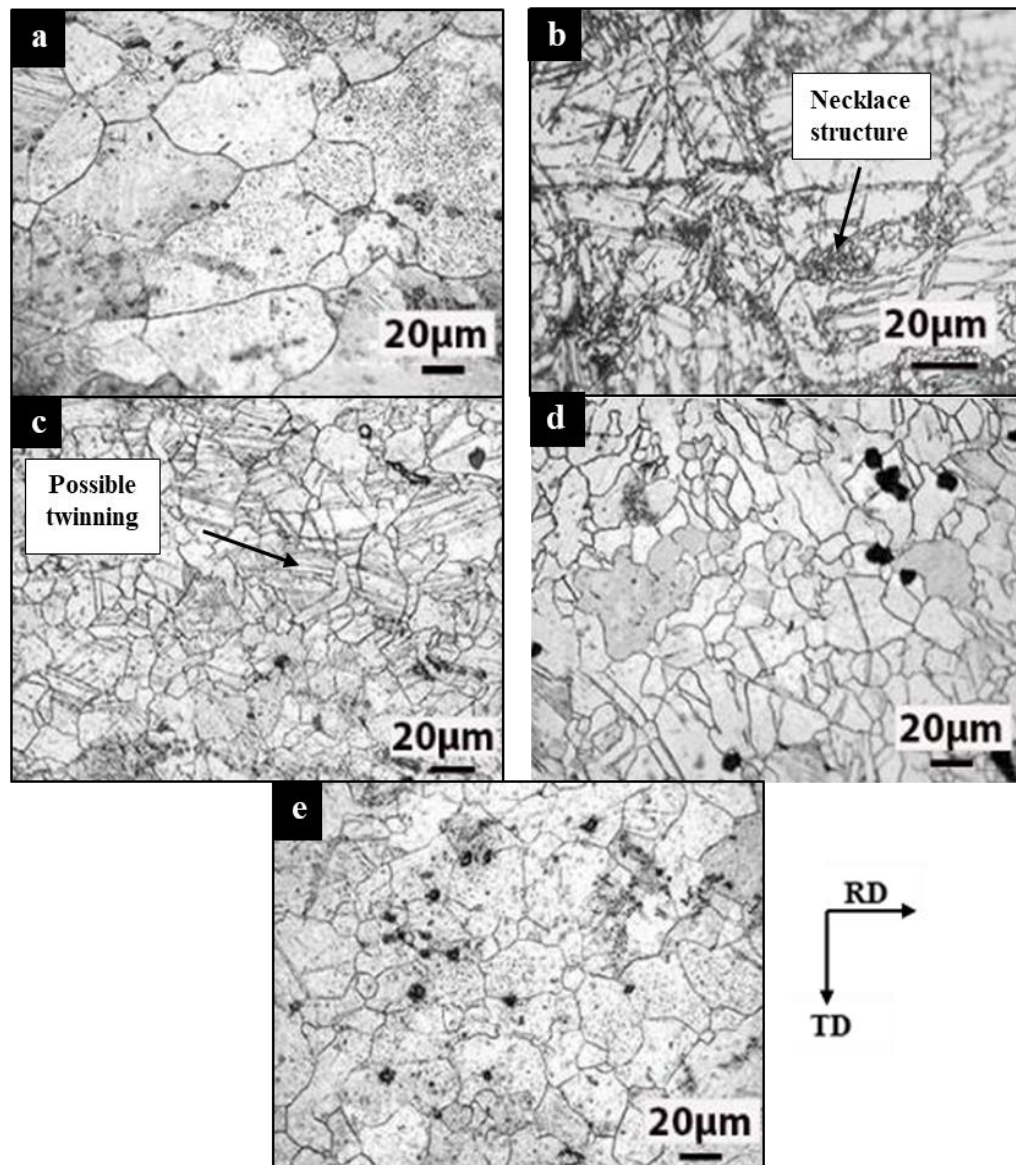


Figure 3.1 Optical micrographs of AZ31B alloys (a) before rolling and after confined rolling at (b) 150°C, (c) 200°C, (d) 250°C, and (e) 300°C along normal direction (ND)

Consistent with the schematic illustrating the microstructure development during necklacing process [146, 147] as shown in fig. 3.2, it can be observed that the samples rolled at 150°C (fig 3.1b) adorned a necklace structure with equiaxed

recrystallized grains along the grain boundaries. The mechanism of necklace structure development is as follows: At low temperatures, twinning and basal slip occur preceding other mechanisms to accommodate deformation. As strain increases, dynamic recrystallization (DRX) occurs in areas of high misorientations due to accumulation of dislocations at defects such as twins and grain boundaries. These newly formed fine grains deform more easily than the grain core and hence repeatedly undergoing recrystallization.

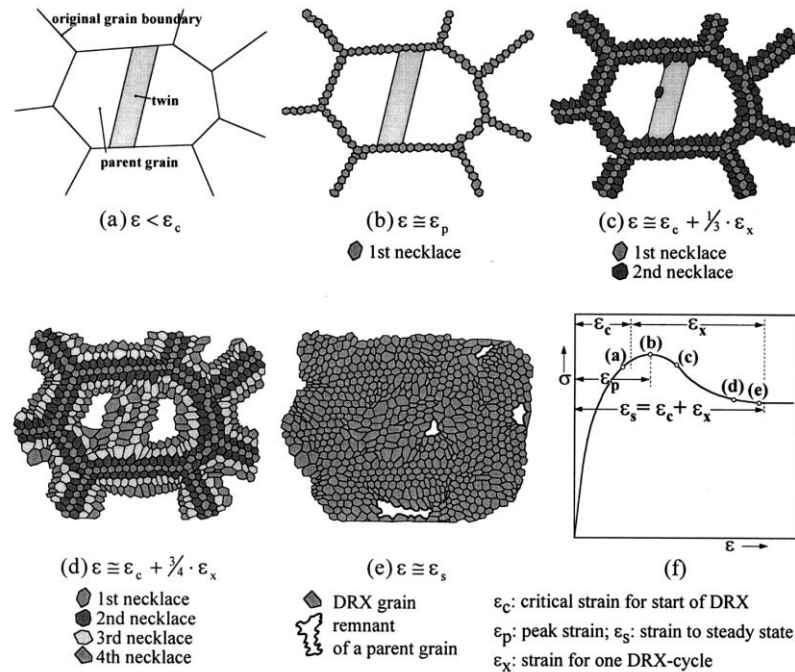


Figure 3.2 Schematic representation of microstructural evolution by necklace formation: (a) Only the parent grain is present at strain $\varepsilon < \varepsilon_c$ (b) First layer of necklace structure forms at grain boundaries (c) Second layer of necklace structure expands the recrystallization to the core of the grain (d), (e) expansion of necklace structure to consume whole interior of the grain and (f) the corresponding flow stress curve [147].

Barnett et al.[95] reported the effect of initial grain size and strain on average grain size of dynamically recrystallized grains. They established that with a high enough strain and fine-grained baseline material, impingement of necklace grains on the

opposite side of the grain resulted in a fine-grained microstructure. In this case, initial fine grain size increases the kinetics of DRX while coarse grains cause higher working loads and partially recrystallized microstructures. Necklace structures are quite common in Mg alloys and were reported by a few other authors as well [148-150]. The size of the dynamically recrystallized grains at lower temperatures cannot be determined accurately due to the resolution limitations of the optical microscope and hence it was deemed that an SEM-EBSD technique was needed to resolve them.

3.2 SEM- EBSD studies

This section consists of results that can pertain to grain orientation, average grain size, texture, grain boundary distribution, recrystallization and deformation mechanisms etc. ND-IPF maps in fig. 3.3 show basal texture i.e., c-axis of most of the grains are parallel to the normal direction. The color bar shown in fig. 3.3 represented as a standard stereographic triangle corresponds to the crystallographic orientation of each grain (red, green and blue represent (0001), $(\bar{1}2\bar{1}0)$ and $(01\bar{1}0)$ respectively). The micrographs from the samples rolled at 150°C and 200°C seem to draw more interest due to fine grains nucleating along the grain boundaries (necklace structure) in the former to a fully recrystallized structure in the latter. In the case of this sample, to attain a fine fully recrystallized microstructure, a rolling temperature between 150°C-200°C should be chosen to attain better mechanical properties. The ND-IPF maps show similar trend as optical micrographs for all the rolling temperatures. There is a considerable decrease from the baseline grain size

after confined rolling and progressive increase in grain size as rolling temperature increases (fig 3.4).

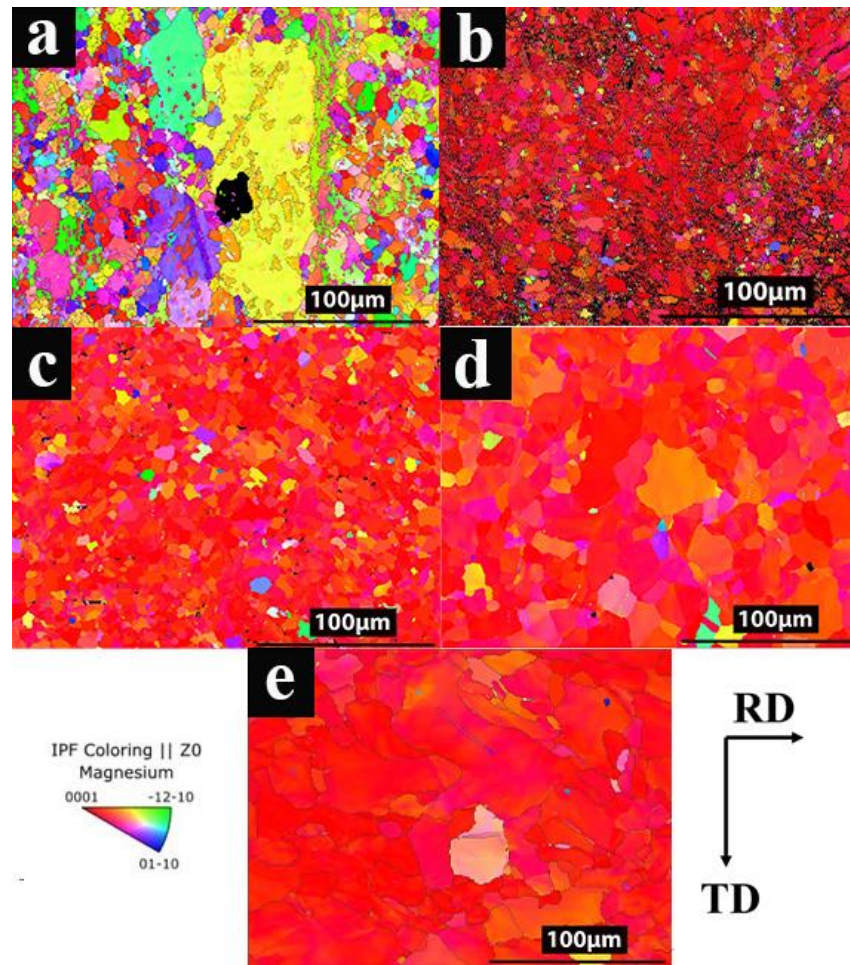


Figure 3.3 ND- Inverse pole figure (IPF) maps of AZ31B alloys confined rolled at (a) before and after confined rolling at (b) 150°C, (c) 200°C, (d) 250°C and (e) 300°C

Although there are a lot of discrepancies in the literature regarding grain sizes depending on processing parameters (reduction ratio, for instance), initial texture, etc., the average grain size of this alloy is in good agreement with the range of grain sizes obtainable from other severe plastic deformation methods such as equal-channel angular pressing (ECAP), Friction stir processing (FSP), etc. for AZ31B alloys as shown in fig. 3.5[151-153].

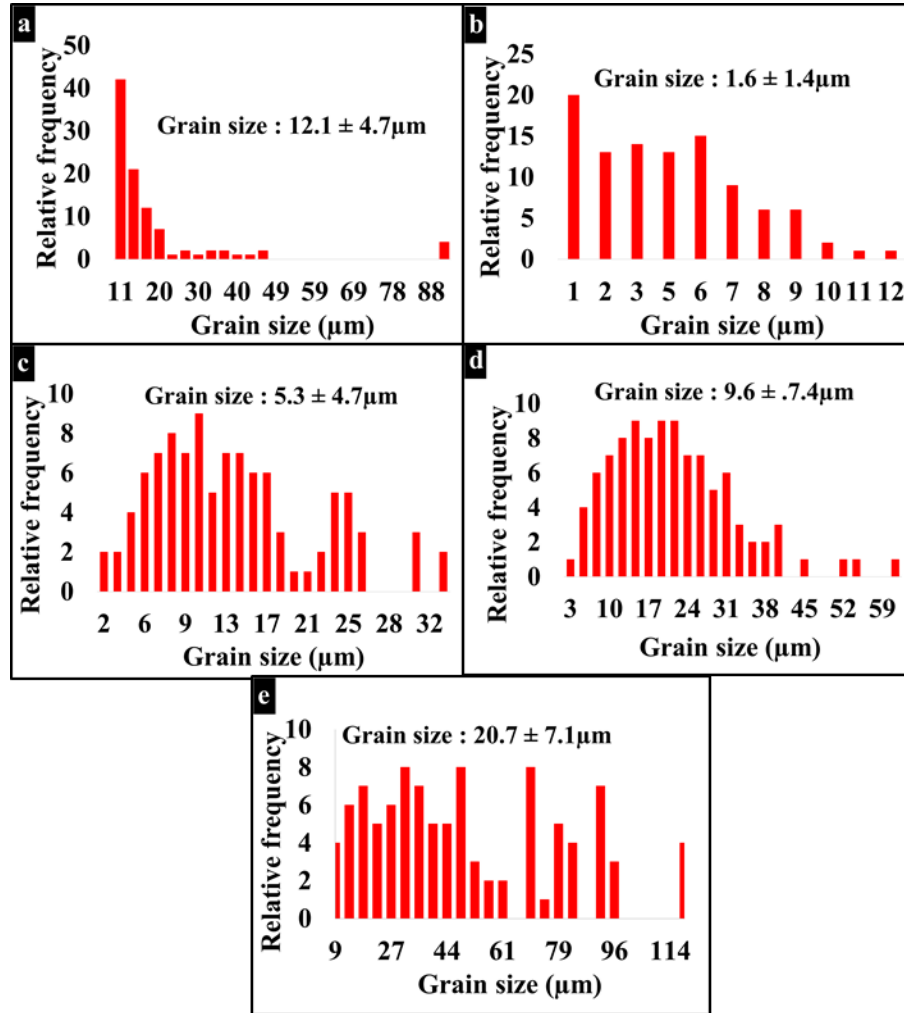


Figure 3.4 Grain size measurements along ND plane of AZ31B alloy confined rolled at (a) before rolling and after confined rolling at (b) 150°C, (c) 200°C, (d) 250°C and (e) 300°C.

This along with the average recrystallized grain size has been explained using Zener-Holloman parameter (Z) which gives the collective influence of strain rate ($\dot{\epsilon}$) and deformation temperature (T) as shown in equation 3.1 and 3.2.

$$Z = \dot{\epsilon} e^{\frac{Q}{RT}} \quad (3.1)$$

$$D_{DRX} = CZ^{\left(\frac{4}{n}-1\right)} \quad (3.2)$$

where R is the gas constant and Q is the activation energy required for deformation [95, 96, 149]

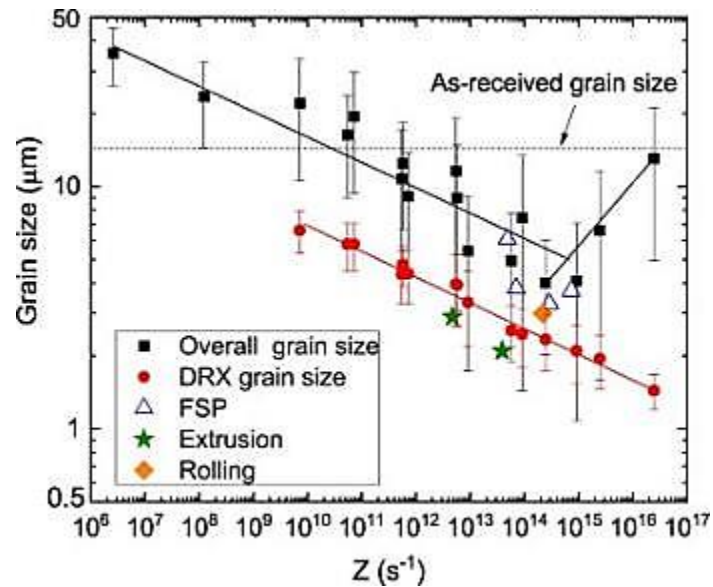


Figure 3.5 Relationship between various thermo-mechanical processing techniques with Z parameter and grain size for AZ31B alloys [95, 96, 149]

3.2.1 Texture

$\{0001\}$ and $\{10\bar{1}0\}$ pole figures of the baseline and as-rolled plates are given in fig. 3.6. The pole figures indicated a strong basal texture that was stabilized during processing which is characteristic of rolled Mg alloys [7, 151, 153-155]. There were no signs of randomization of texture although a slight shift in basal texture was observed. The textural intensity given in terms of multiple intensity of random orientation (MRD) number above the color bar next to the pole figures is the normalized probability density of a given orientation. The higher the number, the stronger texture and vice-versa. This value for samples rolled at 200°C was the lowest again reiterating the fact that the deformation assisted dynamic recrystallization is almost complete when rolled at this temperature.

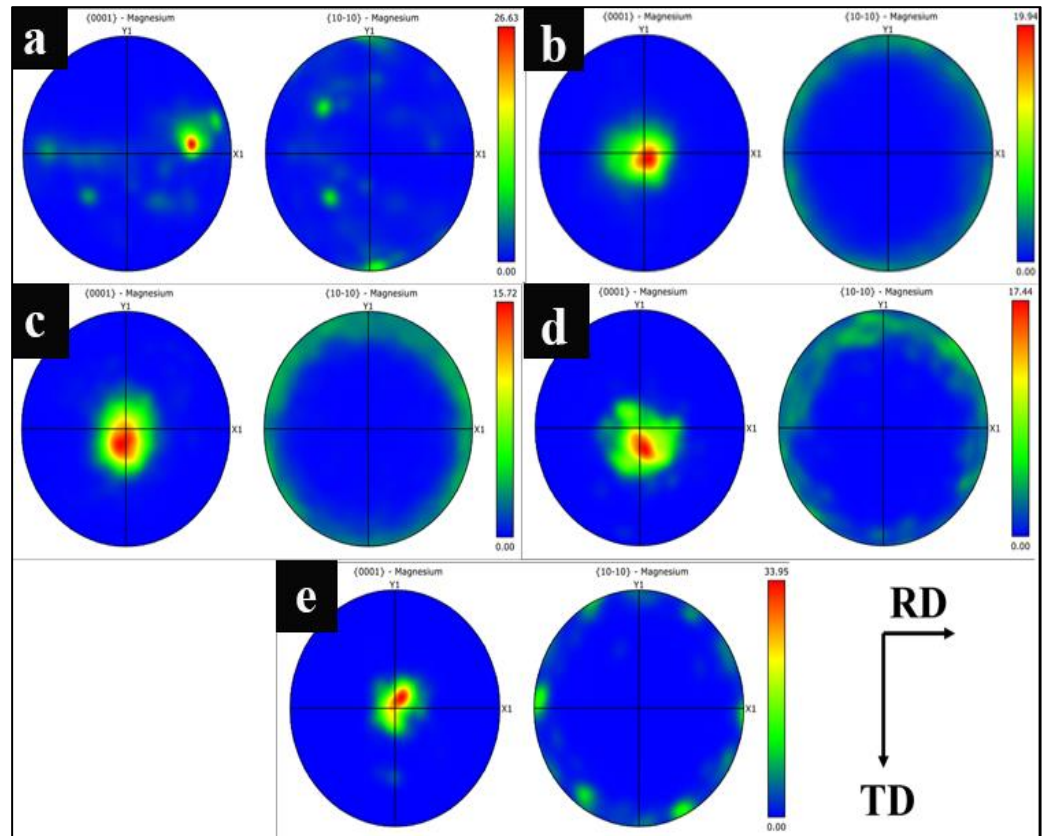


Figure 3.6 Texture intensity of $\{0001\}$ and $\{10\bar{1}0\}$ planes of AZ31B alloys (a) before and after confined rolling at (b) 150°C, (c) 200°C, (d) 250°C and (e) 300°C along ND

At 150°C, there was still a large portion of the microstructure that is deformed and yet to recrystallize hence the strong basal texture, although overall grain size is small ($\sim 1.6\mu\text{m}$) due to extremely fine recrystallized grains adorned in the form of necklace structure. It can be observed that the strong texture was slightly shifted towards the rolling direction (RD) for all sampled rolled above 150°C. This may be because of confined rolling accommodating thickness reduction along the rolling direction (RD) and restriction of movement along the transverse direction (TD). Textural intensity increased with increase with rolling temperature due to the easy

movement of non-basal slip systems promoting grain rotation along the direction of deformation [156].

3.2.2. Grain boundary character distribution (GBCD)

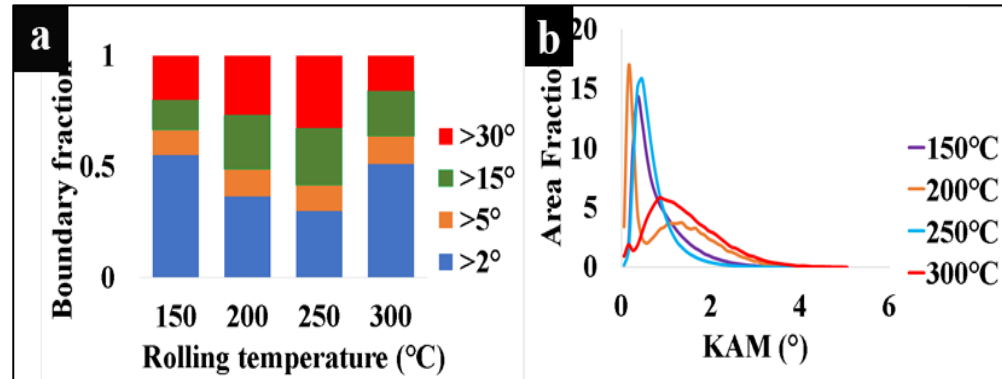


Figure 3.7 (a) Grain boundary distribution and (b) Kernel average misorientation distribution of AZ31B samples rolled at 150°C, 200°C, 250°C and 300°C along ND

The GBCD maps of confined rolled AZ31B alloys in fig. 3.7(a) showed a slightly wide variation in the proportion of low angle grain boundaries (LAGBs- grain boundary angle $<15^\circ$) to high (HAGBs- grain boundary angle $>15^\circ$). The fraction of low angle grain boundaries was the highest at 150°C and progressively decreased upto the rolling temperature of 250°C but then increased again at 300°C. The higher number of LAGBs at 150°C could be attributed to the early onset of recrystallization and necklace structure formation with the subsequent decrease attributed to grain growth. But the reason for increase of LAGBs in samples rolled at 300°C is still under speculation.

Kernel average misorientation (KAM) is generally used to assess local plastic strain or lattice distortion which correlates directly to the density of geometrically necessary dislocations, ρ and the associated stored energy (equation 3.3).

$$\rho = \frac{2KAM_{average}}{\mu b} \quad (3.3)$$

It is a pixel-based deformation coloring scheme and the value is a commonly used metric to quantify local lattice distortion or misorientation in the material. Average KAM values of all samples with rolling temperatures ranging from 150°C - 250°C were below 1 (fig. 3.7b) indicating that the structure contains DRX grains because these grains form at the cost of stored energy provided by the sub-structures and for samples rolled at 300°C is 1.4 indicating high density of sub-structures formed in deformed grains. Although KAM values at 300°C were expected to be reduced due to grain coarsening and dynamic recovery, the values tend to be slightly higher and the reason needs further probing [157, 158].

3.2.3 Average misorientation

Fig. 3.8 represents the misorientation angle distribution of confined rolled AZ31B samples. The relative fraction of grains with misorientation angle $<50^\circ$ is higher in comparison to grains with misorientation angle $>50^\circ$ corroborating the theory that confined rolling helps in breaking coarser grains to form a finer microstructure. As temperature increases, grains with $30\pm 5^\circ$ misorientation progressively increase with grains having misorientation of $\sim 90\pm 5^\circ$ decreases. The fraction of $30\pm 5^\circ$ [0001] grain boundaries correspond to newly formed deformation induced dynamic recrystallization occurring in materials. The presence of $86\pm 5^\circ$ tensile twins (TTWs) $\{10\bar{1}2\} < 10\bar{1}1 >$ formed to accommodate extension strain along the c-axis [159]

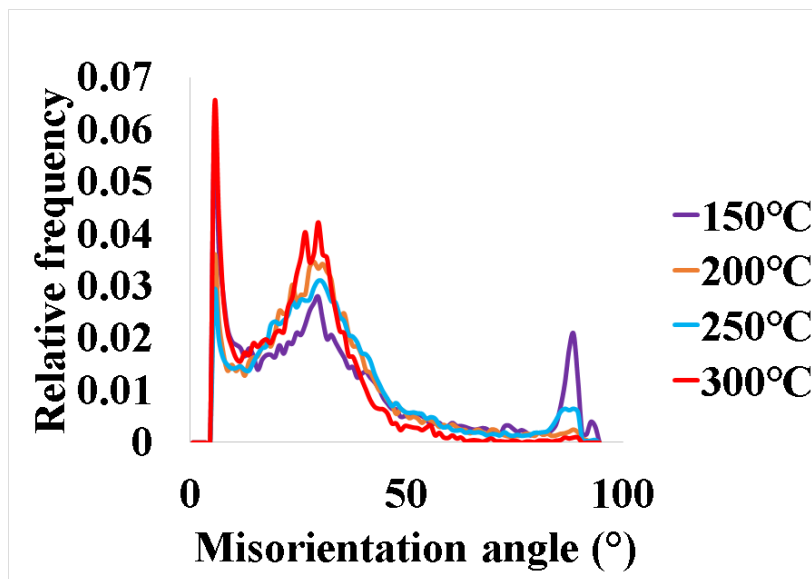


Figure 3.8 Misorientation angle distribution showing progressive increase and decrease of $30\pm 5^\circ$ misorientation and $86\pm 5^\circ$ twin boundaries respectively as rolling temperature increases.

3.3 Deformation mechanism

This section attempts to study in detail about the dynamic recrystallization mechanisms involved and possibility of slip or twin systems aiding in the slight texture modification of this alloy rolled at various temperatures. The extent of recrystallization can be analyzed using the grain orientation spread values obtained through EBSD. This material also exhibited twin based recrystallization along with the grain-based recrystallization mechanisms which will be discussed further in this section.

3.3.1 Grain Orientation Spread (GOS):

GOS is the average difference in orientation between orientation at each point in the grain and the average orientation of the grain. For example, accumulation of dislocations leads to higher average orientation deviation in the grain, thereby characterized by high GOS value and vice-versa for well- annealed materials where

low GOS value is observed due to grains being free of excessive dislocations due to annihilation and rearrangement of dislocations.

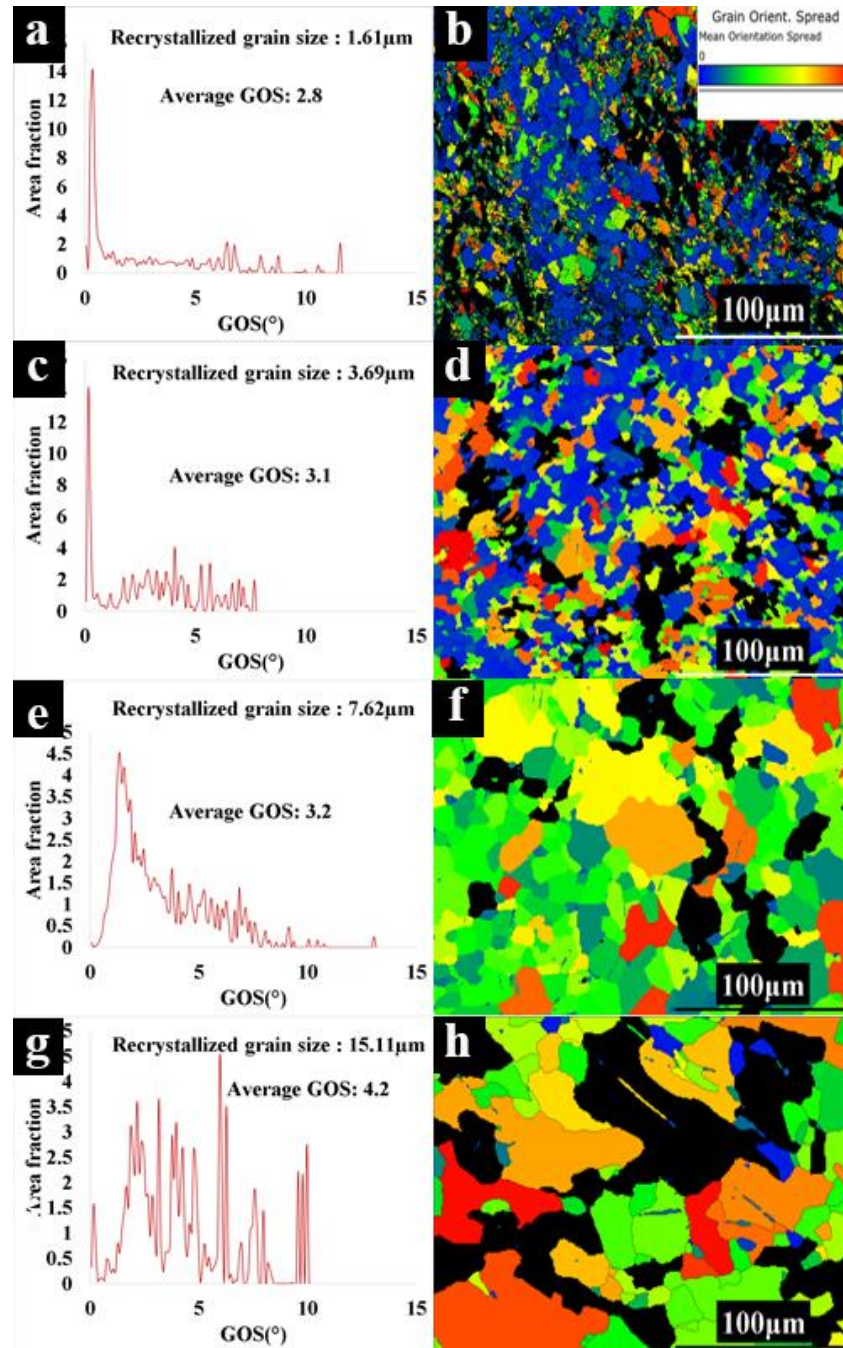


Figure 3.9 (a) – (d) GOS map and (e) – (h) corresponding recrystallized area partitioned using $GOS < 5^\circ$ criterion of samples along ND rolled at 150°C, 200°C, 250°C, and 300°C respectively

Although GOS value $\leq 2^\circ$ is a well-documented approach to identify newly recrystallized grains as per literature, GOS $\leq 5^\circ$ will be used in this thesis since it doesn't consider coarsening of grains which have recrystallized at earlier stages of deformation. As seen in fig. 3.9 (a), samples rolled at 150°C exhibited the same average grain size as that of recrystallized grain size proving that recrystallization of AZ31B is near completion close to this temperature. Recall, at 200°C, complete recrystallization was apparent from the optical and SEM micrographs. Hence, 175°C could be an interesting temperature to be chosen for achieving better microstructure to achieve the desired properties. From fig. 3.9 (b)-(d) it can be deciphered that the average recrystallized grain size increases as rolling temperature increases. Also, the average GOS value increases with increase in rolling temperature indicating grain coarsening as temperature increases. There are still pockets of unrecrystallized areas due to the possibility of uneven distribution of stored energy prior to hot rolling required to initiate recrystallization.

3.3.2 Dynamic recrystallization (DRX) mechanism:

The variation of DRX mechanisms with temperature is shown in fig. 3.10. Continuous dynamic recrystallization (CDRX) mechanism which involves recovery through rearrangement of dislocations to form sub-grains and continuous absorption of dislocations in LAGBs to form HAGBs and eventually newly recrystallized grains was not found predominantly during confined rolling of AZ31B.

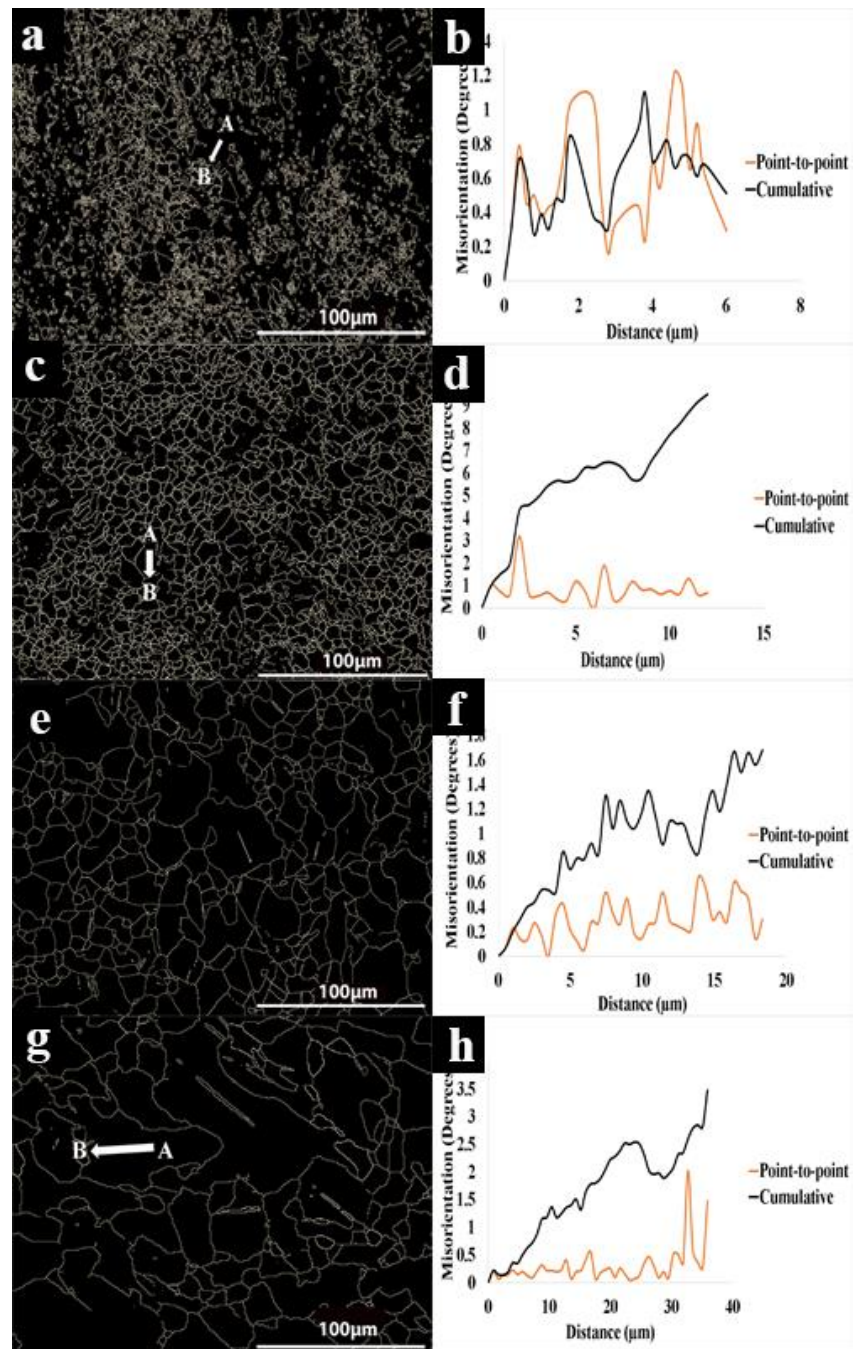


Figure 3.10 (a), (c), (e), (g) HAGB map of AZ31B samples rolled at 150°C, 200°C, 250°C and 300°C and (b), (d), (f), (h) the corresponding line profile of misorientations along the line AB in (a)-(d) respectively along ND

On the other hand, discontinuous dynamic recrystallization (DDRX) which is related to strain induced boundary migration involves nucleation at bulged and

serrated HAGBs and grain growth through grain boundary migration was prominent as seen in fig. 3.10.

A few authors reported that at intermediate temperatures of ~ 200 - 250°C , CDRX acts as the controlling mechanism whereas at a higher temperature of ~ 300 - 450°C , DDRX dominates the deformation process. But significant change of texture was not reported due to DRX irrespective of whatever mechanism occurs [150, 160, 161] making it an even tougher challenge to solve. Contrastingly, other authors reported the weakening of texture due to CDRX during extrusion of Mg-rare earth alloys and since the orientation of DDRX grains was ensuing from the parent grain, it was expected to retain the strong basal texture of the starting microstructure [162-165]. However, few other authors observed that rotated orientation of DDRXed grains from their parents' grains led to randomization of texture [163, 166]. Slight randomization of texture and lowering of textural intensity was observed in AZ31B alloys confined rolled at 150°C .

Apart from DDRX, twinning observed in the samples rolled at 150°C also contribute to the randomization of texture due to reorientation of the parent grains by $\sim 86.3^\circ$ [166]. Copious number of twins formed during deformation divides coarse grains by intersecting them. Such fragmented grains act as dislocation barriers which during further deformation influence grain rotation. In summary, both twinning and DDRX are believed to be two major contributors to the formation of non-basal textures and texture randomization.

Twin DRX was also observed in the alloys rolled at 150°C . Twins possess much higher stored energy (since dislocations cannot penetrate through twin

boundaries) in comparison with the matrix and hence act as favorable sites for DRX [166]. In the current study, the microstructure contains mostly $86^\circ \langle 11\bar{2}0 \rangle$ tensile twins as observed from the section 3.2.3. Since the average grain size is very close to the average recrystallized grain size, the general assumption is that some of these grain inside the twin region have also been recrystallized. These findings are substantiated by the work of Al Samman et al. (fig. 3.11a) with a good evidence for DRX inside twins and some un-recrystallized twins [160]. They found that those twins that recrystallized contained some amount of pre-existing LAGBs due to the dynamics of the process which would incorporate dislocations during further deformation and fragment the twin to form newly recrystallized grains. It was also remarked that those twins which did not recrystallize were either not favorably oriented for deformation and lacked LAGBs to multiply and form new HAGBs. In the current study, apparently most of the twins were favorably oriented for deformation and hosted recrystallized ultrafine grains as shown in fig. 3.11b.

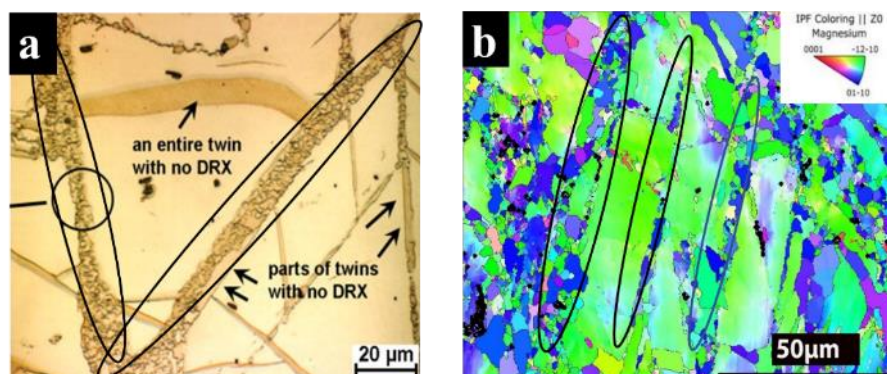


Figure 3.11 Evidence of recrystallization inside twins (marked) in AZ31B alloys (a) extruded at 200°C [160] and (b) confined rolled at 150°C in RD (this work).

In addition to twin DRX, the necklace structure which was discussed in section 3.1 of this chapter also contributed to texture randomization. Al Samman and co-authors defined this phenomenon as “Low temperature DRX.” They

observed the presence of serrated grain boundaries of coarse grains which discontinuously recrystallized by bulging. At higher temperatures, subsequently necklace layers formed and eventually caused complete DRX. It was speculated that this low temperature DRX was promoted due to the lack of easily activated slip systems, low stacking fault energy of magnesium, high grain boundary diffusivity etc. [160].

3.3.3 The special case of confined rolling at 175°C

The promising results of samples rolled at 150°C and 200°C raises curiosity about behavior of the material when rolled at an intermediate temperature between the two given temperatures. The rolling temperature was chosen to be 175°C and these samples were characterized with the necklace structure of DRX grains and contained numerous twins (which sub-divide the structure and recrystallize themselves) in turn refining the microstructure (fig. 3.12 (a)). Grain boundary map in fig 3.12 (b) revealing higher volume fraction of LAGBs ($<15^\circ$) ~79% in comparison to HAGBs ($>15^\circ$) and IPF maps along ND in fig. 3.12 (c) illustrate the almost completely recrystallized microstructure with some deformed and mostly DRXed grains sweeping the entire microstructure.

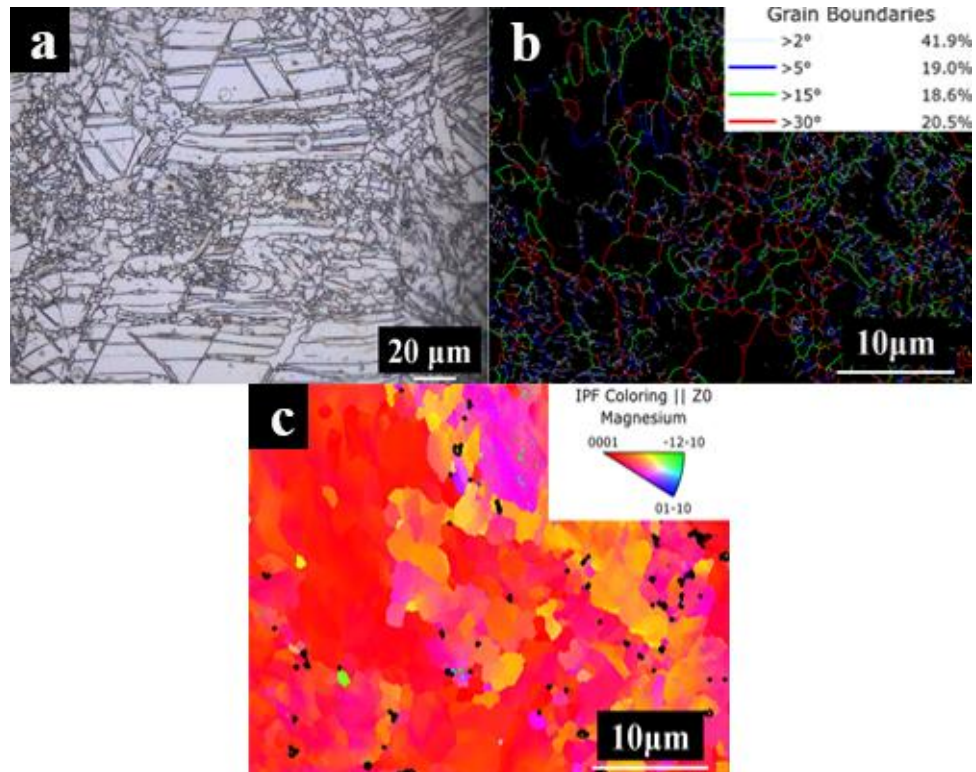


Figure 3.12 (a) Optical micrograph (b) grain boundary distribution (c) inverse pole figures with deformed and fine DRX grains along ND of AZ31B alloys rolled at 175°C

Looking at the duplex microstructure, this sample posed an interesting opportunity and it was expected to exhibit better mechanical behavior of these samples in terms of higher compressive strength and larger strain to fracture. A comprehensive analysis of the effect of rolling temperature on the mechanical behavior of this alloy is described in the upcoming section.

3.4 Mechanical properties under compression

3.4.1 Stress-strain behavior at different strain rates under compression

Fig. 3.13 represents the quasi-static and dynamic behavior of AZ31B alloys confined rolled at various temperatures. At quasi-static strain rates, there is a steep increase in strain hardening rate whereas in dynamic strain rates, it was at a gradual

pace. In comparison to the baseline alloys at quasi-static rates, the rolled alloys exhibited 1.5 times higher compressive strength, but malleability was halved.

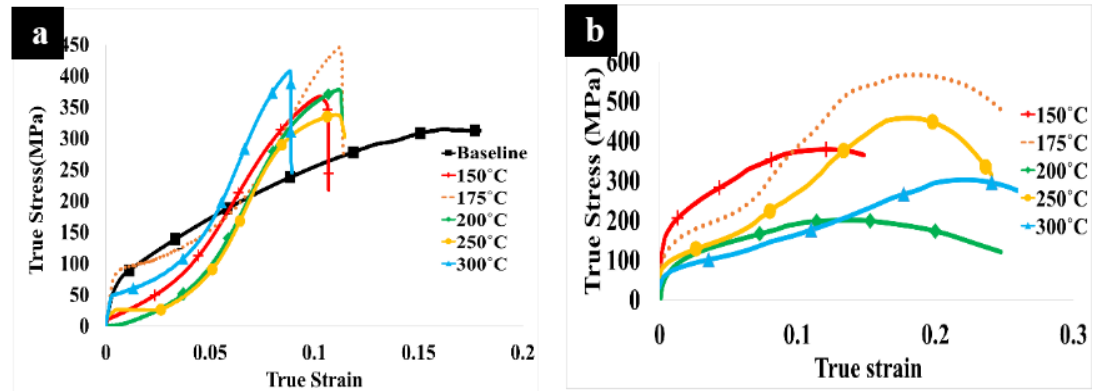


Figure 3.13 (a) Quasi-static and (b) dynamic compressive behavior of AZ31B alloys rolled at different temperatures along ND

Most of the rolled samples except the ones rolled at 175°C either didn't exhibit change (samples rolled at 150°C and 250°C) or exhibited strain rate softening i.e., decreased in compressive strength (samples rolled at 200°C and 300°C) with increase in strain rate. The behavior at 200°C is an outlier and may be attributed to the presence of inherent defects or flaws created in the material itself during casting. Usually, magnesium alloys demonstrate excellent strain rate hardening due to less time available for plastic deformation mechanisms to kick in and the abundant availability of deformation resistance force generated by the nature of the material [127, 167, 168] but in this alloy, it shows no strain rate dependence. However, increasing the strain rate increases the ductility of the alloy. Along with that, this alloy could be observed to deform significantly by twinning at both the strain rates signifying those non-basal planes were not evoked to accommodate plastic deformation.

3.4.2 Strain hardening rate and coefficient

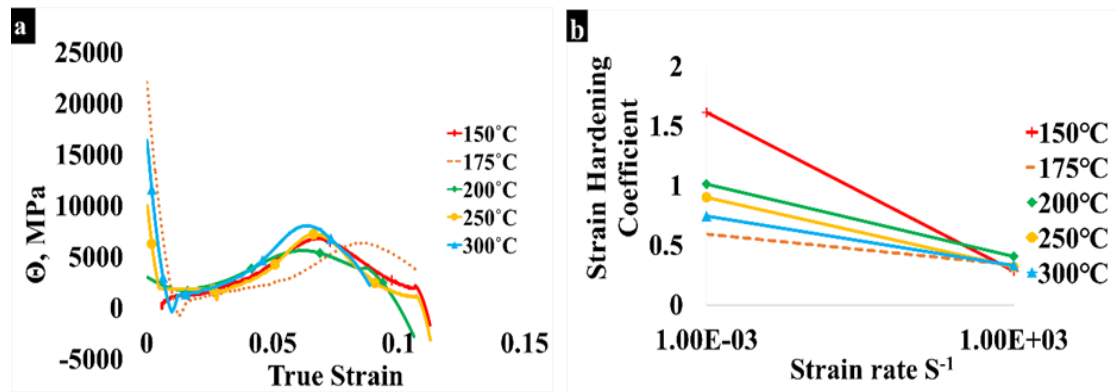


Figure 3.14 (a) Strain hardening rate and (b) Strain hardening coefficient of the AZ31B alloy under quasi-static conditions along ND.

Strain hardening rate of AZ31B confined rolled samples (fig. 3.14 (a)) decreases initially, then increase again slightly and finally decline with increase in strain. Similarly, the magnitude of strain hardening exponent of AZ31B alloys rolled at 150°C was the highest and possessed the maximum amount of plastic strain in quasi-static rates whereas other samples showed similar strain hardening tendencies.

At dynamic strain rates, the value of strain hardening exponent shows decreasing trend and lower values of plastic strain. The higher value of strain hardening exponent in samples rolled at 150°C at quasi-static rates can be attributed to the presence of extension twins. It was observed in literature that the extension twins grow quickly and consumed the whole grain and are not effective in refining grain size through Hall Petch effect. Therefore, their contribution to strain hardening is mainly through texture hardening rather than Hall-Petch kind hardening since they rotate grains into orientations with c-axis parallel to loading axis. Contribution of deformation twinning to strain hardening can be divided into three stages: (a) Strengthening by grain size reduction by forming twin boundaries, (b) glissile to sessile dislocation transformation in the twinned region, and (c) texture hardening or softening within new

twinned orientations. Few authors provided experimental evidence of improvement of flow strength from 115MPa to 150MPa around strain~0.065 where extension twinning was highly active [19, 169]. Presence of substantial amount of extension twins in confined rolled AZ31B alloys could be a rationale for their strain hardening behavior at lower temperatures.

3.4.3 Strain Rate Sensitivity (SRS)

As illustrated in fig. 3.15, the strain rate sensitivity of AZ31B alloys rolled at 150°C is the highest. The general trend is the decrease of SRS until 200°C after which it increases followed by its decline for samples rolled at 300°C. The drop in SRS trend from 150°C to 200°C can be attributed to the occurrence of extensive twinning produced to accommodate deformation in addition to basal slip in the absence of non-basal slip systems [170]. At increasing rolling temperature, the increase of SRS indicates completion of dynamically recrystallized grains formed due to the stored energy through activation of both basal and non-basal slip systems. Given the m values for this alloy ($m < 0.2$), it can be safely concluded that dislocation creep, i.e., dislocation motion in the lattice during deformation operates as climb controlled. Dislocation creep may operate as either glide-controlled creep ($m > 0.3$) or climb controlled creep ($m \sim 0.2-0.25$) [171].

The glide-controlled creep is a process of glide on slip planes in the case where solute atoms (such as Zn and Al in AZ31B) impedes dislocation movement. The climb-controlled dislocation movement is the climb through non-conventional dislocation motion over second phases. The conclusion of climb controlled creep process seems reasonable considering the lower volume fraction of precipitates (<2%) in AZ31B

alloys. Above 300°C, grain size increases dramatically and abnormally. As a result, dislocations are greatly reduced since non-basal dislocations are generated at the grain boundaries due to incompatibility strains. Hence, decrease of m-value due to coarser grains seem reasonable [171].

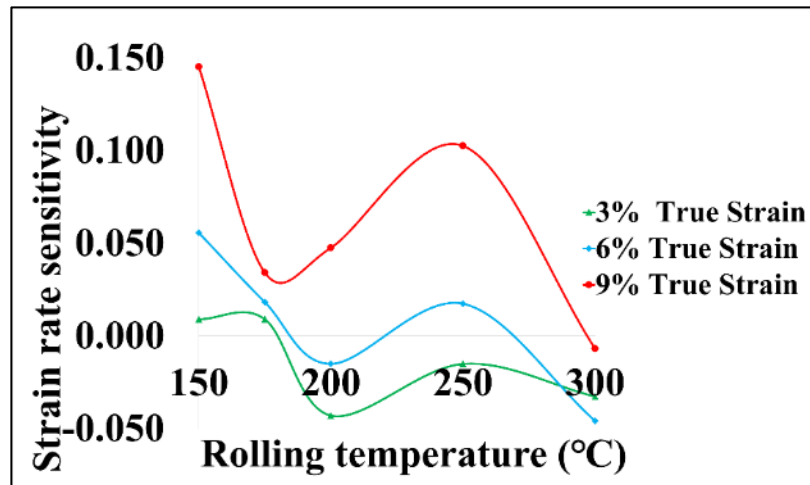


Figure 3.15 Strain Rate Sensitivity (SRS) of AZ31B alloy rolled at different temperatures along ND.

3.4.4 Fracture surface analysis under quasi-static compression

Fig. 3.16 shows fracture surface morphology of AZ31B tested under quasi-static conditions along ND at both macro and microscopic magnification levels. Since the dynamic tested samples were broken into bits and pieces, they could not be recovered for failure analysis. Initial observations of macroscopic details of fracture surface showed sample failing with fracture lines along 45° orientation with respect to the loading direction.

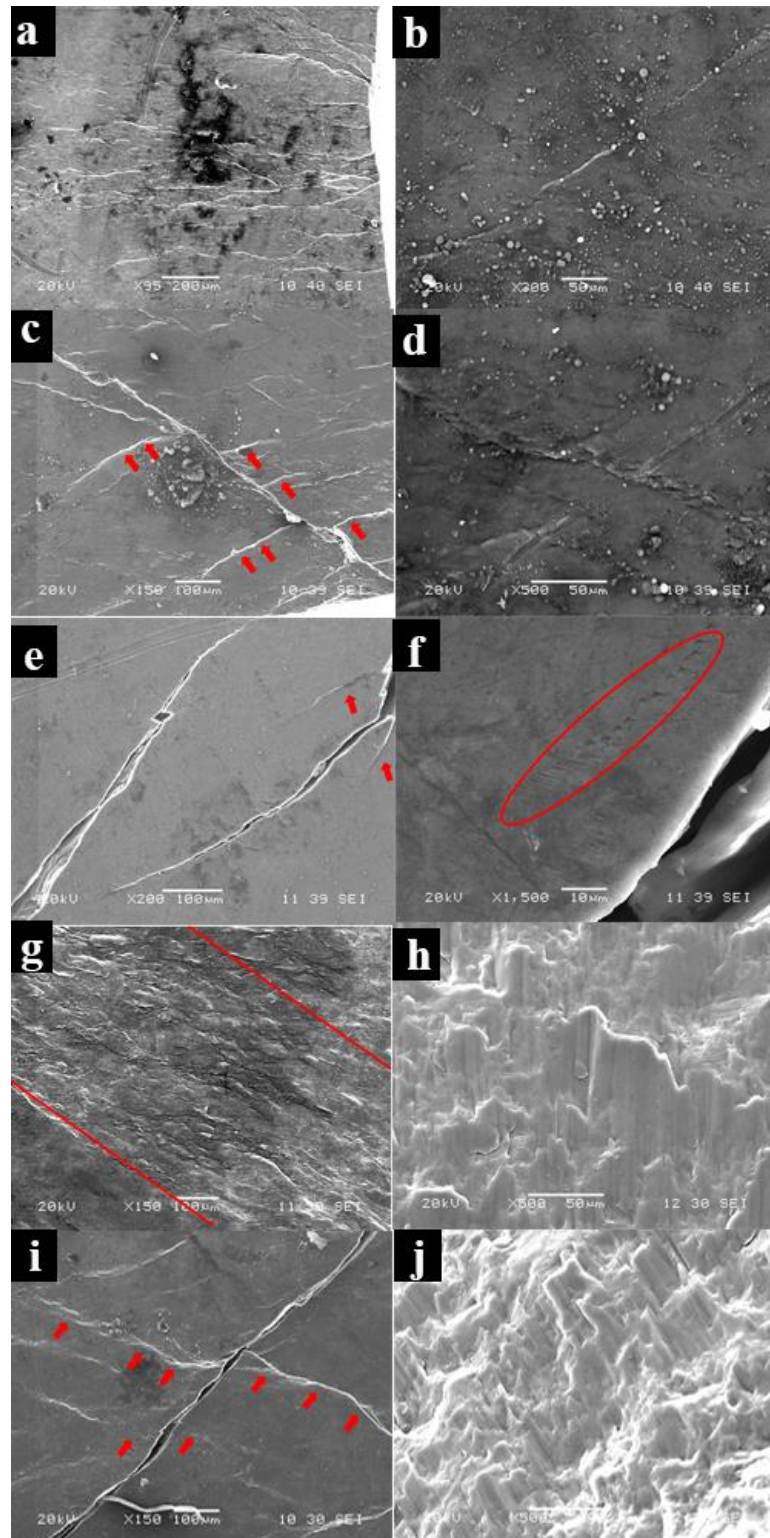


Figure 3.16: Fracture surface SEM macro (a, c, e, g, i) and micrographs (b, d, f, h, j) of AZ31B samples confined rolled at 150°C, 175°C, 200°C, 250°C, 300°C respectively after quasi-static compression along ND

Some evidence for shear localization was seen on both the sides of the shear band (marked by red arrows) suggesting a strain gradient across the fracture line with maximum strain towards the center. Samples rolled at 150°C and 250°C didn't show branching of the main crack however, they also failed through shear only.

The fracture surface micro-morphology of samples rolled at 150°C and 175°C was not studied since the sample didn't break during the operation. The sample failed through intermittent cracking and the crack was not connected as seen in fig. 3.16 (b) and (d). Samples rolled at 200°C showed micro-cracks parallel to the main crack. Samples rolled at temperature range of 200°C-300°C exhibited ductile fracture as shown in the form of elongated dimples in the fracture surface (fig. 3.16(c-d)).

3.5 Chapter summary

By far, based on the microstructural and mechanical property correlation, AZ31B samples confined rolled at lower temperatures (<200°C) responded positively with respect to the refinement of microstructure and improved mechanical properties in terms of higher compressive strength and slightly larger strain to failure especially in the case of samples rolled at 175°C. But a complete randomization of texture was not observed in any of these alloys. With dynamic recrystallization almost near completion, the samples will be expected to be isotropic. The recrystallized grains did not possess a random texture however, there was a slight shift in texture towards the RD probably because of confinement and thickness accommodation along the RD rather than TD. AZ31B rolled at a temperature range of 150°C -200°C showed better properties in terms of both compressive strength and strain to failure. The

work hardening rate was also slightly higher in this range due to completion of recrystallization and refinement of microstructure. However, they were not strain rate sensitive. Fracture surface morphology showed that the sample failed due to shear and exhibited features for ductile failure.

CHAPTER 4: Mg-6%Al

In this chapter, the research work on Mg-6%Al will be discussed with respect to the effect of addition of Al as an alloying element on the microstructure and mechanical behavior of confined rolled alloys. In the previous chapter, effect of addition of 3% Al to Mg was discussed. However, this alloy will show some complexity in terms of precipitation but not as much as expected from Mg-9%Al (which will be discussed in the next chapter). The extent to which deformation and dynamic recrystallization mechanisms will be affected due to dispersion of precipitates will be extensively studied in this chapter. Also, the effect of volume fraction, size, type and morphology of the precipitates in altering the recrystallization, deformation and ultimately the mechanical behavior of material will be analyzed elaborately. The expectation with this alloy is that it would be a perfect candidate for structural applications with the right amount of precipitation since they would aid in improving strength and simultaneously through precipitation hardening and acting as nucleation sites for fine dynamically recrystallized grains. The microstructure (optical/electron microscopy along with texture, deformation and dynamic recrystallization characterization through EBSD technique) and mechanical behavior (quasi-static and dynamic strain rate behavior under compression) of Mg-6% Al (A6) alloys will be studied in a similar manner as AZ31B. Additionally, the effect of precipitation (type and morphology) will be characterized with the help of TEM and correlated with their effect in affecting plastic deformation behavior of the material.

4.1 Optical Microstructure

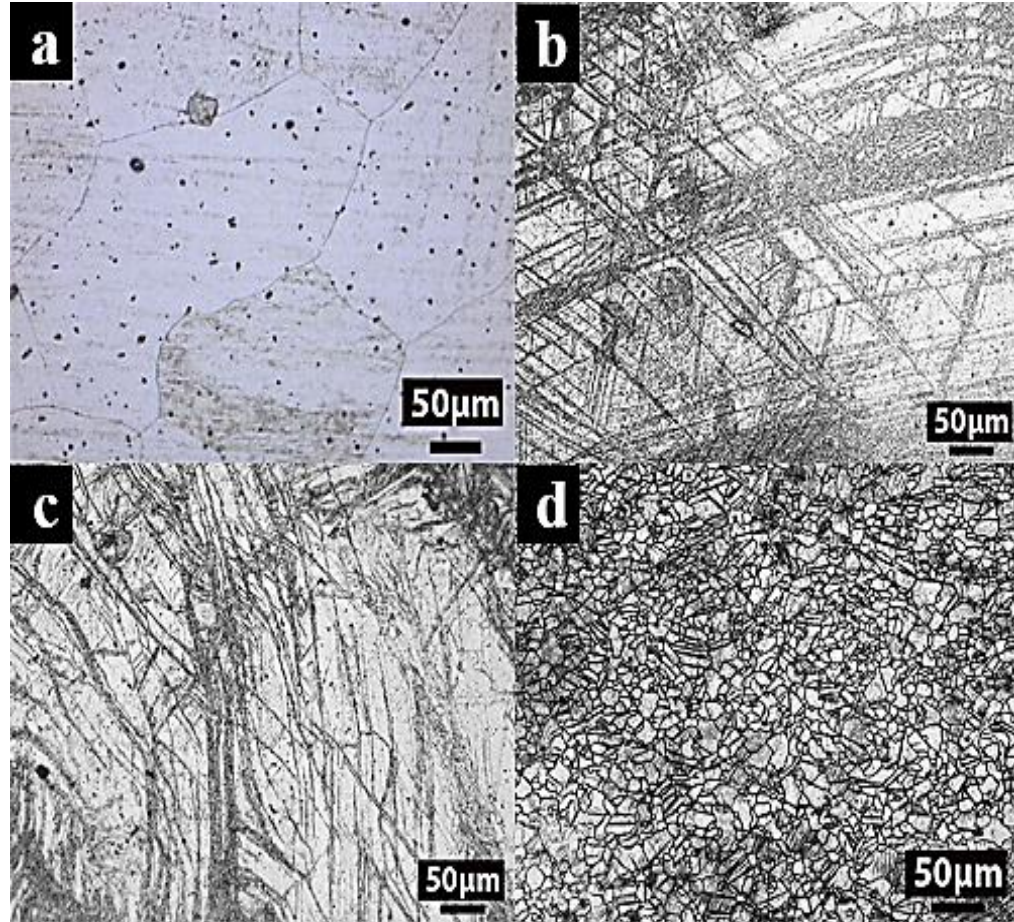


Figure 4.1 Optical micrographs of A6 alloys (a) before rolling and after confined rolling at (b) 200°C, (c) 250°C and (d) 300°C along normal direction (ND)

Fig. 4.1 shows the optical microstructure of A6 alloys confined rolled at 200°C (a), 250°C (b) and 300°C (c) respectively. The average grain size of the baseline alloy (before rolling) is found to be $\sim 150\mu\text{m}$. As rolling temperature increases, the extent of dynamic recrystallization increases with the microstructure being almost fully recrystallized at 300°C. The microstructure at 200°C and 250°C consists of recrystallized grains in either twins or shear bands. They had a necklace structure like that of AZ31B confined rolled at 150°C described in the previous chapter. Due to the resolution limit of optical microscope, the extremely fine features at these temperatures were not visualized properly. Hence, an advanced technique, EBSD

is required to study the finer details of the microstructure including grain size, extent of recrystallization, texture, effect of precipitation etc.

4.2 SEM-EBSD studies

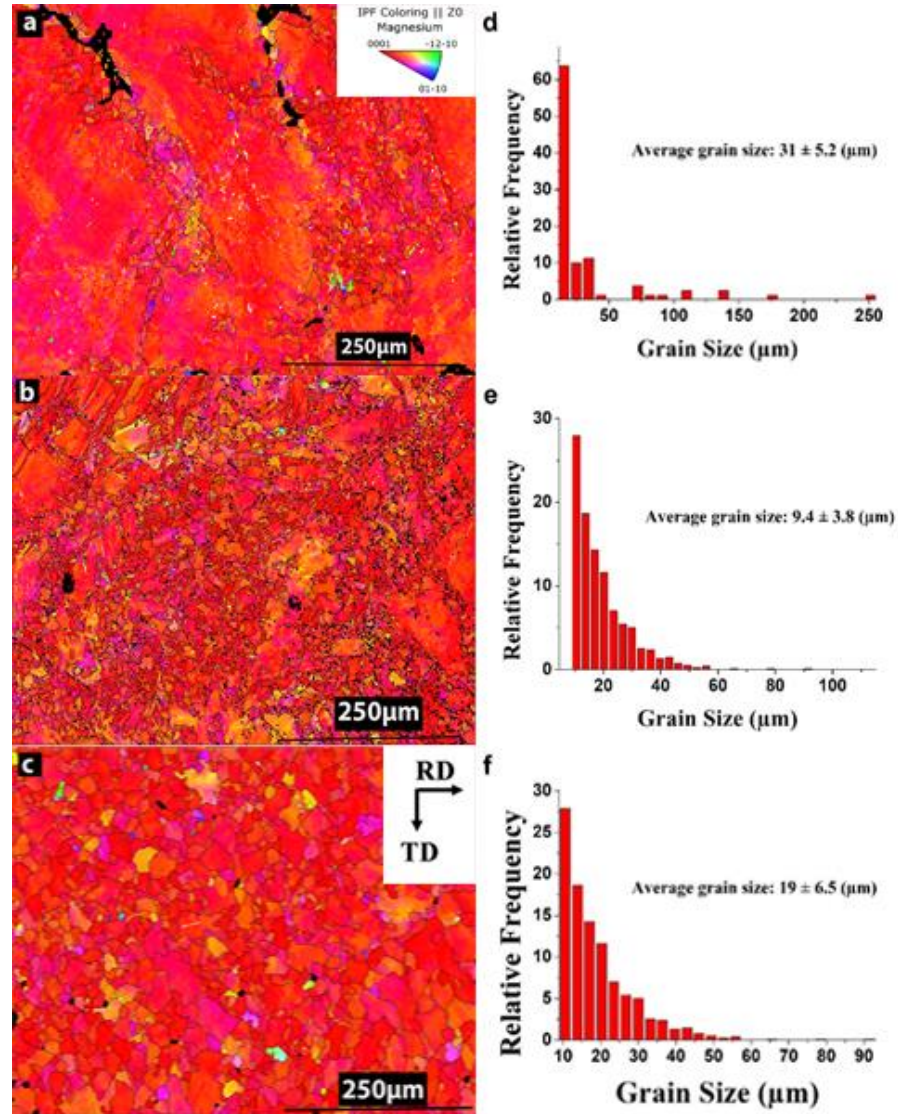


Figure 4.2 Inverse Pole Figure (IPF) map and the corresponding grain size measurements along ND plane of A6 alloys confined rolled at (a)&(d) 200°C, (b)&(e) 250°C and (c)&(f) 300°C respectively.

From the ND-IPF maps given in fig. 4.2, like AZ31B, it can be observed that the c-axes of most of the grains lie parallel to the normal direction thus confirming basal texture. Although compression and tensile twins are expected at lower

temperatures, the microstructure shows no to minimal twinning when observed through EBSD. At 200°C, there is no fragmentation observed in the bigger grains hence attributing to the highest average grain size among the three samples. This could be possible due to the precipitation kinetics being higher at lower temperature leading to a higher solute (Zener) drag hence retarding movement of the grain boundaries and in turn, recrystallization. Extensive fragmentation of grains and recrystallization is found in the samples rolled at 250°C giving rise to a smaller average grain size among the three samples (the average grain size is expected to be even smaller since some grains remain unindexed due to the limitations in the resolution limit of EBSD technique). This variation in grain size is due to the higher area fraction of coarse un-DRXed grains at lower temperatures and the subsequent increase in the area fraction of the recrystallized grains with further increase in rolling temperature. At 300°C, higher grain size was expected and observed due to the availability of thermal energy for grain coarsening.

4.2.1 Texture

Fig. 4.3 (a), (b), (c) and (d) represent the $\{0001\}$ and $\{10\bar{1}0\}$ pole figures of the as-rolled plates taken along the ND plane. The basal texture has been slightly shifted but still not randomized, and the c-axis is almost parallel to the normal direction at all the three rolling temperatures. It can be observed the strong texture had slight inclination towards transverse direction (TD) for samples rolled at 200°C and along ND for samples rolled at 250°C and 300°C. Confined rolling could be a reason for this slight shift in texture in the sample. The strong basal texture appearing at 200°C seemed to be consistent with the presence of a high fraction of

unrecrystallized deformed parent grains. With increase in temperature, volume of dynamically recrystallized (DRXed) grains increased consuming a major fraction of the deformed grains. The strong basal texture at 200°C evolves into a relatively weak texture at 250°C due to the dispersed orientation of the newly formed DRXed grains which was the main source for the weakening of the deformation texture like other severe plastic deformation methods such as ECAP[172] and DSR [156].

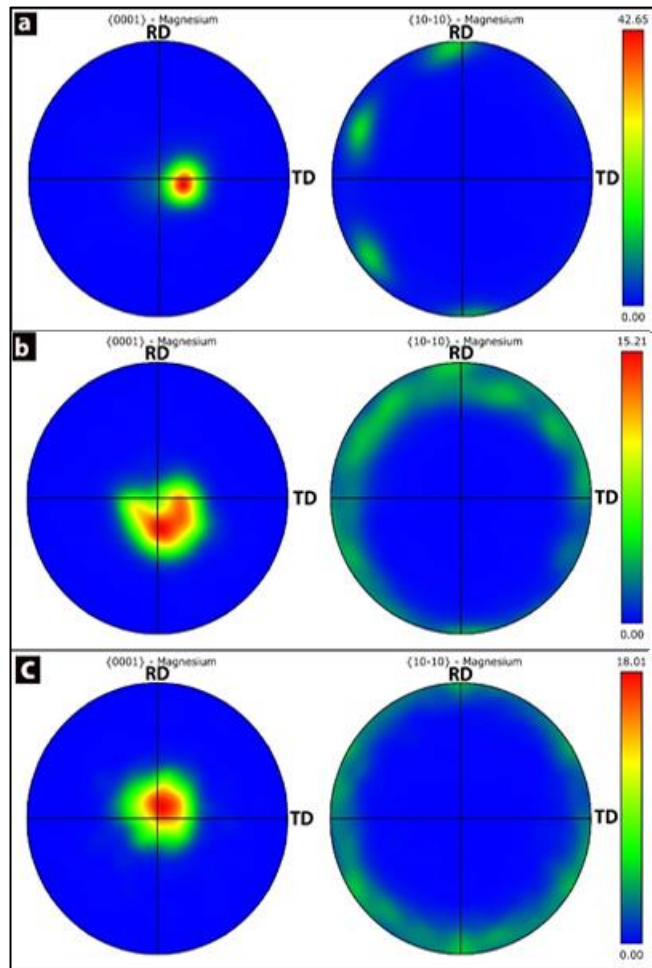


Figure 4.3 (a) –(c) Texture intensity along the ND of $\{0001\}$ and $\{10\bar{1}0\}$ planes of A6 alloys confined rolled at (a) 200°C, (b) 250°C and (c) 300°C

A similar drop in $\{0001\}$ textural intensity (indicated qualitatively by the multiple intensity of random orientation number (MRD) above the color bar next to the pole

figures) was also observed in the case of confined rolled AZ31B samples (previous chapter) between rolling temperatures of 150°C and 200°C. As temperature increases, the texture intensity begins to increase at 300°C. This is due to the easy dislocation movement facilitated by the activation of non-basal slip systems thereby promoting rotation of the grains parallel to the direction of deformation [156].

4.2.2 Grain boundary character distribution (GBCD):

Fig. 4.4 (a) shows that low angle grain boundary (LAGB fraction- grain boundary angle $<15^\circ$) for samples rolled at 200°C and 250°C was similar and the highest in comparison to samples rolled at 300°C. The boundary fraction of grain boundaries with angle between 2-5° progressively increased with increase in rolling temperature indicating the occurrence (ultrafine necklace structure) and near completion of DRX at 200°C and 250°C respectively. This may be due to precipitates facilitating dynamic recrystallization by acting as nucleation sites and not facilitating grain growth by securing grain boundaries through Zener pinning effect. Also, the increase of HAGBs could correspond to grain coarsening at higher temperatures due to availability of thermal energy to overcome the particle pinning effect.

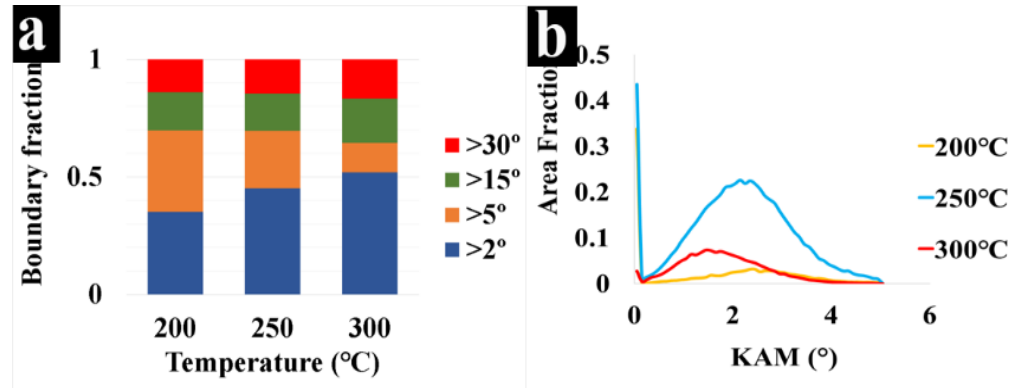


Figure 4.4 (a) Grain boundary distribution and (b) Kernel average misorientation distribution of A6 samples rolled at 200°C, 250°C and 300°C along ND

Kernel average misorientation (KAM) being an important indicator of geometrically necessary dislocation density, associated stored energy and strain distribution on individual measurement points was also studied for these alloys. It can be clearly seen that for samples rolled at 250°C, the KAM distribution was broader with higher average values in comparison to samples rolled at other temperatures indicating heterogeneity in dislocation arrangement, higher strain and dislocation density. At 300°C, the curve showed less broadening and inclined towards smaller average values due to lesser change in misorientation because of dynamic recovery (DRV). KAM values for samples rolled at 200°C and 250°C indicated that the samples were more strained in comparison to the samples rolled at 300°C. As the temperature of deformation reduced, strain accumulated in the material increased.

4.2.3 Average misorientation

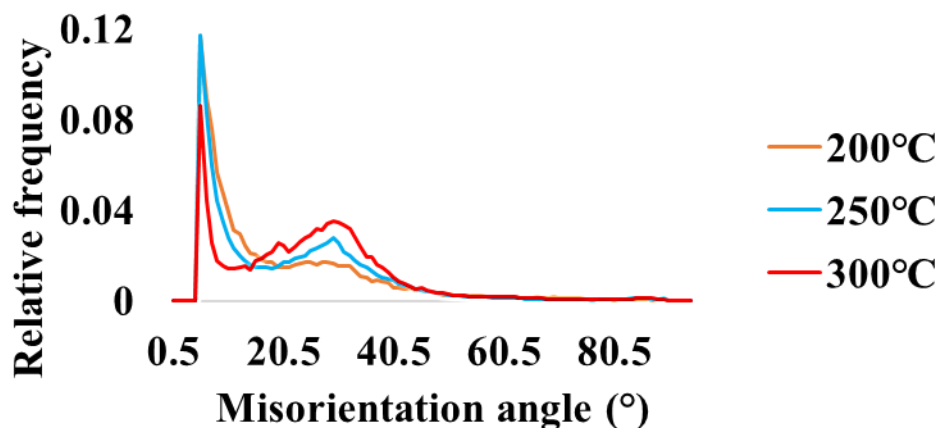


Figure 4.5 Misorientation angle distribution showing progressive increase of $30 \pm 5^\circ$ boundaries with increase in rolling temperature

The misorientation angle distributions of confined rolled samples were compared in fig. 4.5. The diffused population ranging from 0.5° to 180° with minor peaks at $\sim 30 \pm 5^\circ$ was observed in all the cases. Surprisingly, no significant peaks were observed at $\sim 90 \pm 5^\circ$ misorientation angle partially indicating that twinning is negligible in the rolled alloys which is entirely contrasting to the results obtained from AZ31B rolled at lower temperatures. Twinning becomes extremely difficult with fine-grain alloys containing precipitates [173]. Hence, an additional dislocation mechanism should be in place of twinning for such fine-grained alloys. The 30° [0001] grain boundaries which are common in Mg alloys after thermo-mechanical processing are mostly attributed to the formation of coincident site lattice (CSL) boundaries close to $\Sigma 13a$ boundaries [159, 161]. They are an indication of DRX occurring in materials. As discussed by Liu et.al [159], these grain boundaries correspond to an energy minimum and were highly mobile due to easy glide of Shockley partials along the {0001} plane [163, 164]. This may also be due to the

reason that most of the grains inside twins might have recrystallized at 200°C and could be resolved better than optical microscopy through the SEM- EBSD technique.

4.3 Deformation mechanism

In this section, an elaborate discussion on the dynamic recrystallization mechanisms, suppression of twinning, different strengthening mechanisms etc. will be done on A6 alloys. Since precipitation in this system is more in comparison to AZ31B alloys, it is imperative to understand their effect on recrystallization kinetics, invoking non-basal slip systems etc.

4.3.1 Grain orientation spread (GOS):

In the case of a distorted grain, due to the accumulation of dislocations and subsequent development of misorientation within the grains, this average misorientation i.e., GOS would be a higher value. On the other hand, a completely annealed material or a recrystallized microstructure might have a lower GOS value due to dislocation free grains due to annihilation and rearrangement of dislocations and due to the formation of defect-free and strain-free grains respectively. In the case of A6, an approximation of GOS value $<2^\circ$ was chosen to differentiate between recrystallized grains to the deformed parent grains in contrast to the GOS value $<5^\circ$ chosen for AZ31B alloys. This was done after careful measurement of GOS values of small equi-axed grains formed around the vicinity of larger deformed grains. Primary reason for this conservative criterion is due to recrystallized grain size changing drastically to coarse grain sizes if GOS criterion was increased for A6 alloys.

The images of the partitioned recrystallized grains based on the above said criterion for various rolling temperatures are given by fig. 4.6. From the microstructures, it can be clearly observed that the volume fraction of recrystallized grains increased as the rolling temperature increased up to 250°C and then decreased as temperature increased further. Also, the average size of recrystallized grains was the smallest at the rolling temperature of 250°C and increased as the temperature increased.

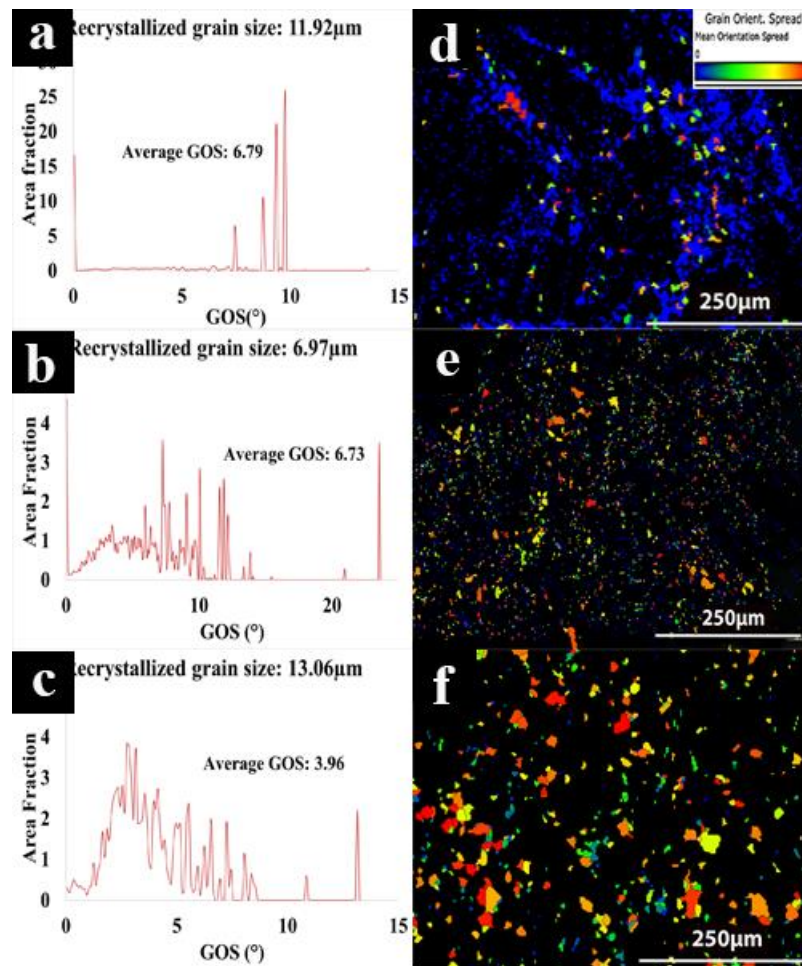


Figure 4.6 (a) – (c) GOS map and (d) – (f) corresponding recrystallized area along ND partitioned using GOS $< 2^\circ$ criterion of samples rolled at 200°C, 250°C and 300°C respectively

A viable reason could be that at low temperatures, critical strain for DRX would have been reached at many sites whereas at higher temperatures, due to the enhanced relaxation process, the critical strain would not have been available at a lot of sites in comparison to lower rolling temperatures leading to a smaller number of recrystallized grains [174]. The lower GOS and higher recrystallized grain size value of samples rolled at 300°C indicated completion of recrystallization and grain growth respectively.

4.3.2 Schmid factor

Fig. 4.7 shows the variation of Schmid factor of predominant slip systems with rolling temperatures. Activity of basal slip appears to be lower at all the temperatures in comparison to the activity of non-basal slip system, i.e., pyramidal II system being the highest for all the different rolling temperatures. All other non-basal slip systems remained the same through the variation of rolling temperatures.

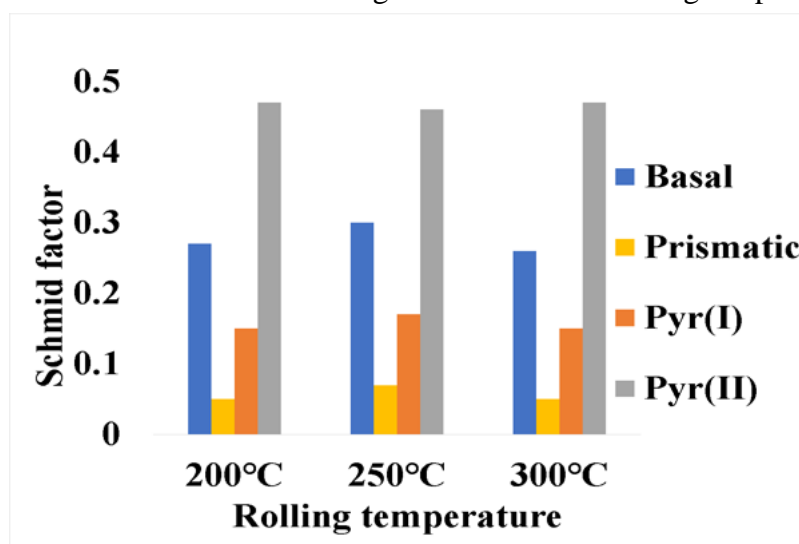
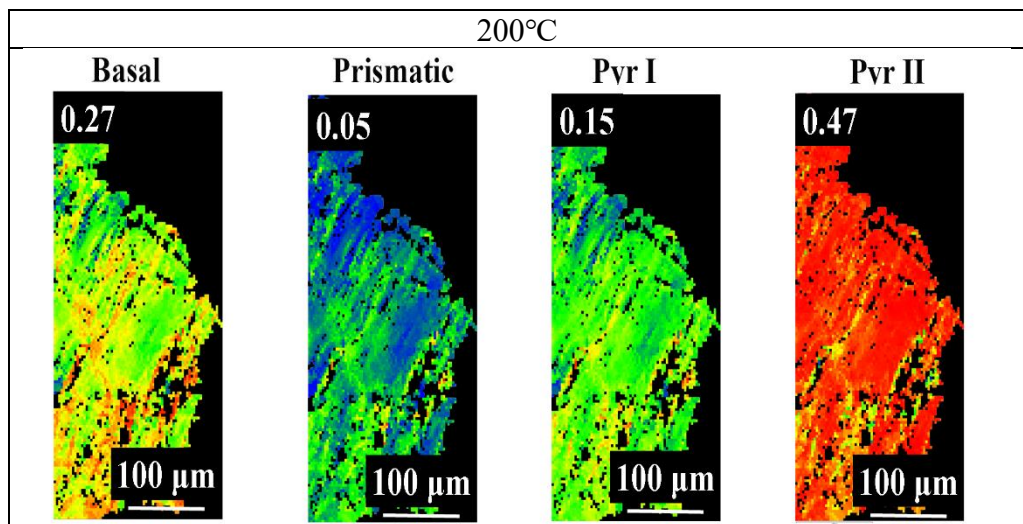


Figure 4.7 Variation of Schmid factor with rolling temperature along ND

From fig. 4.8 which shows the activity of various slip systems in a single grain in the microstructure, it was evident that non-basal slips (mainly $\langle c+a \rangle$ pyramidal II slip system) were active at all the rolling temperatures which was proved by higher

Schmid factor of 0.46-0.47. This is possibly due to the deformation assisted DRX and the effect of compatibility stresses. In large-grained Mg alloys, to satisfy the von-Mises criterion, twinning acts as an auxiliary deformation mechanism to basal slip. In juxtaposition, fine grained A6 alloy do not show extensive twinning at any stage of deformation as twinning becomes increasingly difficult with decreasing grain size and higher volume fraction of precipitates [173].

Strain incompatibility is caused in the grain boundaries when only two independent slip systems are available instead of the necessary five. Additional stresses arise to maintain strain compatibility in the grain boundaries since the boundaries are strong enough for Mg alloys. In this process, non-basal dislocations as well as twins get activated. This phenomenon is well documented in bi-crystal experiments [175-177]. In equi-channel angular extruded (ECAE) AZ31B, Kobayashi et al. and Koike et al., reported that non-basal dislocations were generated several microns from grain boundaries. In fine grained alloys, the compatibility stress sweeps the entire grain volume.



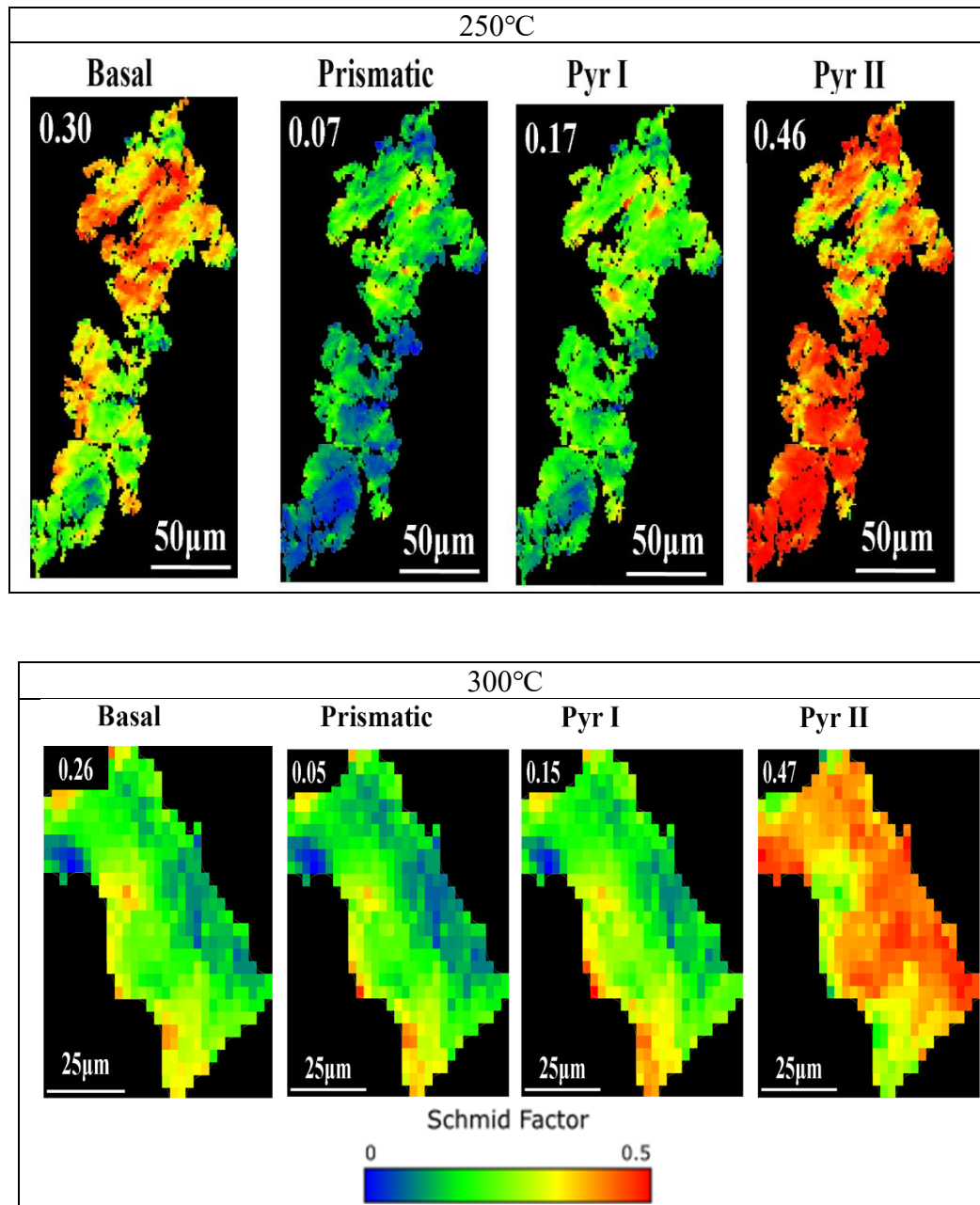


Figure 4.8 Basal slip Schmid factor maps along ND for samples rolled at 200°C, 250°C and 300°C respectively

On one hand, this compatibility stress at grain boundaries restricts the basal slip and on the other hand, enables activity of non-basal slip [174-180]. The distance of influence of compatibility stress from grain boundary has been analyzed to be $\sim 10\mu\text{m}$ [179]. In the case of A6 alloy, the grain size for samples rolled at 250°C and

300°C ranging from 9 μm -19 μm was sufficient to activate both basal and non-basal dislocation slip systems. This compatibility stress induced by higher volume fraction of precipitates was attributed as the main reason for the activation of pyramidal II slip systems in these confined rolled alloys.

4.3.3 DRX mechanism

Mechanisms of plastic deformation and DRX varied with different temperature regions as shown in fig. 4.9. In the low rolling temperature regime (200-250°C), continuous DRX (CDRX) was found to operate whereas at high temperatures (such as 300°C), it was unclear which mechanism was operating, while choosing the grain for studying its interior misorientation, it could either be DDRX or it could simply be a recrystallized grain since the misorientation inside is the lowest in this case as well. The model proposed by Galiyev et al. for ZK60 alloy was found to be accurate with the A6 alloy system [99]. According to them, the following are the mechanisms:

1. At low temperatures, basal dislocations with a Burgers vector accumulate near twin boundaries. Therefore, the internal stresses created due to the remaining large elastic distortion exceeds the local CRSS required for non-basal slip. This rearrangement of dislocations results in the formation of high angle grain boundaries. Along with that, $\langle c+a \rangle$ dislocations are also required for the complete formation of 3D recrystallization nuclei [99].
2. At intermediate temperatures, cross-slip of a dislocations on non-basal planes which is activated predominantly near grain boundaries due to higher stress concentration controls plastic deformation. This leads to a transition of screw

dislocation to edge dislocation (which can readily climb since it lies in a non-basal plane) by Friedel-Escaig mechanism. A network of low angle boundaries gets generated at the vicinity of the grain boundaries by dislocation rearrangements through the above-mentioned mechanisms of cross-slip and climb. Cross-slip of a dislocations by Friedel-Escaig mechanism controls both plastic flow and DRX nucleation. Recrystallized grain size is at the lowest in this temperature range since the process is not diffusion controlled.

3. At high temperatures, dislocation climb becomes the controlling process since the activation energy of plastic flow approaches the activation energy of volume self-diffusion. Bulging of grain boundaries caused by strain localization at slip lines leads to DRX nucleation. Fast dislocation climb leads to the formation of low angle grain boundaries which in-turn trap moving dislocations and converts them into high angle grain boundaries. In this case, dislocation climb controls both plastic deformation and nucleation of DRX [99].

This behavior of A6 alloys was slightly varied with reference to AZ31B alloys which exhibited only discontinuous dynamic recrystallization (DDRX) at all rolling temperatures. This change in A6 alloys may perhaps have been due to the invocation of non-basal slip systems combined with the refinement of grain size or the effect of precipitate in pinning the grain boundaries hence reducing the driving force for DDRX which will be studied in detail in the upcoming chapter.

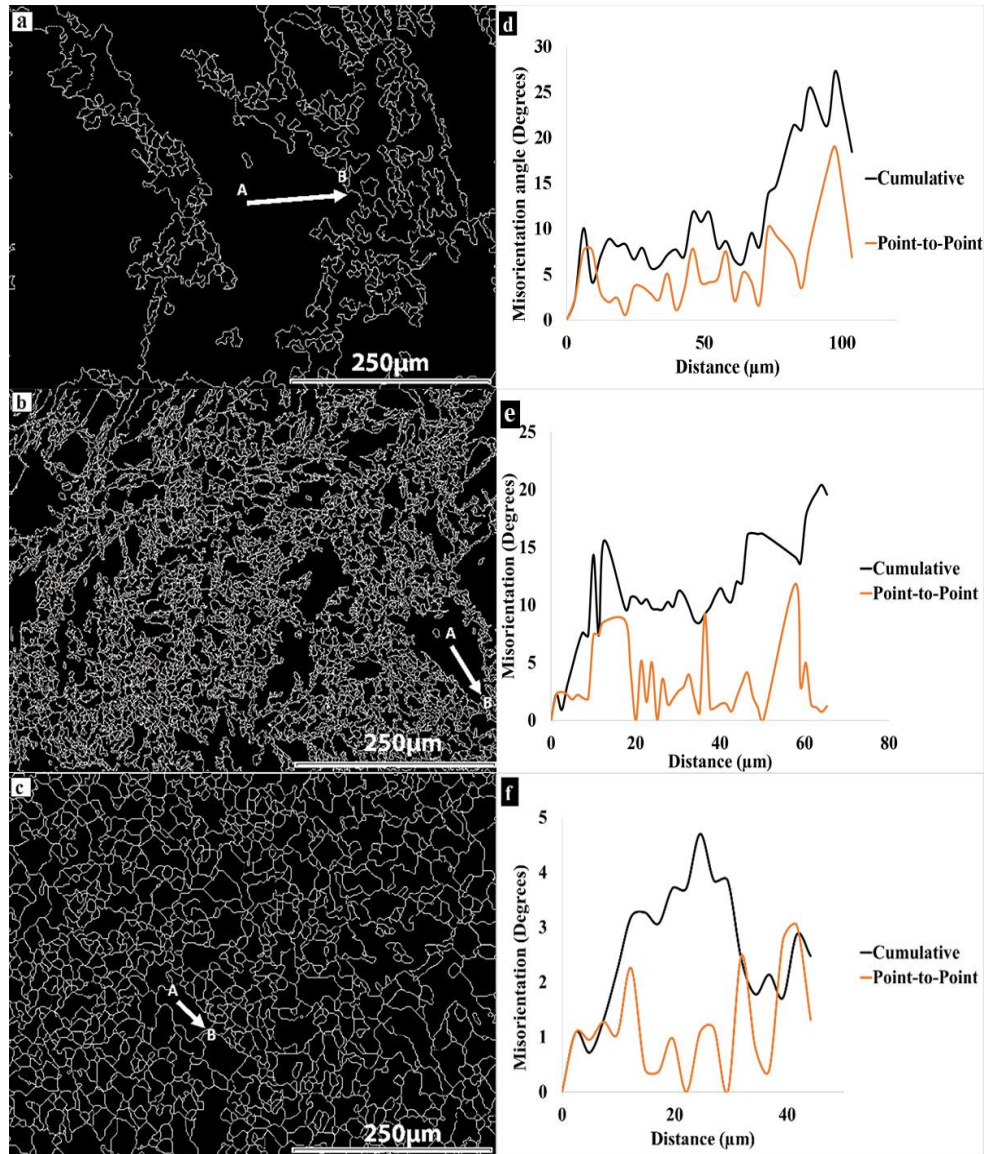


Figure 4.9 Grain boundary map along ND (a-c) and corresponding line profiles of misorientation indicated by black arrow A-B (d-f) for samples rolled at 200°C, 250°C and 300°C respectively.

4.4 Effect of Precipitation

4.4.1 Continuous and discontinuous precipitation

In the case of Mg-Al systems, discontinuous precipitation (DP) is a duplex growth with alternative layers of secondary phase and near-equilibrium matrix phase at high angle grain boundaries. Precipitates which form in all the remaining regions of the super-saturated Mg-Al matrix are called continuous precipitates (CPs). Both

signify a solid-solid phase transformation where a super-saturated solid solution, α_0 , decomposes into a new solute-rich precipitate, γ , and a comparatively less saturated, near equilibrium phase, α , with a crystal structure similar to the parent phase α_0 . The mechanism behind CP is nucleation and growth of the γ phase inside the α_0 grains, whereas, for DP, the alternating layers of α and γ phases form behind a moving grain boundary. The volume fraction of DP depends on various factors such as the reaction front velocity, temperature, average composition of the solute depleted α -lamellae, grain boundary condition, etc. [181-183]. In contrast, the phase transformation during CP is a sequential process of nucleation, growth, and impingement [114, 184, 185]. In both the cases, the limiting factor would be a reduction in the driving force for propagation and impingement. The amount of CP depends on crystal defects within the matrix acting as heterogenous sites for nucleation. Apart from grain boundaries, other nucleation sites include dislocations, vacancies, stacking faults, etc. Especially, important are vacancies that promote volume diffusion. Vacancy diffusion can be prominent in this alloy due to the comparable size of Al and Mg atoms. Discontinuous and continuous precipitation are favored when grain boundary and volume diffusion is favored, respectively. In the case of this alloy system, confined rolling and subsequent quenching would have increased the concentration of (non-equilibrium) vacancies. The volume fraction of continuous precipitates increased with increasing temperature. At higher temperature, diffusion becomes faster, resulting in larger volume and more massive precipitates.

Precipitation in A6 alloys differs with location namely, continuous precipitation which occurs within grain interiors and discontinuous precipitates which occur along grain boundaries. Both types of precipitates could be observed to coexist in the matrix, i.e., continuous precipitates inside the grains and discontinuous precipitates along the grain boundaries. At lower and higher rolling temperatures of 200°C, continuous precipitation appeared to be predominant although the mechanism of precipitation is different. At 200°C, continuous precipitates were in nucleation and growth regime and eliminated most of the super-saturation hence preventing discontinuous precipitates from nucleating (fig.4.10).

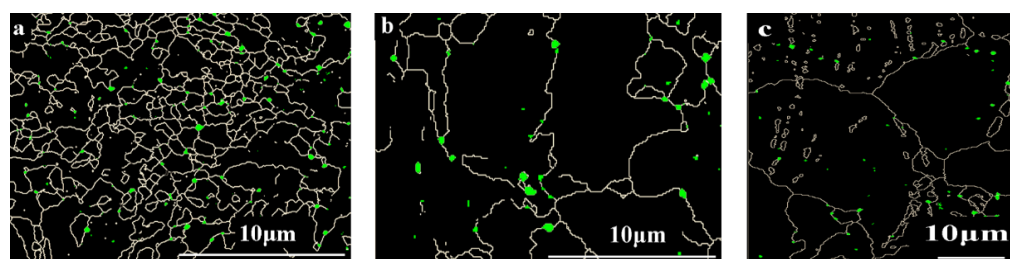


Figure 4.10 EBSD maps along ND showing continuous and discontinuous precipitates in samples rolled at (a)200°C (b)250°C (c)300°C. Green color represents Mg₁₇Al₁₂ precipitates.

At the intermediate temperature of 250°C, both continuous and discontinuous precipitation co-existed. However, discontinuous precipitation dominated as seen in figure 4.10 (b). These continuous precipitates might act as nucleating agents for recrystallization when discontinuous precipitates pin the grain boundaries in turn arresting grain growth causing a refined microstructure.

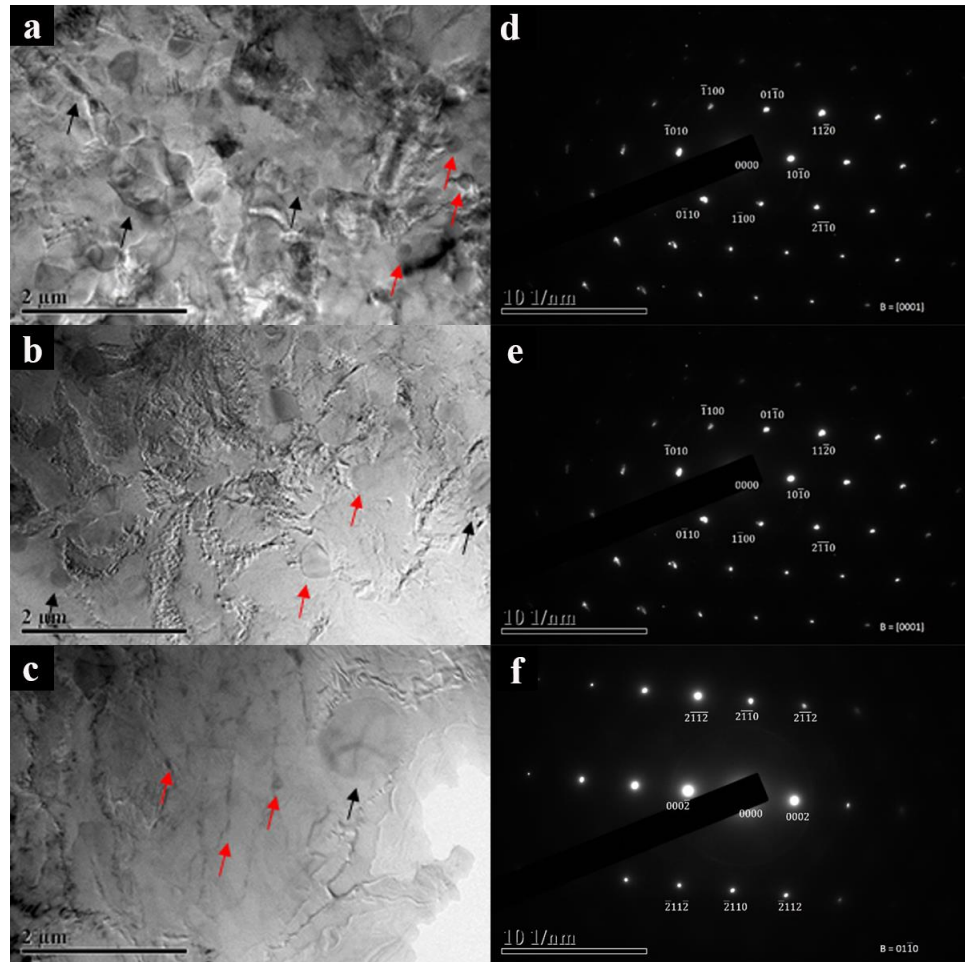


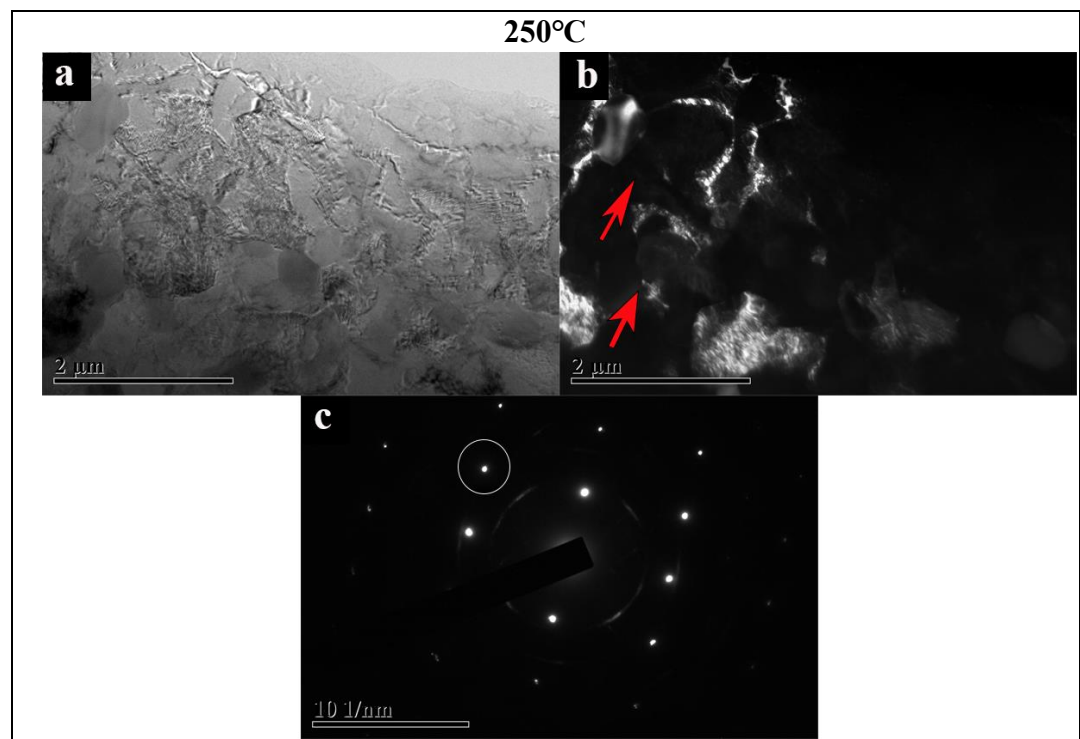
Figure 4.11 TEM micrographs showing continuous and discontinuous precipitates in samples rolled at (a), (d) 200°C (b), (e) 250°C (c), (f) 300°C (continuous and discontinuous precipitates shown in black and red arrows respectively).

The macroscopic kinetics of discontinuous precipitation depends on nucleation rate per grain and its average nucleation time is approximately one order of magnitude larger than the propagation time making initiation much more difficult if continuous precipitation occurs. At 300°C, volume diffusion in front of a moving grain boundary during the growth of a discontinuous precipitate colony equalized solute content in both sides of the boundary hence reducing the chemical driving energy for propagation of discontinuous precipitation [186]. However, TEM micrographs show micrographs of both coarse discontinuous and fine nano-sized continuous precipitates. Hence, it would be interesting to know the balancing act of Zener

pinning and particle stimulated nucleation in forming the final microstructure of the material thereby affecting its mechanical properties.

4.4.2 Particle stimulated nucleation and Zener pinning

Numerous studies have indicated that particle stimulated nucleation (PSN) has a profound effect on DRX by formation of deformation zones around the particle which would hinder dislocation movement hence forming LAGBs. Second phase particles have a significant PSN effect on DRX behavior by accelerating DRX nucleation.



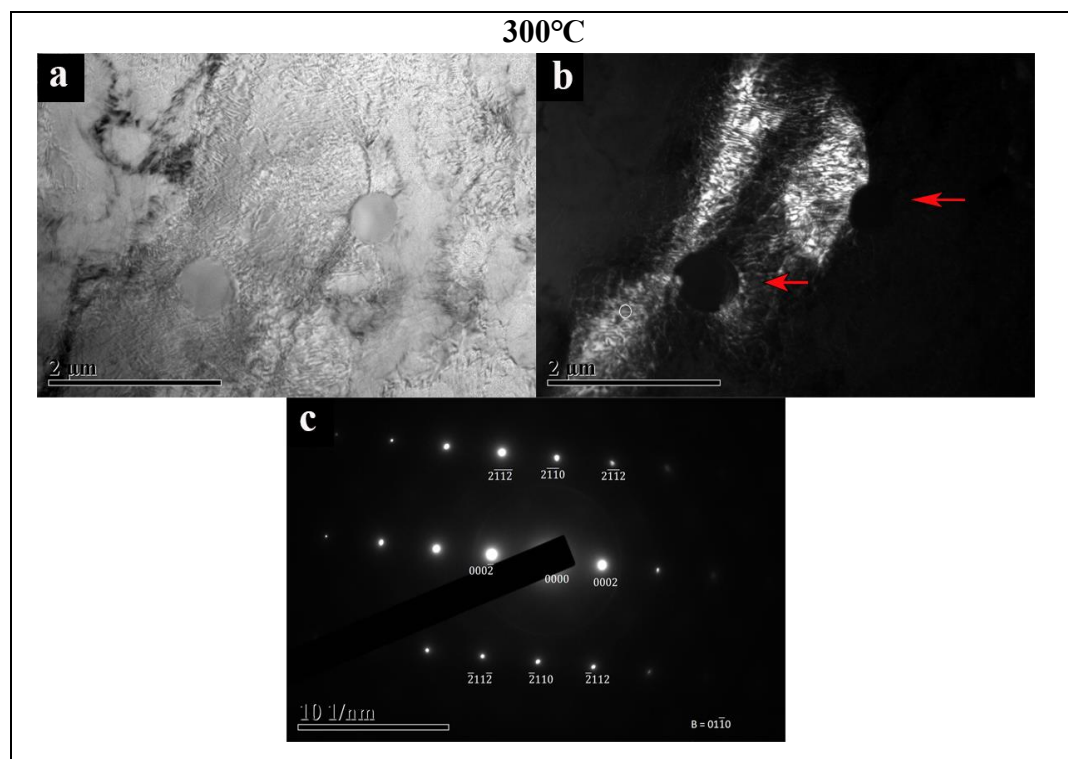


Figure 4.12 Particle stimulated nucleation observed in A6 samples rolled in bright field (a), dark field (b) and selected area diffraction (SAD) pattern (c) at 250°C and 300°C respectively

Humphreys concluded that a) recrystallization originates at the pre-existing sub-grain within the deformation zone but not necessarily at the particle surface; (b) nucleation occurs by sub-boundary migration; (c) a grain may stop growing when the deformation zone is consumed. A common feature of PSN is that the recrystallized grains do not grow large and eventually get surrounded by other recrystallized grains [181, 187, 188]. Based on TEM observation, only samples rolled at 250°C and 300°C exhibited evidence of PSN (fig. 4.12) and looking at the fine recrystallized grain size of $\sim 6.97\mu\text{m}$ at 250°C for instance, it can be safely concluded that PSN played a major part in recrystallization along with deformation.

When coarse particles act as nucleation sites for recrystallization, nano-sized fine particles present in the microstructure exhibit a pinning effect on grain

boundary migration thus, mitigating their growth. This effect is described as pinning the rearrangement of dislocations and grain boundary migration [181, 187, 188]. For grain boundary migration, the pinning effect by precipitates is given by:

$$V = M_0 \exp\left(\frac{-Q}{RT}\right) (P_D^{Rex} - P_Z - P_C) \quad (4.1)$$

$$P_D^{Rex} = 0.5\rho Gb^2 \quad (4.2)$$

$$P_Z = \frac{3F_V\gamma}{2r} \quad (4.3)$$

$$P_C = \frac{\alpha\gamma}{R} \quad (4.4)$$

In the above equations, P_D^{Rex} is the driving force M_0 is grain boundary mobility, Q is apparent activation energy, P_Z is Zener pinning pressure and P_C is boundary curvature pressure, ρ is dislocation density, G is shear modulus, b is Burger's vector, γ is grain boundary energy, r is average radius of precipitates and $\frac{1}{R}$ is the mean radius of grain boundary curvature. Based on TEM observations of precipitation, it can be assumed that the outstanding grain refinement of samples rolled at 250°C was indeed due to the finer grain sized precipitates [181, 182, 188-192].

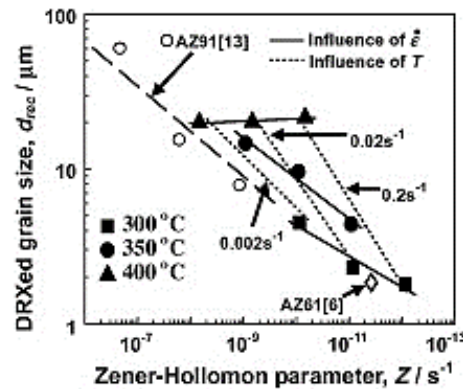


Figure 4.13 Variation of DRXed grain size with Zener-Hollomon parameter [188]

Also, researchers have reported that DRXed grain sizes of Mg alloys are governed by the Zener-Hollomon parameter, $Z = \dot{\epsilon} \exp(Q/RT)$, where $\dot{\epsilon}$ is the strain rate and T is the temperature as shown in fig. 4.13 [188]. When the compression temperature is fixed, the DRXed grain size decreases with increasing strain rate whereas at a given strain rate, the DRXed grain size decreases as temperature decreases. The slope of grain size exponent, m is less for fixed strain rate than for the fixed temperature proving that influence of compression temperature on DRXed grain size is stronger than that of the strain rate since it influences the size, volume fraction and morphology of the precipitates. This is precisely the same reason why the grain size of A6 initially at $\sim 150\mu\text{m}$ reduces to $\sim 9\text{-}30\mu\text{m}$ after confined rolling [185, 188, 190]. Also, some amount of shear stress could have developed along the ND plane due to restriction of movement along TD during confined rolling and could also have been another reason for this drastic grain refinement.

4.4.3 Precipitate morphology

Traditional heat treatment and severe plastic deformation techniques produce precipitates with high aspect ratios leading to poor strengthening. These long aspect ratio precipitates can act as a source of spall failure since they act as sources of void nucleation which accelerates failure during real-time applications. Attempts have been made to refine the size and alter the shape of the precipitates through deformation assisted precipitation and some researchers were successful in refining the microstructure [114, 117, 184].

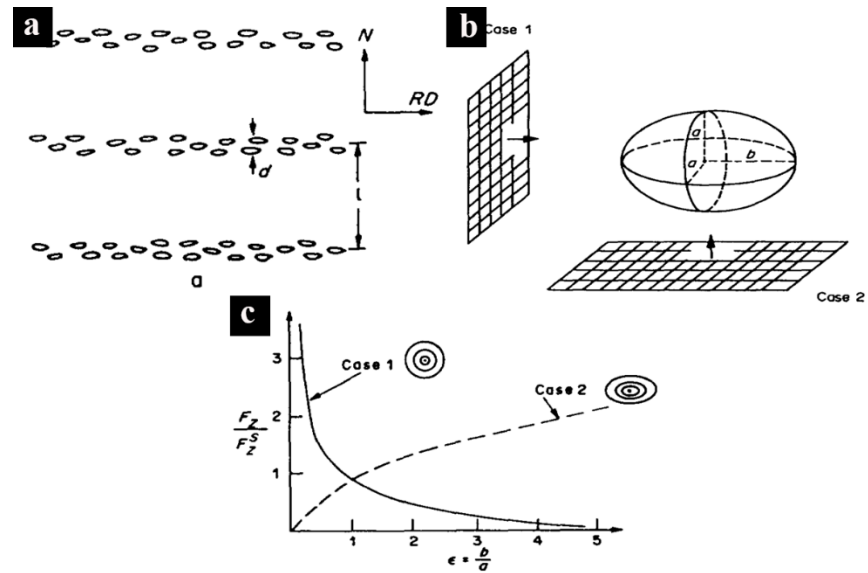


Figure 4.14 (a) Particle structure in metals, (b) Particles having an ellipsoidal shape with rotational symmetry around RD axis and (c) drag force as a function of particle aspect ratio based on geometry given in (a) [181, 182]

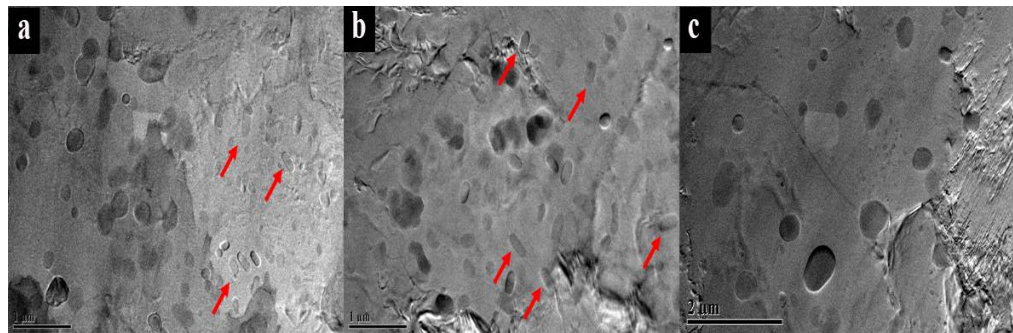


Figure 4.15 Precipitate morphologies of samples rolled at (a) 200°C, (b) 250°C and (c) 300°C

Nes et al. [182] studied the effect of spatial distribution of particles and shape effects on the mobile boundary of the recrystallized grains during annealing of cold rolled Al-Mn alloys. They demonstrated that the shape of the particles does matter. However, the pinning effect is slightly larger than spherical precipitates only when a particle with small aspect ratio meets the boundary with the short axis perpendicular to it or a particle with higher aspect ratio meets the boundary with long axis perpendicular to it. Shape of the precipitate is strongly dependent on

particle distribution parameter, $\delta = \frac{L}{d}$ and particle shape parameter, $\varepsilon = \frac{b}{a}$ represented by the eccentricity of the ellipsoidal particle as shown in fig. 4.14. In the case of A6, the drag force exerted by plate shaped particles was more in comparison to spherical precipitates as can be seen from fig. 4.15 and 4.16 [181, 182]. At pressure ratio around 0.1 and with particle distribution parameter of 5, even for spherical particles ($\varepsilon = 1$), strongly flattened recrystallized grains were observed. The effect of grain shape due to particle shape can be disregarded at lower pressure ratio ($q < 0.2$) since it is considerable only at higher pressure ratios ($q > 0.2$).

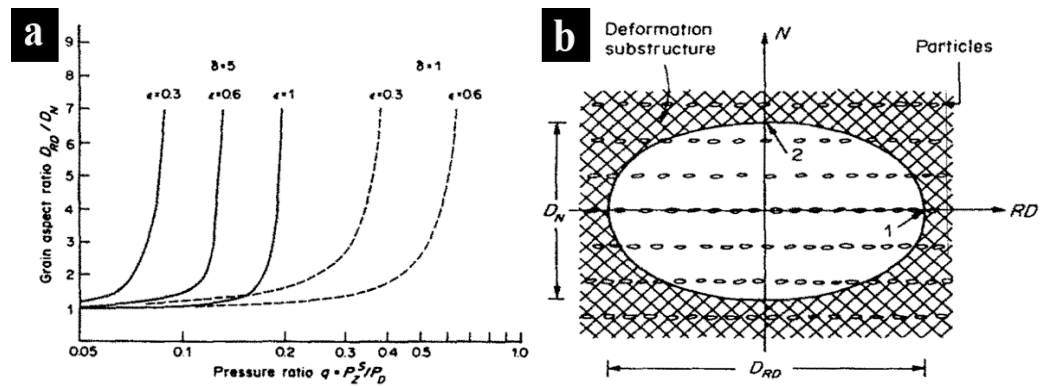


Figure 4.16 (a) Recrystallized grain aspect ratio as a function of pressure ratio, q , with δ and ε as variables and (b) short transverse-longitudinal section of a recrystallized grains [181, 182]

The volume fraction of ellipsoid samples was the highest for the samples rolled at 250°C (fig. 4.15). This was attributed as the reason for better mechanical properties due to the exceptional drag force exerted by the particles of the cross-section which will be described in the upcoming section. This drag force perhaps, kept grain growth under control and refined the microstructure effectively.

4.5 Mechanical properties under compression

4.5.1 Stress-strain behavior at different strain rates under compression

Quasi-static (strain rate $\sim 10^{-3} \text{ s}^{-1}$) and high strain rate ($1 \cdot 10^3 \text{ s}^{-1}$) experiments were performed in uniaxial compression using INSTRON model 5582 Universal Testing Machine and conventional Kolsky (Split Hopkinson Pressure Bar SHPB) respectively. As seen in fig. 4.17, at quasi-static conditions, strain hardening rate remained steep and almost constant at all temperatures. The compressive strength of the alloys rolled at different temperatures was almost doubled and ductility almost halved in comparison with baseline alloys. While there was no change in ductility, there was a decrease in compressive strength as rolling temperature increased. The sigmoidal shape of the curves indicated profuse twinning in this material. In contrast, at dynamic conditions, the same alloys exhibited higher strength and ductility as rolling temperature increased.

The material rolled at 250°C and 300°C exhibited strain rate hardening i.e., the compressive strength increases with increase in strain rate. Particle stimulated nucleation (PSN) observed in the alloys rolled at these temperatures might be a major factor for such exceptional behavior of this alloy. The observed flow stresses at dynamic strain rates were higher in comparison to quasi-static rates hence signifying that the alloys at those temperatures could be strain rate sensitive. Again, the balance between PSN and Zener pinning enabling refinement of the

microstructure could be a reason for the increased strain rate sensitivity (SRS) of this material in comparison to AZ31B alloys which showed zero to negative SRS.

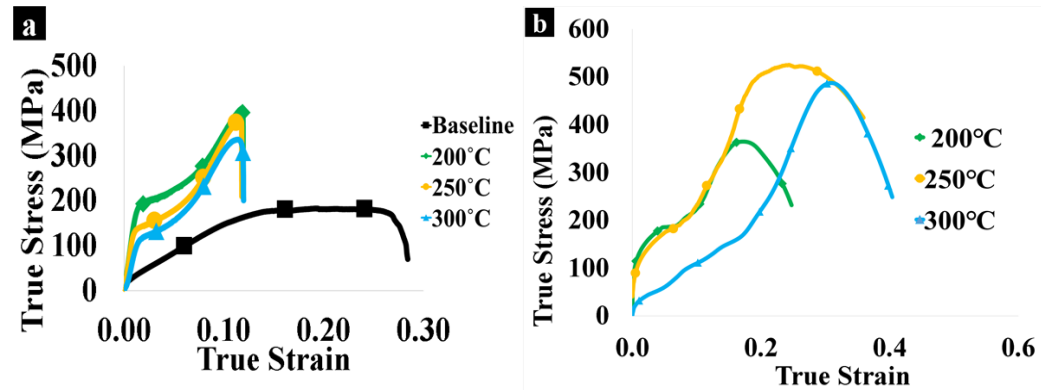


Figure 4.17: (a) Quasi-static and (b) dynamic compressive behavior of A6 alloy rolled at different temperatures along ND

The strain to fracture looks similar for both the current alloy and AZ31B at quasi-static strain rates however, at dynamic strain rates, A6 tends to be more malleable since the effect of precipitation in altering the deformation and recrystallization mechanisms plays a critical role although AZ31B had fine grains like A6 alloys.

4.5.2 Strain hardening rate and coefficient

Strain hardening capability of a material can be assessed by two factors: First is the strain hardening rate shown in figure 4.18 (a) at quasi-static strain rates. All the samples showed similar trend i.e., a linear decrease in the strain hardening rate (Stage III hardening) as true strain increased followed by Stage IV hardening commonly seen in slip assisted deformation [193]. A6 samples rolled at 200°C had the highest initial strain hardening rate but the lowest ductility when compressed at high strain rates. This could be attributed to higher volume fraction of precipitates and rod-shaped morphology of the precipitates which effectively impede dislocations than spherical precipitates [194]. Second factor is the strain hardening

exponent [194, 195], larger its magnitude, greater the strain hardening for a given amount of plastic strain. Figure 4.18 (b) represents the variation of strain hardening exponent with varying temperature for different strain rates showing a decreasing trend as strain rate increased.

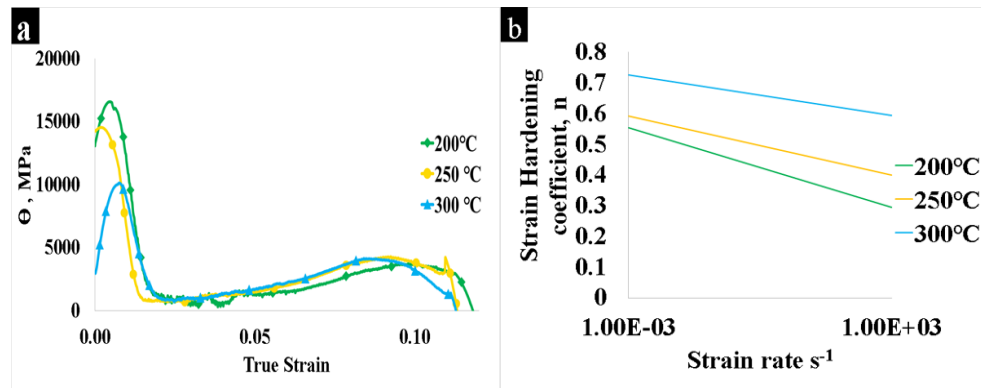


Figure 4.18: (a) strain hardening rate at quasi-static strain rate and (b) strain hardening coefficient of A6 alloys along ND

4.5.3 Strain rate sensitivity (SRS)

Higher values of SRS indicate better post uniform deformation and a gradual loss of load bearing capacity [193, 194]. Figure 4 shows SRS value increasing until 250°C and then decreases for samples rolled at 300°C. This may be due to the possible nucleation of twin boundaries at lower strains followed by their disappearance [196, 197] which can be slightly observed in figure 1(b). Although strain hardening rate of samples rolled at 200°C was the highest, higher volume fraction of the precipitates could have prevented the migration of twin boundaries hence making them less strain rate sensitive compared to 250°C which seems to be a temperature where both twin and slip assisted deformation occurs amicably hence having better strength and ductility simultaneously compared to samples rolled at other temperatures.

Although the values of SRS at 300°C might seem to be extremely low, it can be deceiving since the sample had a good strain hardening behavior as strain increased. The reason for the comparatively lower yielding in the material rolled at 300°C can be attributed to perhaps the bimodal distribution of precipitates (coarse discontinuous and fine continuous precipitates) and the extensive drag exhibited by the nano continuous precipitates associated with change of texture etc. [198].

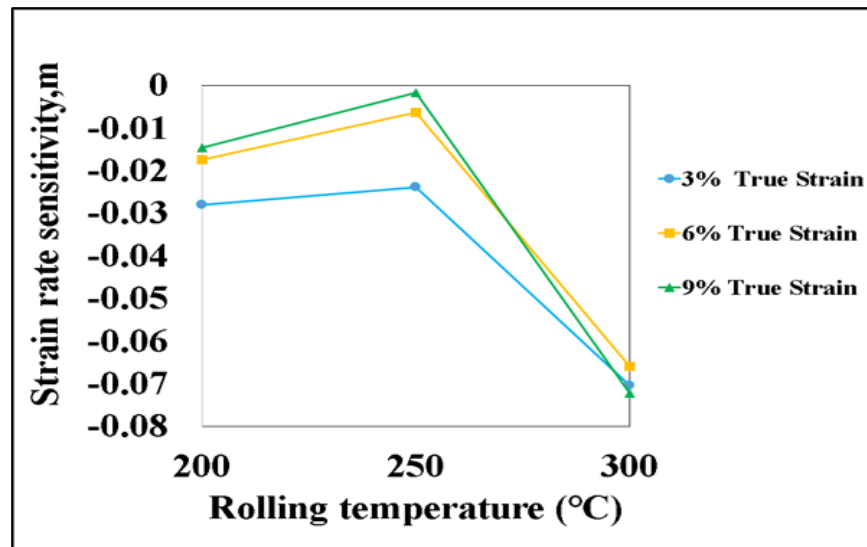


Figure 4.19: Strain rate sensitivity (SRS) of A6 alloys along ND

4.5.4 Fracture surface analysis under quasi-static compression:

Figure 4.20 (a, c, e) shows macroscopic fracture surfaces of A6 samples rolled at 200°C, 250°C and 300°C respectively after quasi-static compression along ND. All the dynamically tested samples were broken into tiny bits and hence, could not be recovered for failure analysis. The quasi-static compression testing failed samples were characterized by the presence of fracture lines oriented at 45° with respect to the loading direction. All the samples showed shear failure with evidence of localized shear flow on both sides of the shear band (marked by red arrows).

According to Wright et al. [199] this shear banding exhibits a canonical structure where the flow lines curve into one side of the band and curve away from the other side of the band as pointed by arrows in fig. 4.20 a, c, e. This suggests that a strain gradient occurs across the fracture line with the maximum located at the mid-point.

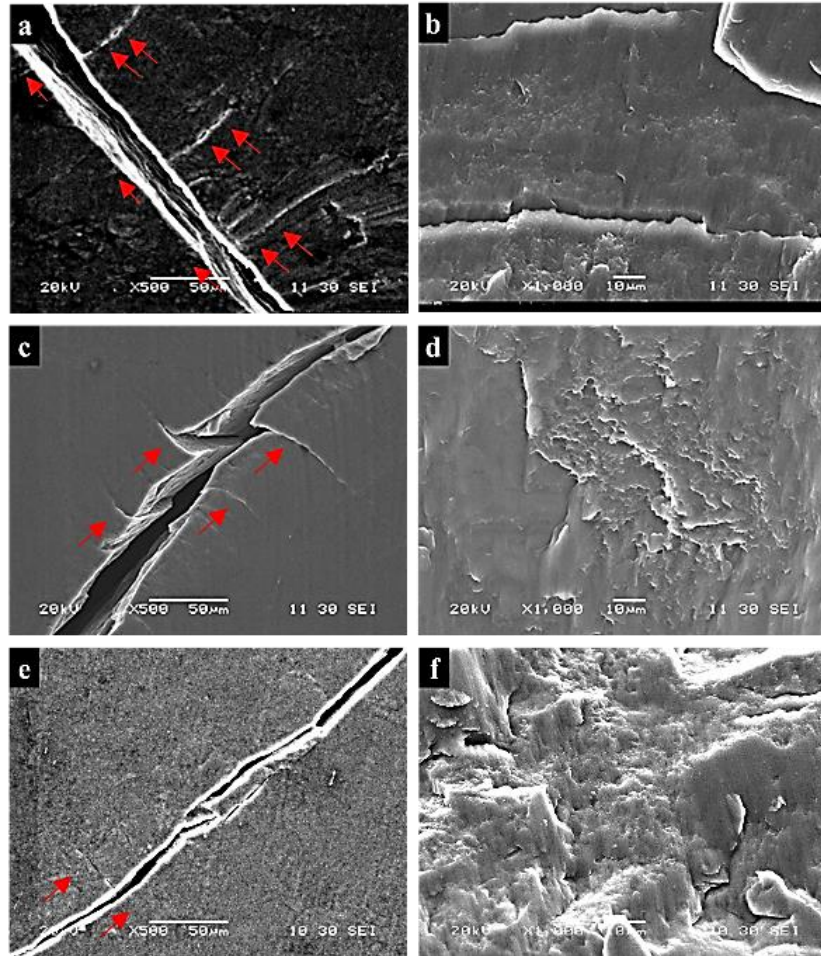


Figure 4.20: Fracture surface SEM macro (a, c, e) and micrographs (b, d, f) of A6 samples confined rolled at 200°C, 250°C and 300°C respectively after quasi-static compression along ND

The fracture surface microstructure of the rolled samples shown in fig. 4.20 b, d, f suggests that the fracture surface was almost flat at lower temperatures (200°C and 250°C) with shallow dimples and slightly deeper dimples observed at 300°C. The relatively clean edges of the tearing regions at lower temperatures showed low

ductility of the alloy (200°C). Also, some sheet like micro-facets were observed in the samples rolled at 200°C.

4.6 Chapter summary

The effect of addition of 6 wt.% Al on the microstructure, deformation mechanisms and ultimately the mechanical behavior of Mg alloys was emphasized in this chapter. The average grain size of these alloys like AZ31B was fine enough to provide both strength and ductility along with reduction of the basal texture intensity contributing to shift in texture. Surprisingly, these alloys didn't exhibit twinning when studied using average misorientation although few twins can be observed in optical micrographs. This may be due to the reason that most of the grains inside twins might have recrystallized at 200°C and could be resolved only through the EBSD technique. With increase in wt.% Al, the recrystallization completion temperature also shifts to higher temperatures. The average grain size and recrystallized grain size were lower in the case of samples rolled at 250°C in contrast to 200°C for AZ31B alloys signifying the completion of recrystallization in that temperature range. There was a suspected change in DRX mechanism from CDRX in samples rolled at 200°C and 250°C to DDRX in samples rolled at 300°C indicating the switch of DRX mechanisms as DRX gets completed in these alloys but the change was unclear since recrystallized grains are also free of misorientation .

In terms of precipitation, these alloys exhibited continuous precipitation at lower temperatures whereas at the higher temperatures, there was a co-existence of both continuous and discontinuous precipitation hence probing the need to

investigate the balance between particle stimulated nucleation and Zener pinning/solute drag effect. These alloys exhibited the right balance between pinning and particle stimulated nucleation (PSN) to act as nucleation sites for dynamic recrystallization and effectively curb grain boundary migration as well to form a well refined microstructure. The material exhibited good mechanical behavior (both strength and ductility) when rolled at higher temperatures. They also exhibited significant strain rate hardening and excellent strain hardening rates due to the ideal volume fraction of particles for precipitation hardening. The plate shaped particles present in large proportion in samples rolled at 250°C also acted as strengtheners by increasing the drag force exerted in grain boundaries in comparison to the spherical counterparts.

Schmid factor maps suggested the invocation of non-basal slip systems in all the samples which is a reason for the increase in ductility of these alloys when tested under dynamic strain rates. This alloy in general proved to be good for structural applications as assumed earlier. However, extensive studies need to be carried out to study the texture of these alloys exclusively to ensure isotropic behavior and prevent premature catastrophic failure in these materials.

CHAPTER 5: Mg-9%Al

In this chapter, the focus would be on the effect of supersaturation of Al in Mg-Al binary alloys. The maximum solid solubility of Al in Mg is 11.8 at. % at 710K. This alloy was created with an intention to study the effect of overcrowding the Mg system with supersaturation of Al. The alloy is particularly complex with precipitation, different size ranges (both micro and nano-sized precipitation), morphologies and mechanisms. The type, nature, morphology of precipitation will be studied with the help of transmission electron microscopy (TEM). SEM-EBSD will be used to study the other aspects such as deformation mechanisms, dynamic recrystallization etc. similar to the work that has been done with Mg-6 wt.% Al (A6) and AZ31B alloys. Again, the results of microstructure will be correlated with their mechanical behavior under compression at different strain rates.

5.1 Optical microstructure

Fig. 5.1 shows the optical micrographs of the Mg-9 wt.% Al (A9) alloys (a) before and after confined rolling at (b) 200°C, (c) 250°C, and (d) 300°C, respectively. From the micrographs, it could be clearly seen that there was only partial dynamic recrystallization in these alloys. The average grain size remained coarse (in the order of 200 μ m and greater) for both the baseline and confined rolled alloys. Severe deformation and extensive twinning could also be observed in the coarse grains. The necklace structure which has been a common factor for both AZ31B and A6 rolled at lower temperature was missing in this case. Instead, the structure remains intact at all the temperatures. The microstructure is composed of excessive number of twins, stacking faults and shear bands. Again, this kind of a peculiar behavior

could not be observed through the restricted resolving power of optical microscopy and hence techniques like EBSD and TEM were necessary to understand the deformation mechanisms, extent of recrystallization if any etc.

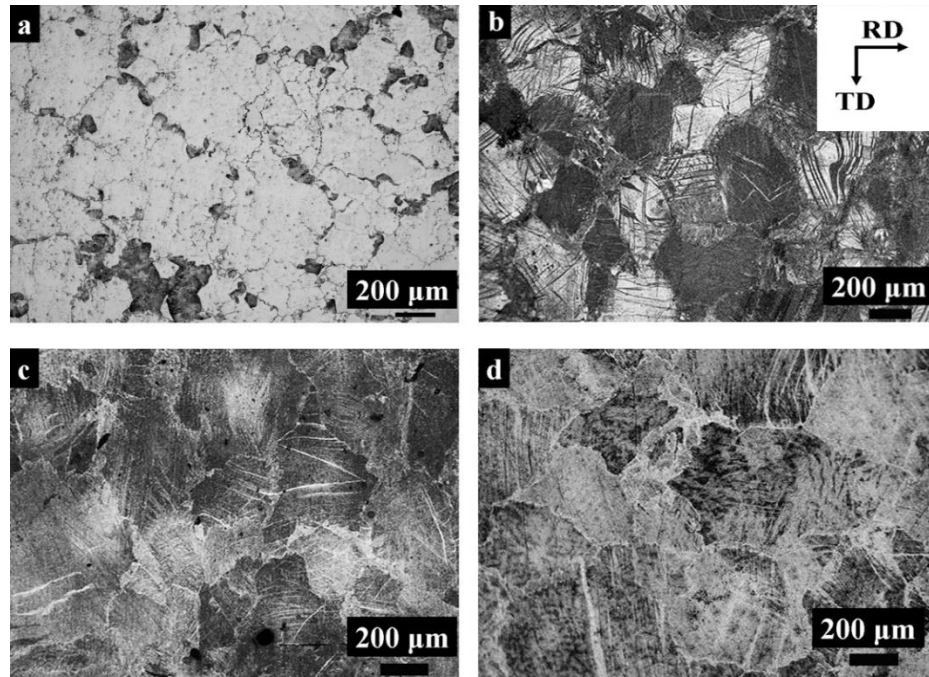


Figure 5.1 Optical micrographs of A9 alloys (a) before rolling and after confined rolling at (b) 200°C, (c) 250°C and (d) 300°C along normal direction (ND)

5.2 SEM – EBSD studies

Looking from the ND-IPF maps in fig. 5.2, the majority of the grains have their c-axes parallel to the normal direction (ND) of the sheet (red color signifies grains, with their basal poles oriented along ND) indicating strong basal texture. Twinning has been found in samples rolled at 200°C and evidence of recrystallization inside twins could be observed. The average grain size of the rolled alloys looks deceiving when compared with the optical micrographs. This might be because EBSD resolved even finer grains (possibly in nm scale) so the grain size values averaged a lot lesser. The trend of the average grain size of the samples initially decreased

with temperature and expectantly increased with temperature due to availability of thermal energy for grain coarsening as observed in other alloys studied.

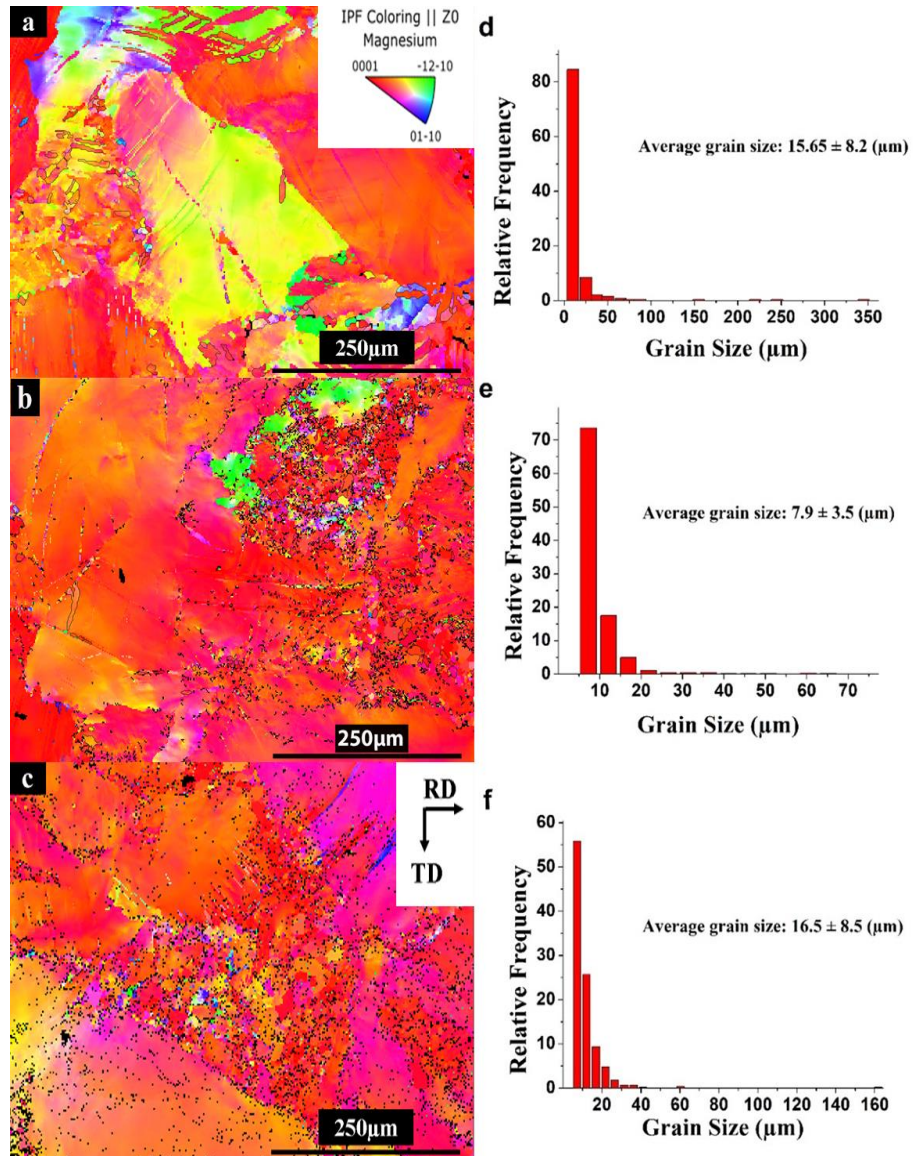


Figure 5.2 Inverse Pole Figure (IPF) map and the corresponding grain size measurements along ND plane of A9 alloys confined rolled at (a)&(d) 200°C, (b)&(e) 250°C and (c)&(f) 300°C respectively.

5.2.1 Texture

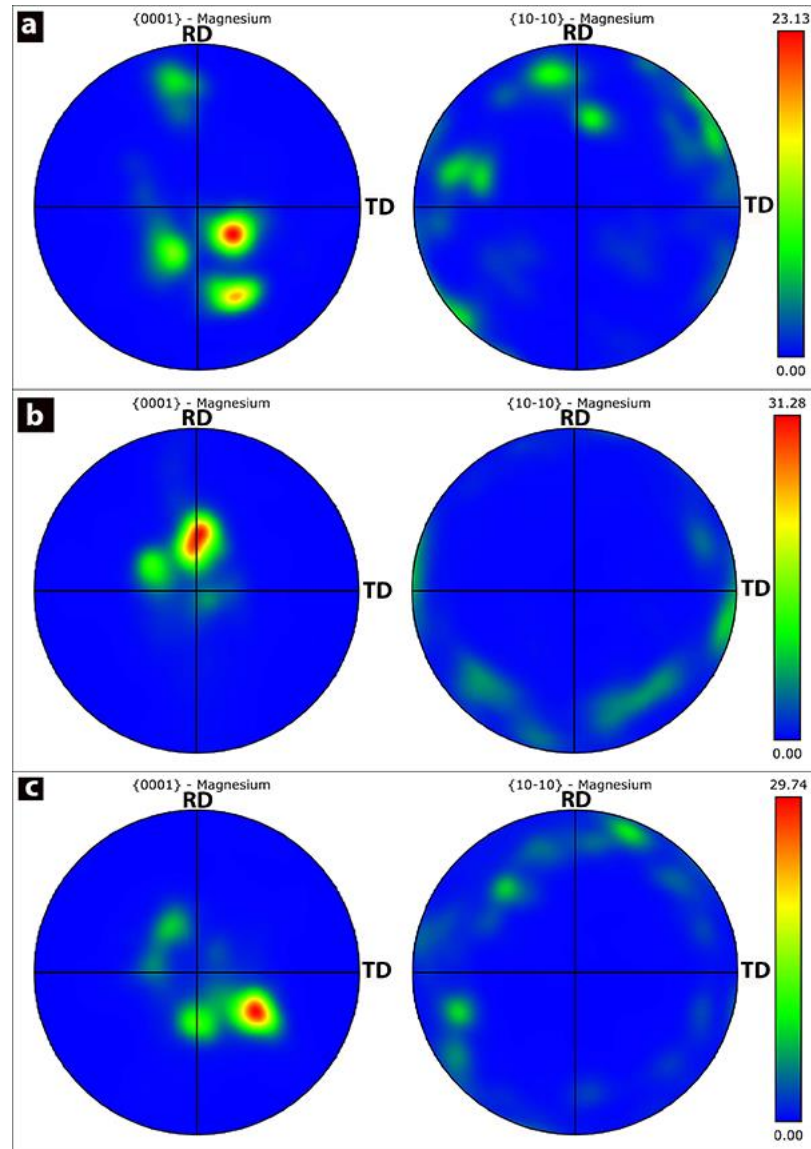


Figure 5.3 (a) –(c) Texture intensity along the ND of $\{0001\}$ and $\{10\bar{1}0\}$ planes of A9 alloys confined rolled at (a) 200°C, (b) 250°C and (c) 300°C

Fig. 5.3 shows the $\{0001\}$ and $\{10\bar{1}0\}$ pole figures of the as-rolled plates. The basal texture was not strong and had slight randomization probably due to the combined effect of higher volume fraction of precipitates and confined rolling. c-axis was no longer parallel to the normal direction at all the three rolling temperatures. While there was no randomization in case of AZ31B and a slight shift

in texture in case of A6 alloys, addition of 9 wt.% Al to Mg caused splitting of basal poles in case of A9 alloys. It can be observed that in addition to the strong texture, there is a weak texture where the c-axis is inclined towards the RD for the samples rolled at 200°C and 250°C, but along the TD for the sample rolled at 300°C. Textural intensity described in terms of MRD indicated qualitatively by the MRD number above the color bar next to the pole figures is increasing in the order of 200°C > 300°C > 250°C. It was puzzling that despite very little dynamic recrystallization being observed in these alloys, the texture appeared to be slightly randomized and needed to be evaluated further.

5.2.2 Grain boundary character distribution (GBCD)

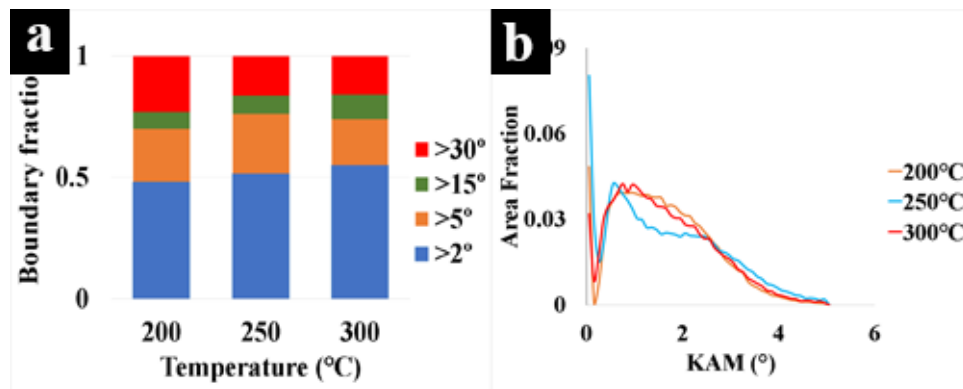


Figure 5.4 (a) Grain boundary distribution and (b) Kernel average misorientation distribution of A9 samples rolled at 200°C, 250°C and 300°C along ND

The GBCD map in fig. 5.4 (a) shows that the LAGB fraction (i.e., grain boundary angle <15°) for samples rolled at 250°C and 300°C were higher compared to samples rolled at 200°C and progressively increased as the rolling temperature was increased. In the case of AZ31B and A6 alloys, the LAGB fraction was the highest during their peak recrystallization temperatures of 150°C and 250°C respectively. Hence, the increase in LAGB fraction in the case of A9 alloys indicated higher

propensity of dynamic recrystallization when rolled at higher temperatures. KAM values in figure 5.4(b) show local lattice distortion or localized deformation through the presence of geometrically necessary dislocations (GNDs). The KAM maps reveal that the regions with higher values of KAM accumulated lots of dislocations and subsequently, sub-grain boundaries which can offer a sufficient strain gradient for triggering CDRX [163]. The KAM maps show that samples rolled at 200°C and 250°C were more strained in comparison to the other samples. This result agreed with the findings from A6 alloys where strain was higher at lower temperatures but not with AZ31B alloys where dynamic recrystallization was complete at a rolling temperature of 200°C and KAM values were low for all the samples with rolling temperatures below it.

5.2.3 Average misorientation

The misorientation angle distribution of the rolled samples, obtained from the EBSD data, is shown in fig. 5.5. It showed a higher fraction of grains with misorientation angle $<50^\circ$ and a lesser fraction at higher angles $>50^\circ$ for all samples. A steady evolution and reduction of misorientation was found at $\sim 30^\circ$ and $\sim 90^\circ$, respectively. To find the possibility of twinning, the grain boundary character distribution was plotted.

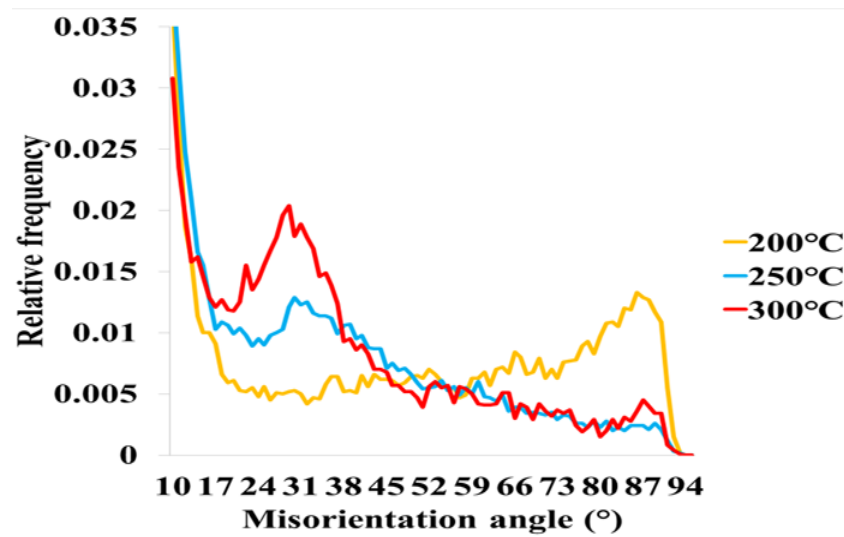


Figure 5.5 Misorientation angle distribution showing a progressive increase and decrease of $30\pm 5^\circ$ misorientation and $86\pm 5^\circ$ twin boundaries, respectively, as the rolling temperature increases

The fraction of twin boundaries decreased as rolling temperature increased. It is expected that the contribution of twinning towards overall deformation would decrease with increase in rolling temperature. Also, the volume fraction of twins observed were much less or literally nonexistent at higher temperatures, giving proof that slip was the dominating mechanism at 250°C and 300°C.

From fig. 5.7, it could be deciphered that the fraction of LAGBs became gradually higher and another local peak aroused at $30\pm 5^\circ$ as rolling temperature was increased. This peak became gradually evident as the temperature increased which supports the observed dominance of 30° [0001] grain boundaries (GB) during rolling, responsible for the nucleation of new $[2\bar{1}\bar{1}0]$ basal fiber orientation in the unDRXed grains through CDRX, speaking in terms of orientation. These 30° [0001] GBs which have been observed in various recrystallized microstructures of Mg alloys were mainly attributed to the formation of $\Sigma 13a$ coincident site lattice

boundaries (CSL). Some molecular dynamic (MD) simulations suggest that such GBs have both low interfacial energy and high mobility in comparison to other boundaries due to the easy glide of Shockley partial dislocations making them an easy route for accommodating sub-grain rotation [163]. This kind of grain boundary is developed favorably to reduce grain boundary energy during grain growth.

At lower rolling temperatures such as 200°C, basal slip and deformation twinning generally operate to comply with the strain incompatibility at the grain boundaries, basal dislocations with $\langle a \rangle$ burgers vector accumulate near twin boundaries and create huge internal stresses due to the remaining elastic distortion exceeding the locally necessary CRSS for non-basal slip (which is usually much larger than basal slip at lower temperatures). The rearrangement of these dislocations give rise to HAGBs containing high density of dislocations along those grain boundaries.

The microstructure of the sample rolled at 200°C was composed of many twins, mainly consisting of compression twins (CTWs) of the type $\{10\bar{1}1\} \langle 10\bar{1}2 \rangle$ (misorientation angle of 56°), followed by tensile twins (TTWs) of the type $\{10\bar{1}2\} \langle 10\bar{1}1 \rangle$ (misorientation angle of 86°), and few double twins (DTWs) of the type $\{10\bar{1}1\} - \{10\bar{1}2\}$ [200]. Compression twins and tensile twins were marked by green color in fig. 5.6 (a). These are the two most common twin modes of single twins that form to accommodate compression strain and extension strain along the c-axis, respectively. Tensile twins can grow thick and even overtake the grain and generally reach profuse levels without causing material failure. However, they may improve the material's ductility while compromising the material's strength. But

the number and size of compression twins remains small and might nucleate a second tensile twin inside their domain, which will eventually grow and fill the compression twin lamella. This would result in a double twin. When a compression twin transforms to a double twin (marked by the blue color in fig. 5.6 (a)), it produces a misorientation angle of 37.5° about the $\langle 11\bar{2}0 \rangle$ axis. Presence of higher number of double twins (marked by the red color) in these samples (as shown in fig. 5.6 (a) indicate the transitioning of compression twins into double twins. This fact is also reiterated by the misorientation angle distribution given by fig. 5.6 (b).

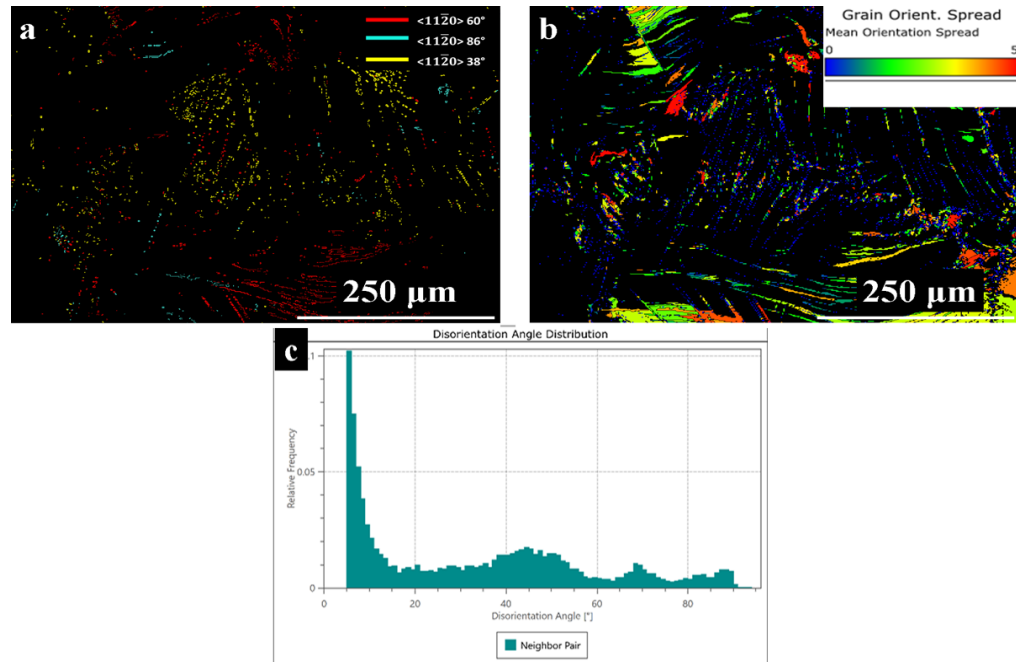


Figure 5.6 (a) EBSD map showing DTWs (red), TTWs (blue), and CTWs (green); (b) evidence of recrystallization in twins and (c) grain boundary character distribution showing the twin distribution

5.2.4 Twin induced recrystallization

Tension twins act as effective sinks for lattice dislocations along their boundaries, hence they can grow easily [200]. The absorption of basal dislocations could also relieve local stress and reduce dislocation pileups along the tension twin

boundaries. Therefore, basal dislocations are not found to accumulate, irrespective of the crystallographic orientation of the tension twins with respect to the applied stress. Therefore, activation of recrystallization inside tension twins is not possible due to inadequate levels of elastic strain energy [201]. In the case of the compression and double twins, due to easy basal slip and accumulation of dislocations around twin boundaries, recrystallization is often observed as seen in fig. 5.3b and supported by [29, 201-203].

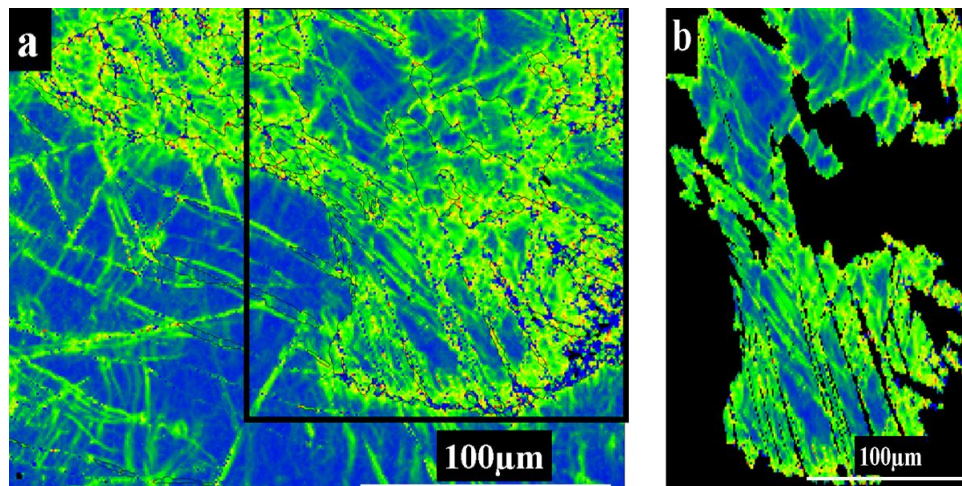


Figure 5.7 KAM map showing the distribution of stored strain energy in (a), and in (b) a close-up illustration of the stored strain energy in the twinned location marked by the yellow box in (a)

For parallel double twin arrays, recrystallized grains can only extend up to the interior boundary of the twin since twin boundaries act as strong barriers for grain growth. This results in the formation of bands of recrystallized grains. As seen in the KAM map in fig. 5.7, due to the lower residual stored energy of the adjacent grains, the recrystallized grains inside twins could not consume them and expand into the neighboring deformed parent grains [202]. This is the reason why twin induced recrystallization could not alter the texture of the material to a greater extent in this case. But the recrystallized grains originating from DTW-DTW and

DTW-grain boundary (GB) intersections will grow towards the deformed parent grains and subsequently in the neighboring deformed grains, extending quickly into regions of higher stored energy as seen in KAM map shown in fig. 5.7 during further deformation eventually weakening its texture and improving its formability [202].

5.3 Deformation mechanism

In this section, the effect of supersaturation of Al in Mg was studied with respect to dynamic recrystallization modes and deformation mechanisms. The balance between particle stimulated nucleation and Zener pinning/ solute drag needed to be studied as the volume fraction of precipitates would be higher. It is suspected that higher precipitation might also have an effect in evoking non-basal slip systems.

5.3.1 Grain orientation spread (GOS)

Grain orientation spread (GOS) is a measure of the material's deformation (particularly quantified through the distortion of grains). The GOS(*i*), or the deformation of the *i*th grain, can be determined by the following equation:

$$GOS(i) = \frac{1}{J(i)} \sum_j \omega_{ij} \quad , \quad (5.1)$$

where $J(i)$ is the number of pixels in grain *i*, ω_{ij} is the mis-orientation angle between the orientation of pixel *j* and the mean orientation of grain *i* [204]. Most of the previous studies using this approach characterized the GOS threshold for dynamic recrystallization to be 1°-2° for different materials since recrystallized grains tend to have a uniform intragranular orientation [205-208]. But a recent study by A. Hadadzadeh et al. delineated the recently recrystallized grains with $GOS < 2^\circ$ from DRX-deformed grains with $2^\circ < GOS < 5^\circ$ (i.e., those that recrystallized at earlier

stages of the deformation) [209]. They concluded that DRX grains contributed to the texture weakening and randomization whereas, the deformation of un-recrystallized parent grains where the c-axis is oriented towards the deformation axis is responsible for the basal texture of the material. As shown in figures 5.8(a-c), in the case of the sample rolled at 200°C, the lower GOS value and lower recrystallized area fraction could be attributed to recrystallization of the grains inside twins. Although the average orientation spread value should decrease with increase in rolling temperature due mechanisms such as dynamic recovery etc., in the case of sample rolled at 250°C, it was higher than expected due to a larger fraction of un-recrystallized deformed parent grains (with an accumulation of dislocations and development of misorientation within them) and a lesser twin fraction (thus a lessened scope for twin DRX). As the temperature reached closer to the nominal recrystallization temperature i.e., 300°C ($> 0.5T_m$), more considerable amount of DRX and relaxation mechanisms due to thermal energy occurred along with grain growth; hence, the contribution to the GOS from the deformed grains was reduced. Also, an increase in recrystallized grain size was clearly observed. The analysis of the GOS corroborated well with the KAM and GBCD maps.

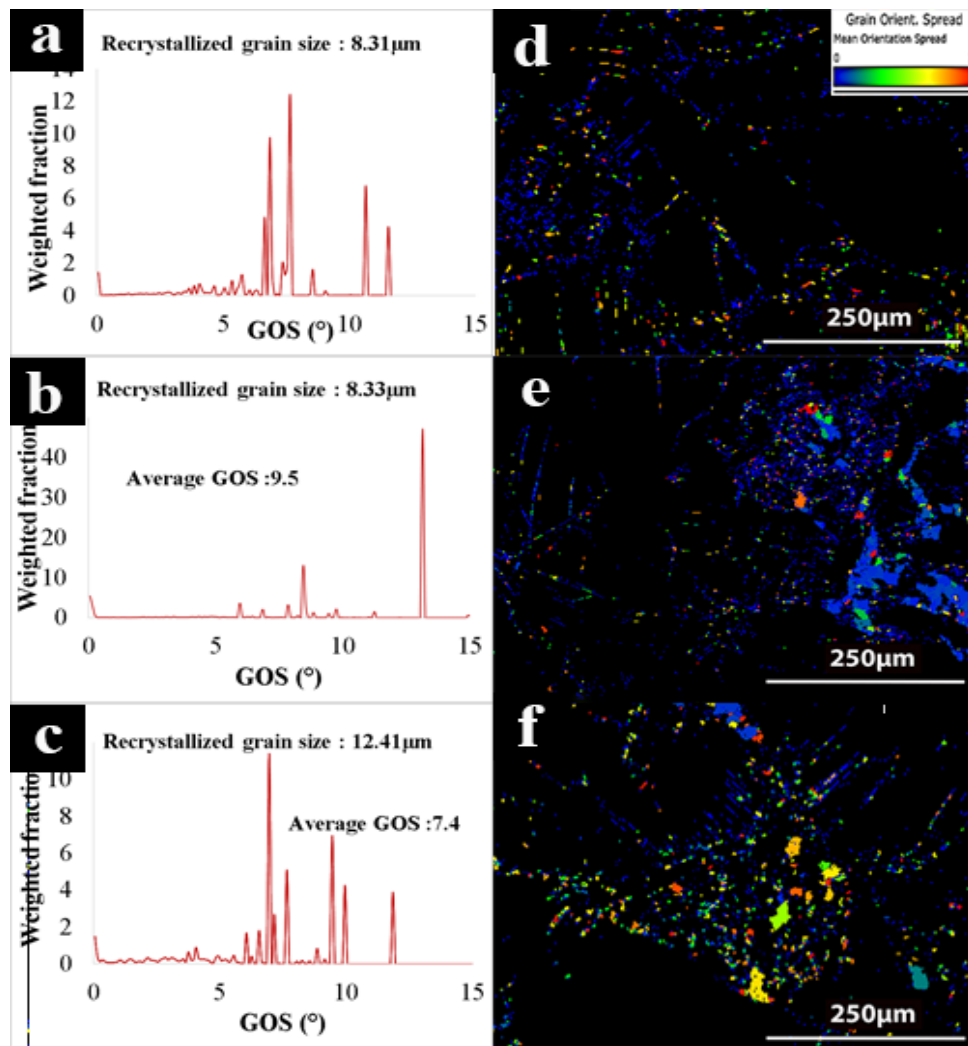


Figure 5.8 (a) – (c) GOS maps and (d) – (f) the corresponding recrystallized areas partitioned using the GOS < 2° criterion of samples rolled at 200°C, 250°C, and 300°C, respectively along ND

Compared to the 200°C and 300°C samples, along with the high GOS, KAM and higher fraction of LAGBs, the recrystallized area fraction is also higher for the case of the sample rolled at 250°C. These results are in line with the results from AZ31B and A6 alloys where the lowest GOS was observed in temperatures where maximum recrystallization occurred. If addition of Al to Mg shifts the recrystallization to higher temperatures (150°C-200°C in case of AZ31B and 250°C - 300°C in case of A6 alloys) then A9 alloys are expected to recrystallize at an even

higher temperature than 300°C. However, recrystallized grain size would be very large and would defeat the purpose.

5.3.2 Schmid factor

Fig. 5.9 indicates the predominance of basal slip at lower rolling temperature of 200°C. As the temperature increases, the Schmid factor values for basal slip gradually start decreasing along with a concurrent increase of the Schmid factor values of non-basal slip, particularly the pyramidal (c + a) slip system. The Schmid factor maps also suggest the same trend with the activity of non-basal slip increasing with rolling temperature.

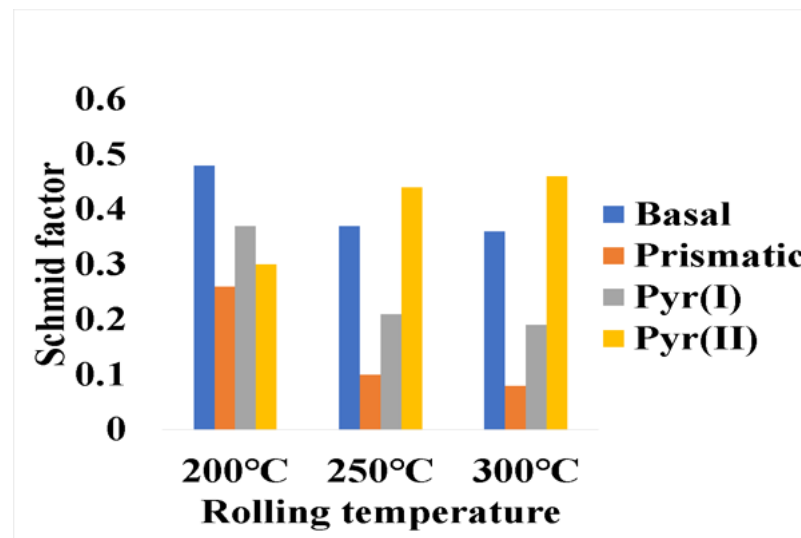


Figure 5.9 Variation of Schmid factor along ND with rolling temperature

From the Schmid factor maps in fig. 5.10, it can be inferred that as the rolling temperature increases, the Schmid factor values for basal, prismatic, and pyramidal I plane decreased and the pyramidal II plane increased. This is because the CRSS of the non-basal slip modes drastically decrease due to thermally activated dislocation glide [22, 26, 210].

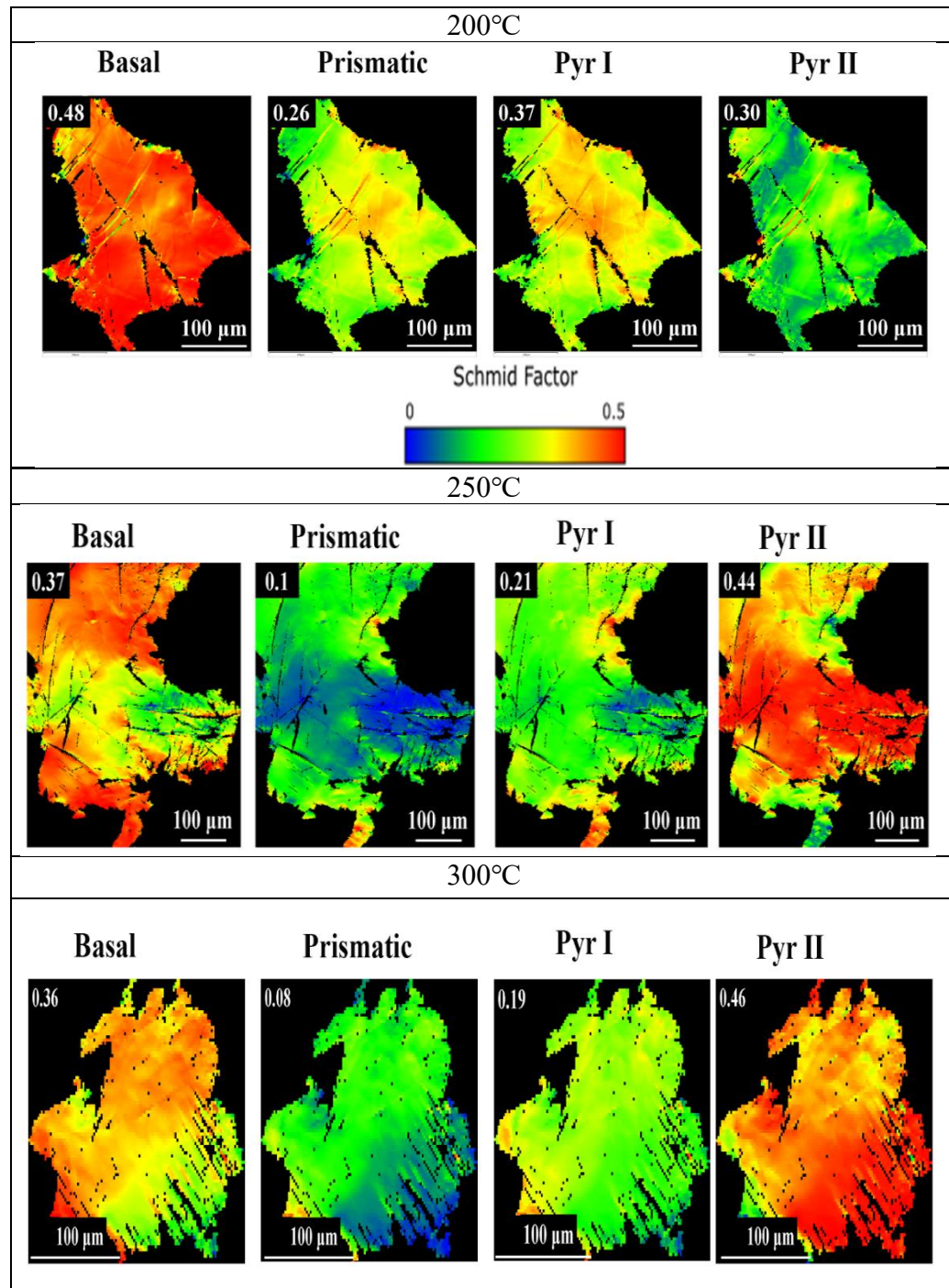


Figure 5.10 Schmid factor maps for basal and non-basal slip systems for samples rolled at 200°C, 250°C and 300°C respectively

In this case, at 200°C, although twin based recrystallization occurred, it was not effective to evoke non-basal slip systems. Only temperature was effective in reducing the CRSS of the non-basal slip systems thereby activating them.

5.3.3 DRX mechanism

Continuous dynamic recrystallization (CDRX) consists of the continuous rearrangement and absorption of dislocations at sub-grain boundaries. This mechanism consists of the formation of low-angle grain boundaries (LAGB) at low strains and a progressive increase of the misorientation of these sub-boundaries as the LAGBs evolve into HAGBs. Fig. 5.11 illustrates line profiles of misorientation along the line AB for samples rolled at different temperatures. It is evident that there was an increase in misorientation of 15°-25° from point-to-origin, suggesting that there was a gradual rotation of the orientation in the un-DRXed grain in all the samples. The observation in all three samples provided sound evidence for the occurrence of CDRX with high activity of LAGBs. In a typical CDRX mechanism, it is inferred that the more mobile dislocations would activate and accumulate near LAGBs which, with an increase in strain, will tend to transform into HAGBs.

This phenomenon was proved by the increase in low angle grain boundaries (LAGBs) in this alloy as rolling temperature increased hence suggesting deformation of coarse parent grains to form sub-structures. However, there was an equally opposing force which didn't allow CDRX to proceed was required to be identified and it was probably related to precipitation. Hence, the need for understanding the effect of supersaturation of matrix with precipitate particles was reinforced.

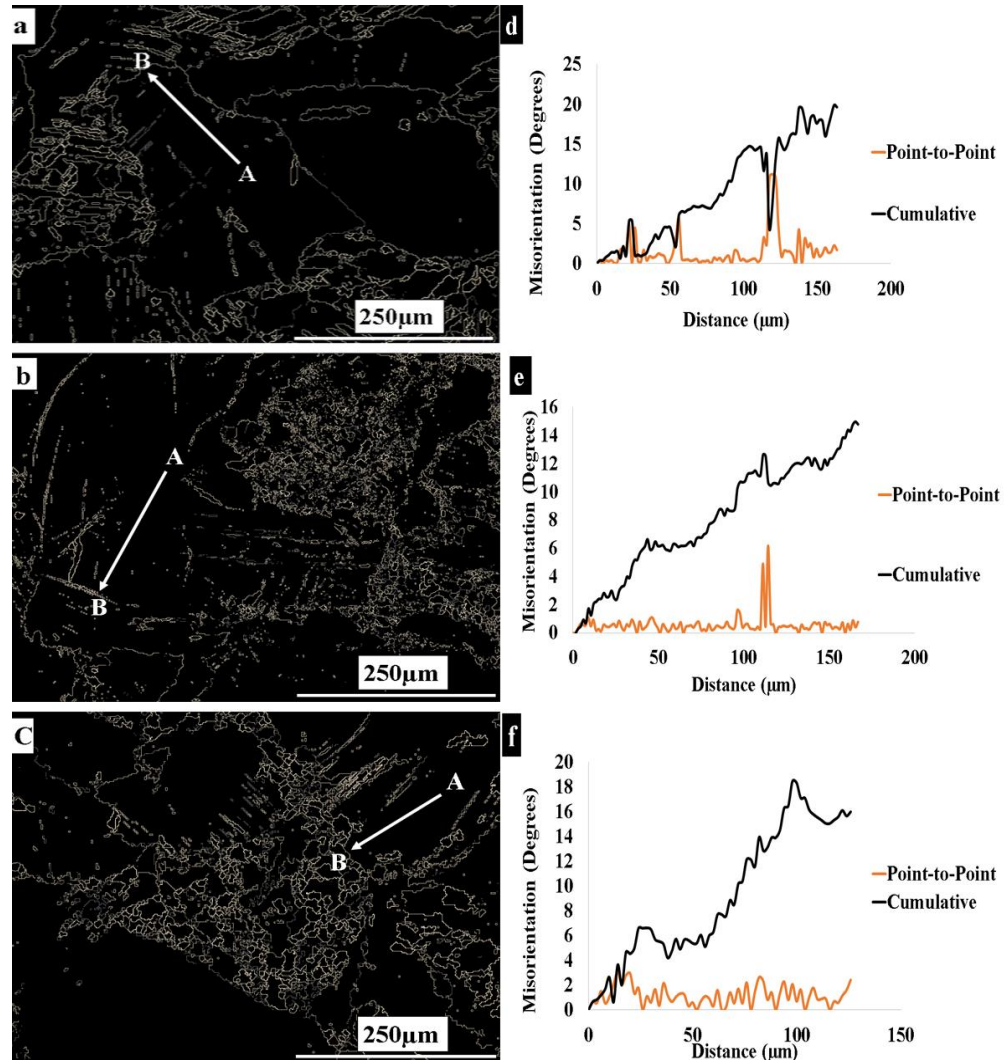


Figure 5.11 (a)-(c) HAGB map of samples rolled at 200°C, 250°C, and 300°C and (d) –(f) the corresponding line profile of misorientations along the line AB in (a)-(c) respectively

5.4 Effect of Precipitation

5.4.1 Continuous and discontinuous precipitation

In the case of Mg-9%Al, all the three samples showed both continuous and discontinuous precipitation. However, at the rolling temperature of 200°C, the proportion of discontinuous precipitates (DP) was much higher compared to continuous precipitates (CP) and vice versa for the samples rolled at 300°C as shown in fig. 5.12. In the case of sample rolled at 250°C, both the precipitates

occurred simultaneously in equal proportions. In short, at 200°C, there were more CPs but fewer DPs, at 250°C, they possessed fewer but larger CPs and mainly DPs whereas at 300°C, the microstructure contained both coarser DPs and finer nano-sized DPs.

At lower temperatures, grain boundary diffusion controls secondary precipitation hence facilitating the formation of discontinuous precipitates at the grain boundaries. As the temperature increases, bulk diffusion takes over which encourages continuous precipitates to form. Also, these continuous precipitates stop further discontinuous precipitation by reducing the amount of chemical driving energy available for its initiation and propagation [108]. However, volume diffusion should allow growth to occur at both the locations as well as facilitate transfer of Al solute from the grain interior to the boundary, hence causing precipitate coarsening.

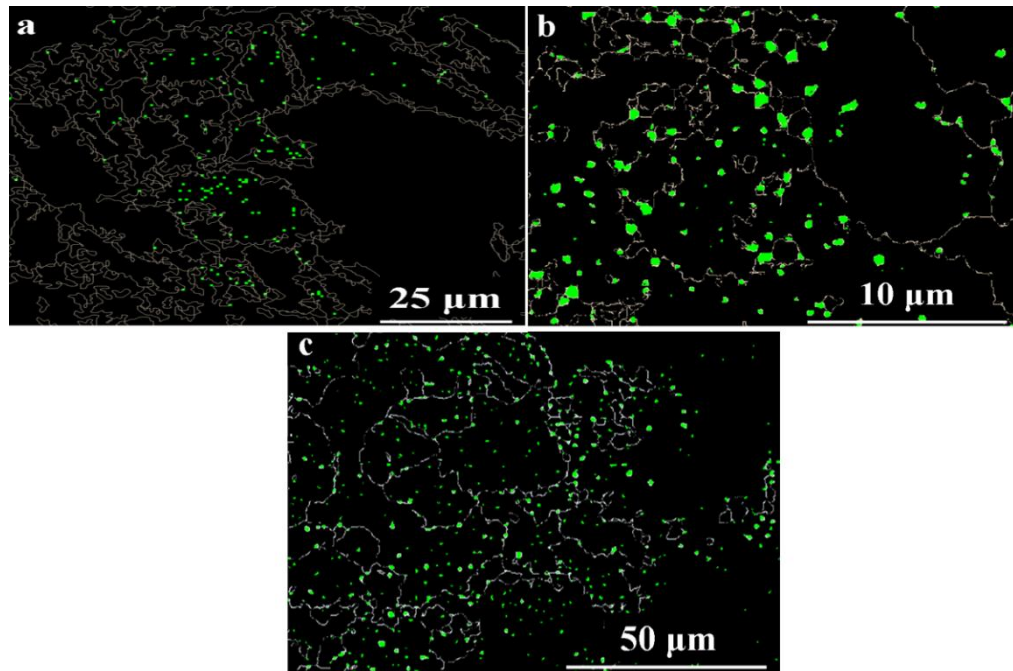


Figure 5.12 (a-c) EBSD images of continuous and discontinuous precipitation in samples rolled at (a) 200°C, (b) 250°C, and (c) 300°C respectively.

5.4.2 Particle Stimulated Nucleation (PSN) and Zener pinning:

As observed from figure 5.13, particles acted as a nucleation site for LAGBs and eventually became sub-grain boundaries. In addition to PSN, the presence of larger volume fraction of particles was suspected to pin grain boundaries through the mechanism of Zener drag. Particle pinning due to solute segregation resulted in reduction of grain boundary mobility which may alter the activity of other recrystallization mechanisms. For example, discontinuous dynamic recrystallization (DDRX) where nucleation occurs at pre-existing grain boundaries through grain boundary serration and rotation of the resulting sub-grains is inhibited due to reduced grain boundary mobility [119].

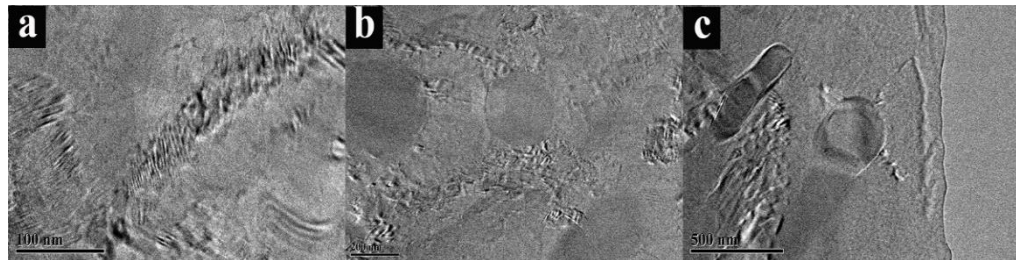


Figure 5.13 (a)-(c) LAGBs forming in contact with precipitates in samples rolled at 200°C, 250°C and 300°C respectively.

Improvement in strength of Mg-9%Al alloys could be attributed partly to refined DRx grains but majorly to $Mg_{17}Al_{12}$ precipitates. The influence of these precipitates in pinning dislocations through Orowan strengthening mechanism has been studied and reported widely. The presence of $Mg_{17}Al_{12}$ particles contribute to accommodate local strain to reduce stored deformation energy leading to lack of sufficient stored energy for stimulating recrystallization. Fine precipitates dispersed in grain interior or at grain boundaries could produce the pinning effect on grain boundary migration to restrict recrystallization [69].

Interface between the matrix and second phase particles is also an important factor for pinning dislocations in Mg alloys. Plate shaped $Mg_{17}Al_{12}$ phase generated in the grain interiors was almost parallel to $\{0001\}$ as basal precipitation. Neither large nor thin basal precipitates are effective for pinning dislocation but the spherical precipitates refined from rod shaped particles along grain boundaries have a dominant influence in inhibiting recrystallization [69]. In the case of spherical particles, size and volume fraction are two important factors. There is an important criteria for the occurrence of recrystallization i.e. the driving force for recrystallization (F_d) must be greater than the Zener pinning pressure (F_z). In case of AZ91, as calculated by Zhong-Zheng Jin et al. F_z value increases from 1.4×10^5 to $8.8 \times 10^5 \text{ Nm}^{-2}$ with increase in deformation but F_d ranges from 0.8 - $1.0 \times 10^5 \text{ Nm}^{-2}$. Since F_z value is higher than F_d during both initial and subsequent (due to variation in precipitate morphology) deformation stages, it implies that there is a strong pinning effect of precipitates on grain boundaries and consequent inhibition of complete dynamic recrystallization of the microstructure [69].

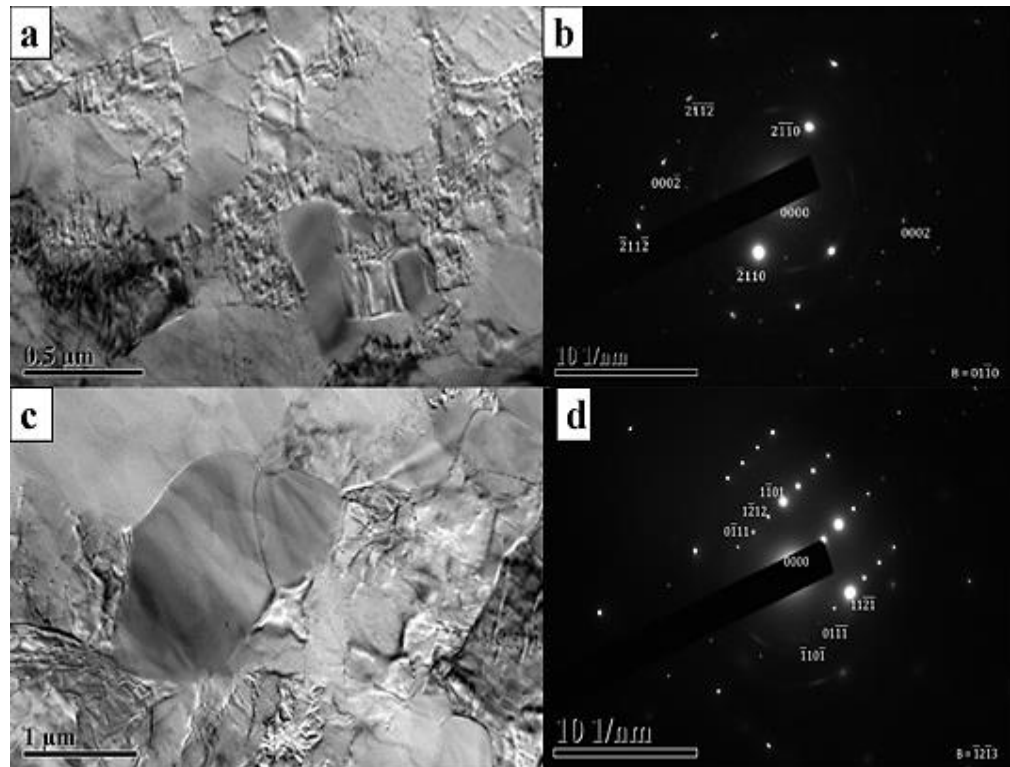


Figure 5.14 Particles pinning grain boundaries shown in bright field (BF) and the corresponding selected area diffraction (SAD) pattern in samples rolled at (a)-(b) 250°C and (c)-(d) 300°C, respectively.

The drag pressure, P_Z , exerted per unit area of grain boundary assuming random distribution of spherical particles with radius, r and volume fraction, F_v , is given by equation 5.2:

$$P_Z = \frac{3F_v\gamma_b}{2r} \quad (5.2)$$

It can be clearly seen that fine particles and higher volume fraction of precipitates maximize the pinning pressure. In the case of A9, the high density of nano- and micrometer-sized precipitates (as shown in fig. 5.14 and 5.15) act as strong barriers for grain boundary migration hence, retarding recrystallization in all the three cases. But in case of A6, dispersion and average size of precipitates was much uniform

hence this pinning effect turned into an advantage by restricting grain growth rather than excessively mitigating grain boundary migration.

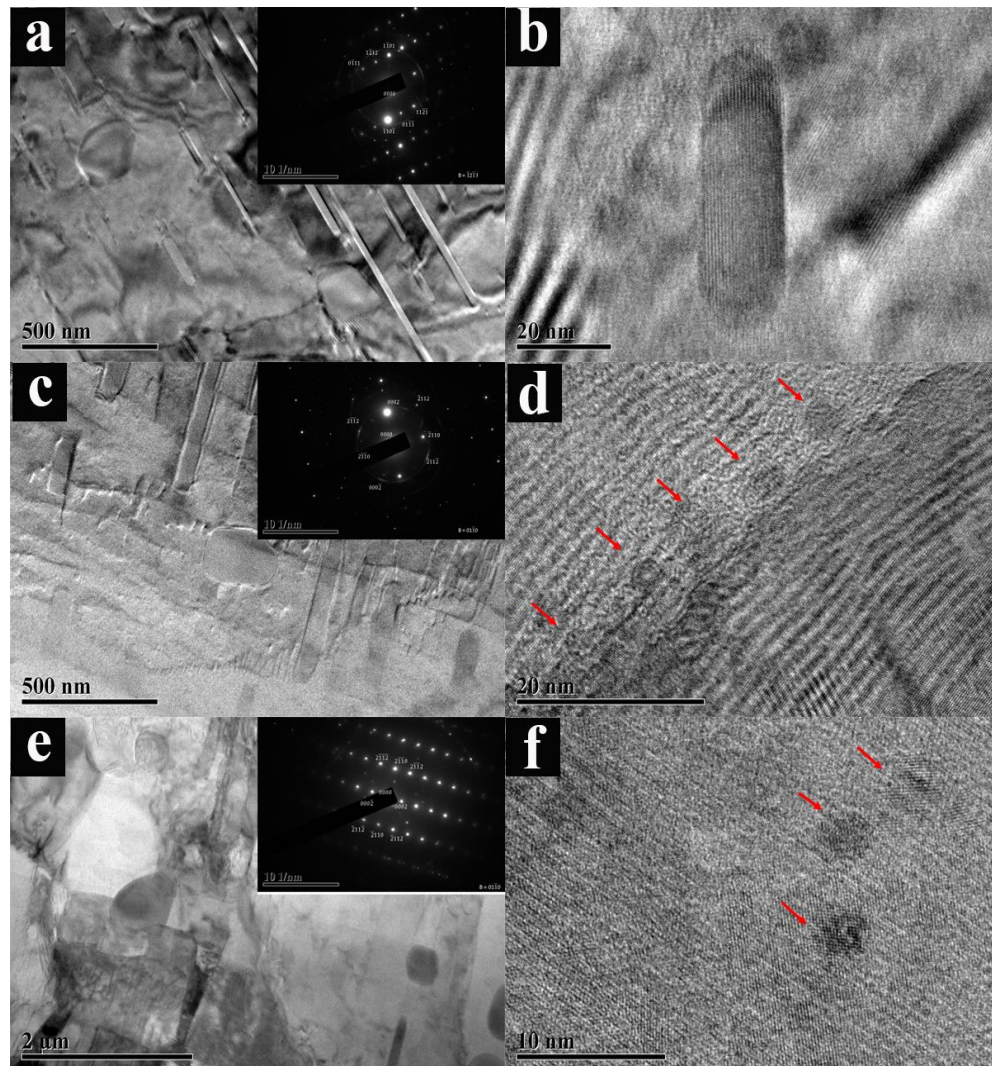


Figure 5.15 Nano-scale precipitates dispersed inside coarse deformed unrecrystallized grains at (a,b) 200°C, (c,d) 250°C, and (e,f) 300°C at higher (with SAD patterns as inset) and lower magnifications, respectively. A higher magnification was chosen for A9 samples at 300°C (c) to for visualizing precipitate morphology due to the larger precipitate sizes at that temperature.

Pinning effectiveness of a particle distribution in mitigating grain boundary migration is determined by volume fraction to radius ratio ($\frac{F_v}{r}$) according to Humphreys and Hartherly [93]. They argued that the Zener pinning [192] pressure plays a massive role in retarding primary recrystallization thereby affecting

nucleation, growth, and recrystallization texture, although Baker and Martin, and Chan and Humphreys reported otherwise [211, 212]. They further suggested the

critical $\frac{(F_v)^n}{r}$ is the key parameter controlling recrystallization kinetics where $\frac{1}{3} < n <$

1. Recrystallization of alloys containing bimodal particle size distributions containing both coarse ($> 1\mu\text{m}$) particles which act as sites for PSN and small particles which pin the migrating boundaries was done by Nes [213]. In this case, the driving pressure for recrystallization (P_D) is counterbalanced by Zener pinning (P_Z) in equation 5.3 to predict the critical particle size for nucleus growth, d_g , as given by equation where F_v and r refer to properties of the small particles.

$$d_g = \frac{4\gamma_b}{P_D - P_Z} = \frac{4\gamma_b}{\frac{\rho G b^2}{2} - \frac{3F_v \gamma_b}{2r}} \quad (5.3)$$

$$D_{lim} = \frac{4r}{3F_v} \quad (5.4)$$

Thus, the critical particle diameter for PSN, D_{lim} increases as the Zener pinning force increases, meaning fewer particles will be available as nuclei and the average size of recrystallized grains increases. Also, the particle dispersion level parameter, $\frac{F_v}{r}$, affects Zener drag pressure (P_Z , see Equation 5.2), critical particle size, d_g , number of viable recrystallization nuclei (see Equation 5.3), and the grain size at which normal grain growth will stagnate (D_{lim} , see Equation 5.4). The effect of the particle dispersion parameter on grain size after recrystallization is given in fig. 5.16 based on models predicted by Nes et al. and Wert et al. [213, 214]

There are three regimes in this graph.

1. $\frac{F_v}{r} < A$ (Grain growth limited size): The primary recrystallization grain size in this region is governed by the number of nucleation sites and a higher availability

of them ensures increases the propensity of grain refinement. However, if the material is treated at sufficiently higher annealing temperature, grain growth will occur up to D_{lim} . A minimum grain size can be achieved when D_{lim} reaches the point A.

2. $A < \frac{F_v}{r} < B$ (Nucleation limited size): In this regime, recrystallization follows the path of D_N as determined by the availability of nuclei. Since it is above the value of D_{lim} , abnormal grain growth occurs.

3. $\frac{F_v}{r} > B$ (No recrystallization zone): Zener pinning is now enough to suppress recrystallization and the precipitates stabilize the deformed microstructures.

D_{lim} represents the grain size at which normal grain growth ceases. D_N represents the recrystallized grain size after PSN. The number of available nuclei from large particles or other sites decreases as $\frac{F_v}{r}$ increases. At some dispersion level, $\frac{F_v}{r} > B$, the number of nuclei decreases to effectively zero, above which recrystallization cannot possibly occur.

Confined rolled A9 samples lie in the regime of $A < \frac{F_v}{r} < B$, almost tipping towards $\frac{F_v}{r} > B$ due to the super-saturation of Al in Mg. This leads to the availability of fewer nucleation sites for or the suppression of recrystallization.

AZ31B and A6 alloys lay in $\frac{F_v}{r} < A$ regime where particle dispersion level is controlled, and grain size refinement was achieved with grain growth limited by D_{lim} .

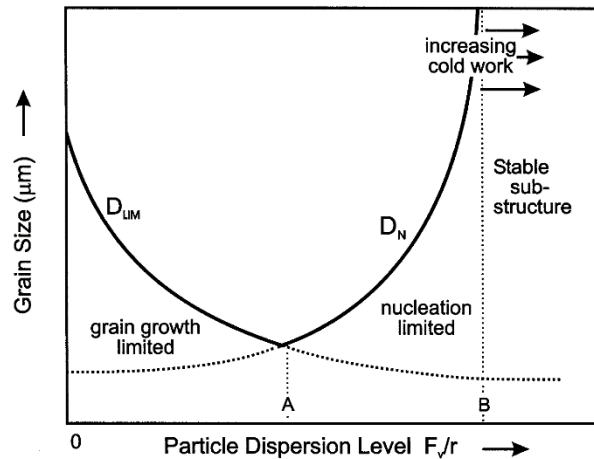


Figure 5.16 Effect of particle parameters on recrystallized grain size [213, 214]

5.4.3 Precipitate Morphology

All the samples consisted of both [0001] precipitate (c-axis) rods and spherical precipitates. However, the proportion of c-axis rods was higher for samples rolled at 200°C; the proportion of spherical precipitates was higher for samples rolled at 300°C; while they were equal in proportion for samples rolled at 250°C (fig. 5.17).

J. D. Robson and co-authors [130, 213-215] researched the effect of particle shape and habit plane on the deformation mechanisms of Mg alloys wherein they compared the role of basal plates and c-axis rods. For randomly oriented spheres, the effective interparticle spacing is indistinguishable on the prismatic and basal planes since the probability of cutting a spherical particle and the in-plane diameter would be the same with respect to both the planes. Therefore, the necessity for replicating the same analysis for spherical particles was not found. They predicted that c-axis rods are more effective strengtheners for basal and prismatic slip in comparison to plates and spherical particles since the probability of a plate/sphere being intersected by a basal plane is very low and the Orowan stress, $\Delta\tau$ (see

equation 5.5) required to bypass rod shaped precipitates is higher. Also, the aspect ratio plays a major part in this strengthening effect.

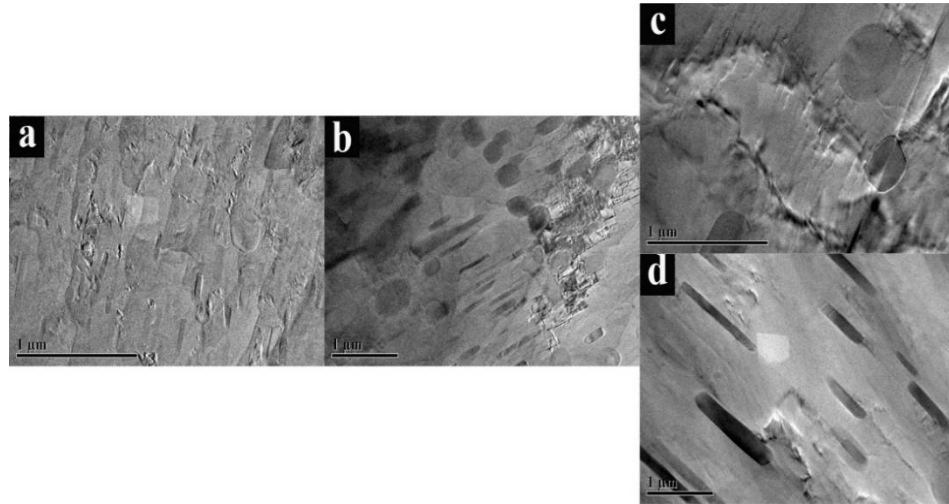


Figure 5.17 Precipitate morphology in samples rolled at (a) 200°C, (b)250°C, and (c, d) 300°C, respectively.

As the aspect ratio of the rods increase, they become more “rod-like” which increases the strengthening effect further. But as the basal plates become thinner and broader (“plate-like”), their predicted strengthening effect reduces.

$$\Delta\tau = \frac{Gb}{2\pi\sqrt{(1-\nu)}\lambda} \ln \frac{d_p}{r_0} \tag{5.5}$$

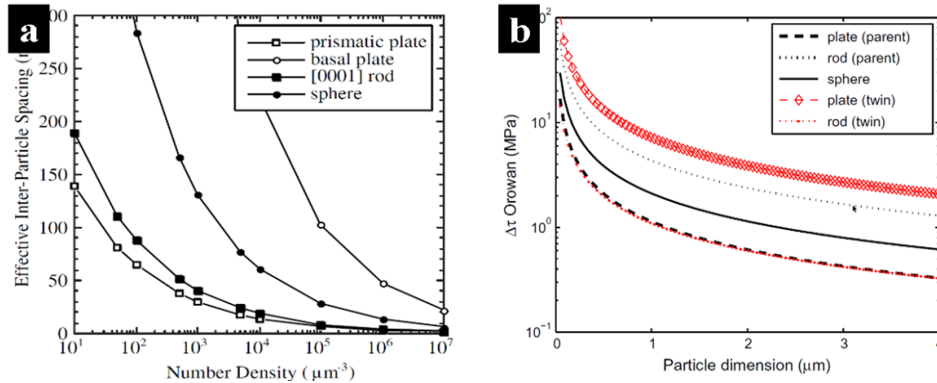


Figure 5.18 (a) Effective inter-particle spacing and (b) Orowan stress of various precipitate morphologies [130, 214-219]

Effective inter-particle spacing (λ) and mean planar diameter (d_p) also play a major role in enhancing dispersion strengthening in these alloys. Although the precipitate

number density per unit area of slip plane of matrix phase can be increased much more effectively by $[0001]_{\alpha}$ rods, prismatic plates are much more efficient in reducing the inter-particle spacing (see fig. 5.18a) [130, 214-219].

However, in the case of twinning, due to lattice rotation, basal plates can become effective barriers for preventing basal slip in a twinned material. In contrast, the c-axis rods fail in preventing basal slip in a twinned material as they lie in the basal plane and are poorly oriented to intersect the basal slip planes. Also, the c-axis rods are predicted to increase asymmetry. In the case of the A9 alloys rolled at 200°C, deformation twinning was observed as a major deformation mode. So, plastic relaxation of the stress concentration (cracks/voids formed or flow localization in the vicinity of the twin boundaries or tips) is limited. Although $[0001]_{\alpha}$ rods being an effective strengthening mechanism (figure 5.18b) against basal slip were present, lack of plastic relaxation mechanisms caused early failure in the materials[220].

In the case of A9 samples rolled at 250°C and 300°C, absence of twinning, the activation of pyramidal $\langle c+a \rangle$ slip, increase in the mean diameter of particles, and reduction in the effective inter-particle distance played a crucial part in relatively improving the strength of the materials which will be discussed in the upcoming section. This is similar to the mechanisms observed in case of A6 alloys where inter-particle distance was still effective enough to provide better mechanical behavior in terms of both strength and ductility with confined rolling helping randomize texture to a certain extent.

5.5 Mechanical properties under compression

5.5.1 Stress- strain behavior at different strain rates under compression

Quasi-static ($1 \times 10^{-3} \text{ s}^{-1}$) and high strain rate ($1 \times 10^3 \text{ s}^{-1}$) experiments were performed in compression using an INSTRON model 5582 Universal testing machine and a conventional Kolsky Bar, or Split Hopkinson Pressure Bar (SHPB), respectively. As seen in fig. 5.19, at quasi-static rates, the strain hardening rate varied with temperature with samples rolled at 250°C exhibiting the highest value among others. The sigmoidal shape of the quasi-static compression curves (fig. 5.19 (a)) indicates profuse twinning in this material. Although it was observed that the samples rolled at 200°C had extensive twinning, the stress-strains curves at quasi-static rates didn't possess sigmoidal shape probably due to recrystallization of grains inside twins during the testing process. This reasoning can be extended to the behavior of this material at higher strain rates as well. The presence of double twins has been correlated to void and crack formation along with flow localization in the vicinity of the boundaries due to the unavailability of plastic deformation mechanisms to relieve stress concentrations [19, 221, 222].

The presence of double twins in samples rolled at 200°C might be a reason for their relatively lower strength and ductility. Samples rolled at 300°C showed the highest compressive strength although samples rolled at 250°C came to a close second in comparison to the other samples. Although, ductility was roughly halved, relative increase in compressive strength (as compared to the solutionized baseline material) was lesser (~35-40%). The reason for change in yield strength of materials rolled at 200°C and 300°C could be perhaps attributed to the change in texture and

splitting of basal poles due to confined rolling. The hypothesis is, at the rolling temperature of 300°C, the volume fraction of fine precipitates would be comparatively less due to the depleted solute content. Hence, until a certain strain level was reached, there was no contribution from these precipitates toward hardening. On the other hand, fine precipitates present in the samples rolled at lower temperatures might have influenced the onset of yield.

In contrast, at dynamic loading conditions, the same alloys exhibit higher strength and malleability as the rolling temperature increased. All the samples exhibited extensive work hardening, especially the samples rolled at 250°C and strain rate hardening i.e., the strength increased with strain rate. Zener pinning effect imposed by the nanometer-sized continuous precipitates could be a reason for such a behavior. Sigmoidal curve still persists at 250°C indicating twin based recrystallization mechanisms do not work much in this temperature range. Perhaps, the orientation of twins might have not been favorable for recrystallization.

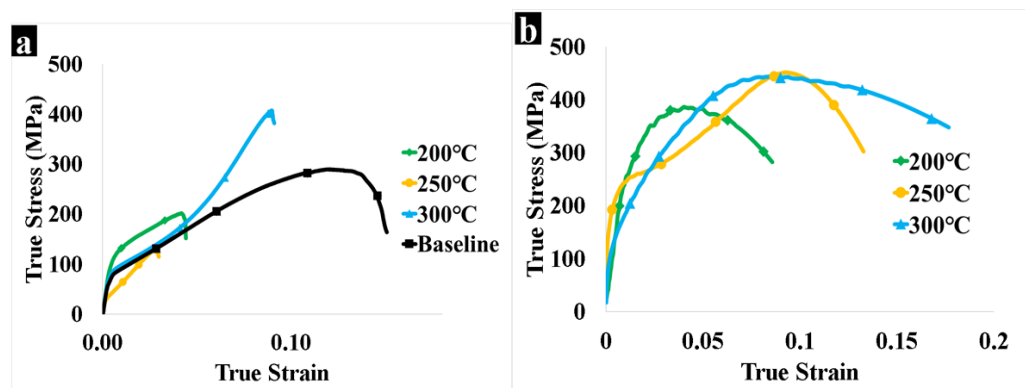


Figure 5.19: (a) Quasi-static and (b) dynamic compressive behavior of A9 alloys rolled at different temperatures along ND

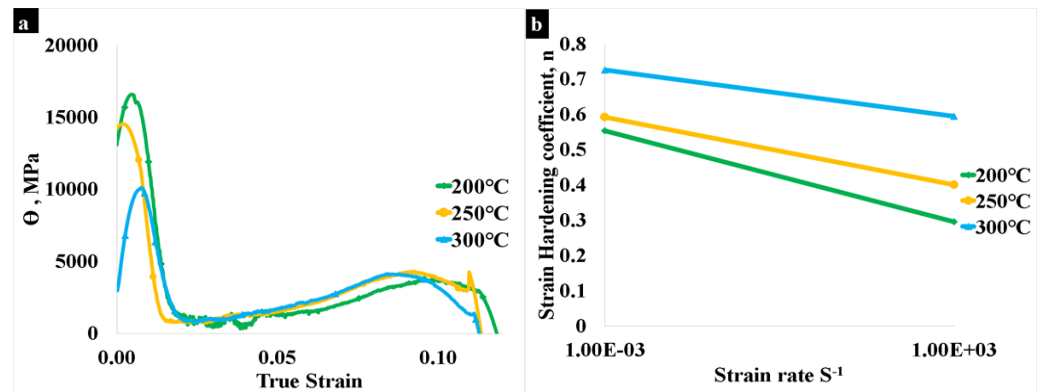
The observed flow stresses at dynamic strain rates were higher in comparison to quasi-static rates hence signifying that the alloys at those temperatures could be strain rate sensitive. In comparison to conventional severe plastic deformation

methods, the compressive properties of these confined rolled alloys in both the strain rates were far superior to AZ31B with similar range of grain sizes produced through conventional rolling and ECAP [223, 224] hence proving confined rolling serves as an advantage to them both in terms of mechanical properties and texture. AZ31B and A6 alloys failed at higher strain levels in comparison to A9 alloys at quasi-static strain rates. The driving force for Zener pinning and recrystallization was balanced in case of alloys with lower Al content and precipitation in general. But in the case of A9, Zener pinning and solute drag was very extensive thereby reducing the driving force for recrystallization and hence, failing at lower strains due to reduced scope for plastic deformation.

5.5.2 Strain hardening rate and coefficient

It can be observed from fig. 5.20(a), that the initial hardening stage (Stage III hardening) for all the three samples with respect to the strain hardening rate was the same. However, the difference lies in the Stage IV hardening which was attributed to slip assisted deformation. Samples rolled at 200°C and 250°C did not harden as true strain increased but samples rolled at 300 did. There was rapid drop in hardening and then increase in hardening with samples rolled at 300°C due to the larger size of precipitates observed from the microstructures at the later stage of deformation. Although the presence of high-volume fraction of precipitates and rod morphology of precipitates can be effective against dislocation movement, reduction in Orowan stress to cut/bow finer precipitates at higher stress might be a reason for not blocking dislocation motion effectively and lowered hardening.

Higher the magnitude of strain hardening exponent, greater is the strain hardening for a given amount of plastic strain. From fig. 5.20 (b), it was observed that the strain hardening coefficient reduced as strain rate increased and the samples rolled at 200°C exhibited increase slope of the strain hardening coefficient curve. With increase in addition of Al content to Mg, shift in recrystallization temperatures have been observed. Perhaps, for this alloy the starting point for intense grain deformation leading to recrystallization occurs at 300°C (recall for AZ31B and A6 alloys, it is 150°C and 250°C respectively) and hence the value of strain hardening



coefficient is also higher.

Figure 5.20: (a) Strain hardening rate and (b) Strain hardening coefficient of A9 alloy along ND.

5.5.3 Strain rate sensitivity (SRS)

The SRS can be described as the change in flow stress corresponding to increasing strain rates defined by $\frac{d \ln \sigma}{d \ln \dot{\epsilon}}$ where σ is the flow stress and $\dot{\epsilon}$ is the strain rate.

Generally, the strength of the materials should increase with strain rate since the high strain rate limits the time required for plastic deformation and the deformation resistance force generated in the material cannot be reduced [167]. The value of SRS showed a decreasing trend until 250°C after which it started to increase. The

increase or decrease in these values could be attributed to various factors like change in deformation mechanism, grain size (DRX), volume fraction of precipitates etc. [225]. On one hand, at quasi-static strain rates, deformation is controlled by thermal activation and the strength of the material increases slowly with increase in strain rate. On the other hand, at dynamic strain rates, dislocation drag mechanism takes the front stage and relationship between strength and strain rate becomes linear.

At 200°C, the given strain rate sensitivity value ranges between 0.025-0.035 which confirms the contribution of basal slip being a dominant deformation mechanism. In fact, the strain rate sensitivity is zero up to ~2% strain which could be attributed to the occurrence of twinning during the early stages of plastic deformation (fig. 5.21) The presence of mechanical twins can be observed from the graphical representation of the average misorientation shown in fig. 5.5.

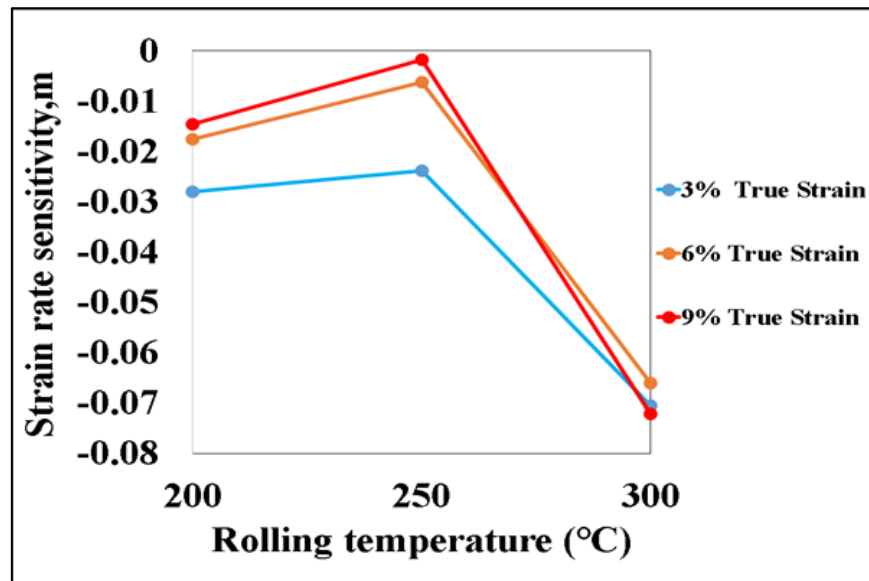
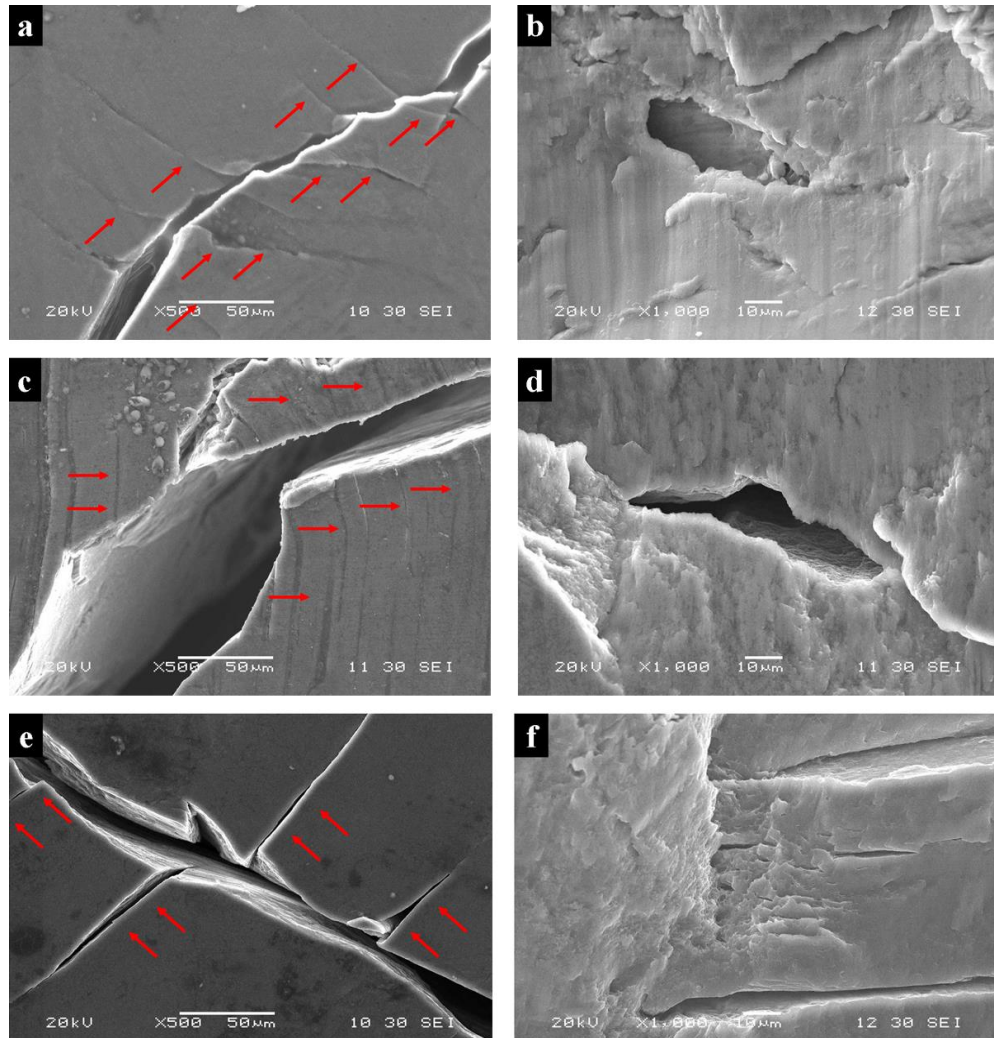


Figure 5.21: Strain rate sensitivity (SRS) of A9 alloy along ND.

The higher values of strain rate sensitivity at lower strains for samples rolled at 300°C is due to the activation of non-basal slip systems, primarily pyramidal II cross-slip (since basal slip and deformation twinning exhibit low and almost rate-insensitive behavior) [171, 193]. But the lower value of SRS at higher (9%) strain is due to the reduction in propensity of grain boundary sliding (GBS) due to grain



size effect and significant dynamic grain growth caused by reduction of interfacial energy at 300°C.

Figure 5.22: Fracture surface SEM macro (a,b,d) and micrographs (c,e) of A9 alloys confined rolled at 200°C, 250°C and 300°C respectively after quasi-static compression along ND

The reason for the almost strain rate insensitivity at 250°C still needs to be understood perhaps, the competing factors such as smaller grain size and the transition between twin-dominated flow at lower temperatures to non-basal slip based flow at higher temperatures might be considered as a reason [170, 171, 193]

5.5.4 Fracture surface analysis under quasi-static compression:

Figure 5.22 depicts both the macroscopic and microstructural perspective of the fracture surfaces in A9 alloys. The samples tested under dynamic compression were crushed into tiny pieces and hence, could not be recovered for fracture surface analysis. These samples, similar to A6 and AZ31B underwent shear failure with fracture lines running across the sample oriented at 45° with reference to the orientation during loading. A similar observation of localized shear flow on both sides of the shear band due to the presence of a strain gradient across the fracture line was observed in this case too (marked by red arrows). Actual fracture surface included sheet like micro-facets especially at 200°C and 250°C almost like a brittle fracture.

This might be due to excessive precipitation (Orowan stress might be lower for fine precipitation) and unavailability of non-basal slip systems at lower temperatures. The observation of tearing regions was in line with that of A6 and AZ31B alloys. As temperature increased, the microstructure hosted shallow dimples showing evidence for ductile fracture at higher temperatures. An interesting observation that set apart A9 alloys from others was the presence of voids/fissures in fracture surface of samples rolled at lower temperatures apparently looking like precipitates were

chipped off from the structure reiterating the fact that precipitates were not effective in resisting dislocation motion.

5.6 Chapter summary

Adding 9 wt.%Al to Mg definitely had an influence on the microstructure, deformation mechanisms and ultimately affected the mechanical properties. The microstructure was not recrystallized and remained coarse grained at all the rolling temperatures studied. There were traces of dynamic recrystallization observed especially inside the twins. However, recrystallization was incomplete in this alloy, unlike AZ31B and A6 which recrystallized to near completion at 200°C and 300°C respectively. Increase in wt.% Al pushed the recrystallization to higher temperatures. Confined rolling was successful in this case to randomize texture in comparison to other alloys. The competition between Zener pinning/solute drag and recrystallization mechanisms turned into a conflict in this case and precipitates were aggressive in pinning the grain boundaries thereby not allowing its movement and hence affecting recrystallization. In terms of precipitation, both continuous and discontinuous precipitates were observed with coarse precipitation along grain boundaries and nano-sized precipitates inside the grains. The decreased interparticle spacing increased the Orowan stress value thereby increasing its strength at the cost of ductility which could be seen through quasi-static compression stress-strain curves. The material exhibited strain rate hardening and the work hardening rate was higher for samples rolled at lower temperatures. Fracture surface analysis showed shear localization and evidence of particles being

peeled/chipped off of the material during testing. Samples rolled at higher temperature showed evidence of ductile fracture by means of shallow dimples.

CHAPTER 6: SUMMARY AND CONCLUDING REMARKS

The last three chapters elaborately discussed three Mg alloys, namely AZ31B (a commercial alloy with composition: Al~3%, Zn~1%, Mn/Si/Cu/Ca/Fe/Ni -traces, Mg- remaining) and two binary alloys Mg-6%Al (A6) and Mg-9%Al (A9). These alloys were holistically studied for the effect of thermo-mechanical processing/severe plastic deformation i.e., confined rolling and change in composition i.e., in terms of %Al. It is easier to compare the commercial alloy, AZ31B with A6 and A9 since no new phases will be formed if Al: Zn ratio exceeds by 3:1. These alloys were fabricated and confined rolled after which they were characterized for microstructure (dynamic recrystallization, effect of microstructural features such as size, volume fraction, distribution, morphology, location of twins, precipitates)/ texture using optical microscopy, SEM (EBSD) and TEM and tested for mechanical behavior under compression at quasi-static and dynamic loading rates.

Aluminum is the most widely used alloying element of magnesium alloys for its use in structural applications. Zheng et.al [225] correlated the effect of addition of Al from 1% to 9% to grain size reduction from 3097 μ m to 111 μ m and increase in hardness from 36.3HV to 50.1HV while attributing it to the solution strengthening by Al solubilized in the α -Mg matrix. In the present work, the average grain size of AZ31B, A6 and A9 are summarized in table 6.1 below:

Table 6.1 Comparison of average grain size of AZ31B, A6 and A9 alloys

Rolling temperature (°C)	AZ31B	A6	A9
200	$5.3 \pm 4.7 \mu\text{m}$	$31 \pm 5.2 \mu\text{m}$	$15.65 \pm 8.2 \mu\text{m}$
250	$9.6 \pm 7.4 \mu\text{m}$	$9.4 \pm 3.8 \mu\text{m}$	$7.9 \pm 3.5 \mu\text{m}$
300	$20.7 \pm 7.1 \mu\text{m}$	$19 \pm 6.5 \mu\text{m}$	$16.5 \pm 8.5 \mu\text{m}$

AZ31B showed signs of recrystallization at a lower temperature approximately between 150°C and 200°C whereas A6 and A9 started showing recrystallization only at 200°C. A6 showed complete recrystallization between 250°C and 300°C whereas A9 didn't show signs of complete recrystallization at any rolling temperature. The numbers provided in the table for A9 alloys were slightly deceptive since optical microscopy didn't show such a refined microstructure. Hence, multiple EBSD images must be mapped together, and then statistical correlation needs to be done especially for A9 alloys

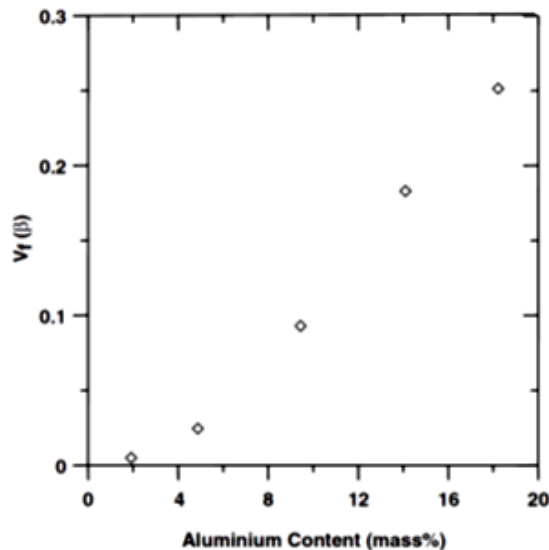


Figure 6.1 Volume fraction of β - $Mg_{17}Al_{12}$ precipitates with varying Al contents in Mg-Al alloys using NMR spectroscopy [226]

. The reason for A9 not getting completely recrystallized was attributed to the competition between particle stimulated nucleation and solute drag by Zener pinning mechanism. Also, high volume fraction (precipitates occupy ~10 vol% of the microstructure as per fig. 6.1 [226]) and dispersion of precipitates placed the alloy in such a regime where Zener pinning was enough to suppress recrystallization and particles stabilized the deformation microstructures.

Comparison of average recrystallized grain sizes based on the GOS criteria indicate the early recrystallization process of AZ31B in comparison to the binary alloys as shown in table 6.2.

Table 6.2 Comparison of average recrystallized grain size of AZ31B, A6 and A9 alloys

Rolling temperature (°C)	AZ31B	A6	A9
200	3.69 μm	11.92 μm	8.31 μm
250	7.62 μm	6.97 μm	8.33 μm
300	15.11 μm	13.06 μm	12.41 μm

Grain boundary character distribution (GBCD) of these alloys suggested that the higher amount of LAGBs (misorientation angle $<15^\circ$) was found in samples rolled at 150°C, 200°C/250°C and 250°C/300°C for AZ31B, A6 and A9 respectively. Kernel average misorientation (KAM) values also indicated an increase in strain for samples rolled below 250°C indicating the amount of stored energy available for recrystallization. The above observations confirm the interpretation of approximate recrystallization completion temperature (except A9 alloys) and evolution of recrystallized microstructure.

Table 6.3 Comparison of texture intensity of AZ31B, A6 and A9 alloys

Rolling temperature (°C)	AZ31B	A6	A9
200	15.70	42.65	23.13
250	17.44	15.21	31.28
300	33.95	18.01	29.74

Comparative textural intensity of the alloys represented in table 6.3 suggested strong basal texture i.e., c-axis is parallel to ND in all the alloys especially AZ31B. However, the textural intensity was reduced in samples where higher recrystallized fraction was observed. As per this observation, texture intensity was the lowest at 200°C and 250°C for AZ31B and A6 alloys with textural intensity for A9 alloys almost same for all temperatures indicating the incompleteness of recrystallization process in these alloys.

Average misorientation of AZ31B and A9 indicated the presence of extension $86 \pm 5^\circ$ tensile twins (TTWs) $\{10\bar{1}2\} < 10\bar{1}1 >$ in the microstructure at lower rolling temperatures of 150°C and 200°C respectively. As rolling temperature increased, 30° [0001] grain boundaries indicative of dynamic recrystallization were progressively seen to increase along with decrease in extension twins. However, in case of A6, it was hypothesized that all or most of the twins might have recrystallized at lower temperatures due to the presence of optimal volume fraction of precipitation for PSN inside twins.

Schmid factor analysis for AZ31B suggested that the persistence of basal slip as a predominant slip system but in the case of A6 and A9, invocation of non-basal slip systems especially pyramidal $<c+a>$ slip systems was observed. In A6, compatibility stress at grain boundaries which sweeps the entire volume due to finer grain size and in A9, thermally activated dislocation glide was attributed as reasons for increased activity of non-basal slip systems respectively. With respect to

dynamic recrystallization mechanism, AZ31B showed consistent discontinuous dynamic recrystallization (DDRX) at all rolling temperatures whereas for A6, transition from continuous dynamic recrystallization (CDRX) to DDRX was observed at higher temperatures (300°C). Interestingly, in A9, CDRX was the prominent mechanism at all rolling temperatures.

Due to less volume fraction of β -Mg₁₇Al₁₂ precipitates available in AZ31B, a lot of information on precipitation was not available in EBSD studies. For A6, continuous precipitation appeared to be predominant for samples rolled at 200°C and 300°C and for samples rolled at 250°C, continuous and discontinuous precipitation seemed to co-exist. For A9, proportion of continuous precipitates was higher at 200°C and equal proportion of both kinds of precipitation at 250°C and 300°C. Evidence for particle stimulated nucleation (PSN) and Zener pinning (solute drag) were observed in both A6 and A9 alloys. In case of A6 alloys, outstanding grain refinement was observed due to the right balance between pinning pressure from coarse particles which mitigated grain growth by slowing grain boundary migration and nano-sized precipitates acting as nucleation sites for recrystallization. However, in case of A9 alloys, although PSN was observed, particle dispersion and higher volume fraction of precipitates maximized pinning pressure thereby minimizing grain boundary movement and reduced the availability of nucleation sites suppressing recrystallization. Hence, the deformed structure was not completely recrystallized.

Precipitate morphology for A9 varied from predominance of c-axis rods and spherical particles for samples rolled at 200°C and 300°C respectively with equal

availability of both precipitate shapes for samples rolled at 250°C. In A6, all the samples had a mixture of both spherical and ellipsoidal particles at all rolling temperatures. The presence of higher volume fraction ellipsoidal particles at 250°C was attributed as a reason for exceptional drag force exerted in turn refining the grain size of these alloys.

Quasi-static and dynamic compression experiments (different strain rates) were performed on these alloys. All the alloys showed increase in compressive strength in comparison to baseline alloys after confined rolling at quasi-static rates. While A6 and A9 showed exceptional strain rate hardening i.e., increase in compressive strength with increase in strain rate, AZ31B showed no or reverse effect due to change in strain rate. The compressive properties of both A6 and A9 are superior in comparison to AZ31B with A6 showing best mechanical properties during high strain rate compression probably due to the ideal volume fraction of precipitates and small grain size achieved due to dynamic recrystallization. Ductility of A9 alloys were inferior compared to other alloys and same observations were obtained in the literature [227] as shown in the figure below.

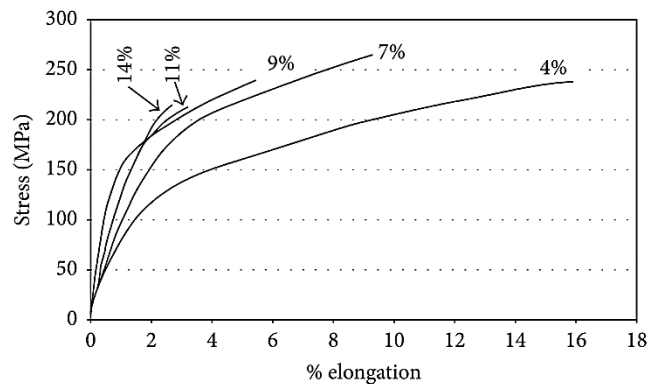


Figure 6.2 Typical stress-strain behavior of Mg-Al alloys as a function of % Al[226].

A comparison of compressive behavior of AZ alloys with different %Al as available in literature versus current work given by figure 6.3 show similar trend of decreasing ductility and increasing compressive strength with increase in %Al.

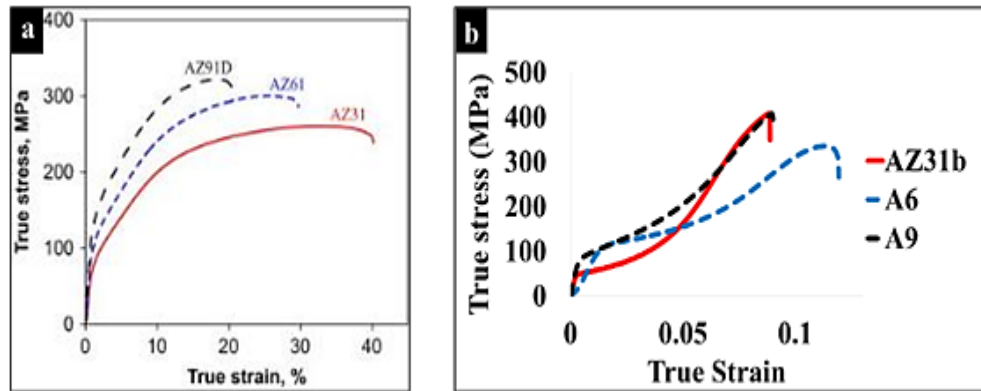


Figure 6.3 Typical compressive stress-strain curves of Magnesium alloys varying %Al observed in (a) literature [198] versus (b) current work at quasi-static strain rates.

Strain hardening rate of AZ31B, A6 and A9 alloys rolled at 150°C, 200°C and 250°C respectively was also examined. In AZ31B, presence of extension twins contributed to strain hardening through texture hardening while in A6 and A9, presence of higher volume fraction of precipitates and rod-shaped precipitation as effective barriers for dislocation motion was pointed out as a reason for their better strain hardening response. In all the three alloys, strain hardening coefficient reduced with increase in strain rate. Strain rate sensitivity (SRS) of alloys was the lowest in the temperatures where completion of dynamic recrystallization occurred except A9 where dynamic recrystallization never occurred for the complete microstructure.

In summary, all the three alloys showed good response to thermo-mechanical processing/severe plastic deformation and improved in compressive

strength both in quasi-static and dynamic strain rate regime. Texture randomization was slightly achieved in the alloys due to the effect of confined rolling in case of A6 and A9 alloys. While AZ31B and A6 showed exceptional grain refinement due to the presence of optimal amount of precipitation, presence of necessary stored energy and right balance between the Zener pinning pressure (solute drag) and particle stimulated nucleation (PSN), A9 didn't undergo complete recrystallization due to the solute drag pressure of deformed grains remarkably exceeding the driving force for nucleation. AZ31B at 175°C and A6 at 250°C proved to be the best composition-processing combination for obtaining the optimal strength and ductility and slight randomization in texture aided by almost complete deformation assisted dynamic recrystallization.

CHAPTER 7 FUTURE WORK

In this thesis, the structure-property relationship of Mg-Al based alloys was analyzed in detail using advanced microscopic techniques such as SEM-EBSD/TEM and mechanical testing under quasi-static and dynamic compression. A fundamental understanding about complex deformation and dynamic recrystallization mechanisms due to the combined effect of addition of Al to Mg matrix and confined rolling was developed. However, some questions still need answering and the following aspects need to be analyzed for a thorough understanding of these alloys.

1. An elaborate transmission electron microscopy (TEM) study on the rolled specimens in terms of twin-precipitate interaction, twin DRX, precipitation-dislocation interaction, precipitation-matrix coherency and orientation relationship, precipitate morphology etc. needs to be done.
2. Finite element analysis (FEA) based modelling study should be done to analyze the stress states developed during confined rolling in comparison to conventional rolling.
3. Hot compression studies of solutionized alloys for studying starting temperatures for dynamic recrystallization at rolling strain rates to fix the temperature of rolling operation needs to be done.

References

1. Neelameggham, R., 1 - Primary production of magnesium, in *Fundamentals of Magnesium Alloy Metallurgy*, M.O. Pekguleryuz, K.U. Kainer, and A. Arslan Kaya, Editors. 2013, Woodhead Publishing. p. 1-32.
2. Kaya, A.A., 2 - Physical metallurgy of magnesium, in *Fundamentals of Magnesium Alloy Metallurgy*, M.O. Pekguleryuz, K.U. Kainer, and A. Arslan Kaya, Editors. 2013, Woodhead Publishing. p. 33-84.
3. Alaneme, K.K. and E.A. Okotete, Enhancing plastic deformability of Mg and its alloys-A review of traditional and nascent developments. *Journal of Magnesium and Alloys*, 2017. **5**(4): p. 460-475.
4. Akhtar, A. and E. Teghtsoonian, SOLID SOLUTION STRENGTHENING OF MAGNESIUM SINGLE CRYSTALS .I. ALLOYING BEHAVIOUR IN BASAL SLIP. *Acta Metallurgica*, 1969. **17**(11): p. 1339-+.
5. Akhtar, A. and E. Teghtsoonian, SOLID SOLUTION STRENGTHENING OF MAGNESIUM SINGLE CRYSTALS .2. EFFECT OF SOLUTE ON EASE OF PRISMATIC SLIP. *Acta Metallurgica*, 1969. **17**(11): p. 1351-+.
6. Agnew, S.R., et al., Enhanced ductility in strongly textured magnesium produced by equal channel angular processing. *Scripta Materialia*, 2004. **50**(3): p. 377-381.
7. Mukai, T., et al., Ductility enhancement in AZ31 magnesium alloy by controlling its grain structure. *Scripta Materialia*, 2001. **45**(1): p. 89-94.

8. Mukai, T., M. Yamanoi, and K. Higashi, Processing of Ductile Magnesium Alloy under Dynamic Tensile Loading. *MATERIALS TRANSACTIONS*, 2001. **42**(12): p. 2652-2654.
9. Kim, W.J., et al., Mechanical properties and microstructures of an AZ61 Mg Alloy produced by equal channel angular pressing. *Scripta Materialia*, 2002. **47**(1): p. 39-44.
10. Fan, H. and J.A.J.J.o.A.M. El-Awady, Molecular dynamics simulations of orientation effects during tension, compression, and bending deformations of magnesium nanocrystals. 2015. **82**(10): p. 101006.
11. Wang, X., et al., Deformation of twins in a magnesium alloy under tension at room temperature. *Journal of Alloys and Compounds*, 2014. **594**: p. 44-47.
12. Jordon, J.B., et al., Effect of twinning, slip, and inclusions on the fatigue anisotropy of extrusion-textured AZ61 magnesium alloy. *Materials Science and Engineering a-Structural Materials Properties Microstructure and Processing*, 2011. **528**(22-23): p. 6860-6871.
13. Song, B., et al., Improvement of formability and mechanical properties of magnesium alloys via pre-twinning: A review. *Materials & Design*, 2014. **62**: p. 352-360.
14. Lou, X., et al., Hardening evolution of AZ31B Mg sheet. 2007. **23**(1): p. 44-86.
15. Yang, Z., et al., Review on Research and Development of Magnesium Alloys. *Acta Metallurgica Sinica (English Letters)*, 2008. **21**(5): p. 313-328.
16. Bohlen, J., D. Letzig, and K.U. Kainer, New Perspectives for Wrought Magnesium Alloys. *Materials Science Forum*, 2007. **546-549**: p. 1-10.

17. Yoshinaga, H. and R. Horiuchi, On the Nonbasal Slip in Magnesium Crystals. Transactions of the Japan Institute of Metals, 1964. **5**(1): p. 14-21.
18. Kelley, E.W. and W.F. Hosford, PLANE-STRAIN COMPRESSION OF MAGNESIUM AND MAGNESIUM ALLOY CRYSTALS. Transactions of the Metallurgical Society of Aime, 1968. **242**(1): p. 5-&.
19. Wonsiewicz, B.C. and W.A. Backofen, PLASTICITY OF MAGNESIUM CRYSTALS. Transactions of the Metallurgical Society of Aime, 1967. **239**(9): p. 1422-+.
20. Yoshinaga, H. and R. Horiuchi, Deformation Mechanisms in Magnesium Single Crystals Compressed in the Direction Parallel to Hexagonal Axis. Transactions of the Japan Institute of Metals, 1963. **4**(1): p. 1-8.
21. Chapuis, A. and J.H. Driver, Temperature dependency of slip and twinning in plane strain compressed magnesium single crystals. Acta Materialia, 2011. **59**(5): p. 1986-1994.
22. Obara, T., H. Yoshinga, and S. Morozumi, $\{11\bar{2}2\}$ $\langle 1123 \rangle$ Slip system in magnesium. Acta Metallurgica, 1973. **21**(7): p. 845-853.
23. Li, X., et al., Orientational analysis of static recrystallization at compression twins in a magnesium alloy AZ31. 2009. **517**(1-2): p. 160-169.
24. Mishra, R.K., et al., Influence of cerium on the texture and ductility of magnesium extrusions. Scripta Materialia, 2008. **59**(5): p. 562-565.
25. Reed-Hill, R.E. and W.D. Robertson, The crystallographic characteristics of fracture in magnesium single crystals. Acta Metallurgica, 1957. **5**(12): p. 728-737.

26. Koike, J., et al., The activity of non-basal slip systems and dynamic recovery at room temperature in fine-grained AZ31B magnesium alloys. *Acta Materialia*, 2003. **51**(7): p. 2055-2065.
27. Langelier, B. and S. Esmaeili, Effects of Ce additions on the age hardening response of Mg–Zn alloys. *Materials Characterization*, 2015. **101**: p. 1-8.
28. Stanford, N., et al., Effect of microalloying with rare-earth elements on the texture of extruded magnesium-based alloys. *Scripta Materialia*, 2008. **59**(7): p. 772-775.
29. Hirsch, J. and T. Al-Samman, Superior light metals by texture engineering: Optimized aluminum and magnesium alloys for automotive applications. *Acta Materialia*, 2013. **61**(3): p. 818-843.
30. Tahreen, N., et al., Influence of aluminum content on twinning and texture development of cast Mg–Al–Zn alloy during compression. *Journal of Alloys and Compounds*, 2015. **623**: p. 15-23.
31. Huang, X., et al., Influence of aluminum content on the texture and sheet formability of AM series magnesium alloys. *Materials Science and Engineering: A*, 2015. **633**: p. 144-153.
32. Luo, A.A., C. Zhang, and A.K. Sachdev, Effect of eutectic temperature on the extrudability of magnesium–aluminum alloys. *Scripta Materialia*, 2012. **66**(7): p. 491-494.
33. Zhao, X., et al., An investigation on microstructure, texture and mechanical properties of AZ80 Mg alloy processed by annular channel angular extrusion. 2019. **12**(6): p. 1001.

34. Narukawa, Y., et al., Effect of Zn Contents on Microstructure in AZ-Series Magnesium Alloys. *Advanced Materials Research*, 2012. **409**: p. 358-361.
35. Yu, Z.H., et al., Effect of Zn content on the microstructures and mechanical properties of laser beam-welded ZK series magnesium alloys. *Journal of Materials Science*, 2010. **45**(14): p. 3797-3803.
36. Huang, X., et al., Texture and stretch formability of AZ61 and AM60 magnesium alloy sheets processed by high-temperature rolling. *Journal of Alloys and Compounds*, 2015. **632**: p. 94-102.
37. Wang, M., H. Zhou, and L. Wang, Effect of Yttrium and Cerium Addition on Microstructure and Mechanical Properties of AM50 Magnesium Alloy. *Journal of Rare Earths*, 2007. **25**(2): p. 233-237.
38. Li, J., et al., Mechanical properties and failure of ECAE processed Mg₉₇Y₂Zn₁ at different strain rates. *Materials Science and Engineering: A*, 2019. **762**: p. 138094.
39. Li, Y., et al., Microstructural evolution and mechanical properties of Mg₅Y-5Gd x Nd_{0.5}Zr magnesium alloys at different states. *Rare Metals*, 2010. **29**: p. 317-322.
40. Shen, J., et al., Mechanical Properties of Mg Alloys AMX602 and AZXE7111 under Quasi-Static and Dynamic Loading, in *Magnesium Technology 2012*. 2012, Springer. p. 371-375.
41. Shen, J., et al., Mechanical behavior of a lanthanum-doped magnesium alloy at different strain rates. *Materials Science and Engineering: A*, 2015. **626**: p. 108-121.

42. Song, G.S., M. Staiger, and M. Kral, Enhancement of the properties of Mg-Li alloys by small alloying additions. *Magnesium Technology 2003*, ed. H.I. Kaplan. 2003, Warrendale: Minerals, Metals & Materials Soc. 77-79.
43. Drozd, Z., Z. Trojanová, and S. Kúdela, Deformation behaviour of Mg-Li-Al alloys. *Journal of Alloys and Compounds*, 2004. **378**(1): p. 192-195.
44. Zou, Y., et al., Texture evolution and their effects on the mechanical properties of duplex Mg-Li alloy. *Journal of Alloys and Compounds*, 2016. **669**: p. 72-78.
45. Wu, R., Z. Qu, and M.L. Zhang. REVIEWS ON THE INFLUENCES OF ALLOYING ELEMENTS ON THE MICROSTRUCTURE AND MECHANICAL PROPERTIES OF Mg-Li BASE ALLOYS. 2010.
46. Valiev, R.Z., et al., Producing bulk ultrafine-grained materials by severe plastic deformation. *JOM*, 2006. **58**(4): p. 33-39.
47. Bridgman, P.W., On Torsion Combined with Compression. *Journal of Applied Physics*, 1943. **14**(6): p. 273-283.
48. Bridgman, P.W., The Effect of Hydrostatic Pressure on Plastic Flow under Shearing Stress. *Journal of Applied Physics*, 1946. **17**(8): p. 692-698.
49. Agnew, S.R., et al., Texture evolution of five wrought magnesium alloys during route A equal channel angular extrusion: Experiments and simulations. *Acta Materialia*, 2005. **53**(11): p. 3135-3146.
50. Zuberova, Z., I. Sabirov, and Y. Estrin, The effect of deformation processing on tensile ductility of magnesium alloy AZ31. *Kovove Materialy-Metallic Materials*, 2011. **49**(1): p. 29-36.

51. Valiev, R., Nanostructuring of metals by severe plastic deformation for advanced properties. *Nature Materials*, 2004. **3**(8): p. 511-516.
52. Ding, S.X., et al., Improvement of strength of magnesium alloy processed by equal channel angular extrusion. *Scripta Materialia*, 2008. **59**(9): p. 1006-1009.
53. Lapovok, R., et al., The effect of warm equal channel angular extrusion on ductility and twinning in magnesium alloy ZK60. 2004. **45**(7): p. 2192-2199.
54. Lapovok, R., et al., Enhanced Superplasticity in a Magnesium Alloy Processed by Equal-Channel Angular Pressing with a Back-Pressure. 2008. **10**(5): p. 429-433.
55. Figueiredo, R.B. and T.G. Langdon, Record Superplastic Ductility in a Magnesium Alloy Processed by Equal-Channel Angular Pressing. 2008. **10**(1-2): p. 37-40.
56. Figueiredo, R.B. and T.G. Langdon, Principles of grain refinement and superplastic flow in magnesium alloys processed by ECAP. *Materials Science and Engineering: A*, 2009. **501**(1): p. 105-114.
57. Orlov, D., et al., Improvement of mechanical properties of magnesium alloy ZK60 by integrated extrusion and equal channel angular pressing. *Acta Materialia*, 2011. **59**(1): p. 375-385.
58. Malheiros, L.R.C., R.B. Figueiredo, and T. Langdon, Processing Different Magnesium Alloys through HPT. *Materials Science Forum*, 2014. **783-786**: p. 2617-2622.

59. Edalati, K., et al., High-pressure torsion of pure magnesium: Evolution of mechanical properties, microstructures and hydrogen storage capacity with equivalent strain. *Scripta Materialia*, 2011. **64**(9): p. 880-883.
60. Kai, M., Z. Horita, and T.G. Langdon, Developing grain refinement and superplasticity in a magnesium alloy processed by high-pressure torsion. *Materials Science and Engineering: A*, 2008. **488**(1): p. 117-124.
61. Agnew, S.R. and Ö. Duygulu, Plastic anisotropy and the role of non-basal slip in magnesium alloy AZ31B. *International Journal of Plasticity*, 2005. **21**(6): p. 1161-1193.
62. Ulacia, I., et al., Mechanical behavior and microstructural evolution of a Mg AZ31 sheet at dynamic strain rates. *Acta Materialia*, 2010. **58**(8): p. 2988-2998.
63. Al-Samman, T., X. Li, and S.G. Chowdhury, Orientation dependent slip and twinning during compression and tension of strongly textured magnesium AZ31 alloy. *Materials Science and Engineering: A*, 2010. **527**(15): p. 3450-3463.
64. Yi, S., et al., Mechanical anisotropy and deep drawing behaviour of AZ31 and ZE10 magnesium alloy sheets. *Acta Materialia*, 2010. **58**(2): p. 592-605.
65. Zarandi, F., et al., Effect of Al and Mn additions on rolling and deformation behavior of AZ series magnesium alloys. *Materials Science and Engineering: A*, 2008. **496**(1): p. 159-168.
66. Eddahbi, M., et al., Comparison of the microstructure and thermal stability of an AZ31 alloy processed by ECAP and large strain hot rolling. *Materials Science and Engineering: A*, 2005. **410-411**: p. 308-311.

67. del Valle, J.A., M.T. Pérez-Prado, and O.A. Ruano, Texture evolution during large-strain hot rolling of the Mg AZ61 alloy. *Materials Science and Engineering: A*, 2003. **355**(1): p. 68-78.
68. Alili, B., et al., Texture evolution in AZ91 alloy after hot rolling and annealing. *Transactions of Nonferrous Metals Society of China*, 2013. **23**(8): p. 2215-2221.
69. Jin, Z.-Z., et al., Effects of Mg₁₇Al₁₂ second phase particles on twinning-induced recrystallization behavior in Mg–Al–Zn alloys during gradient hot rolling. *Journal of Materials Science & Technology*, 2019. **35**(9): p. 2017-2026.
70. Wang, M., et al., Effect of initial texture on dynamic recrystallization of AZ31 Mg alloy during hot rolling. 2011. **528**(6): p. 2941-2951.
71. Beausir, B., et al., Analysis of microstructure and texture evolution in pure magnesium during symmetric and asymmetric rolling. *Acta Materialia*, 2009. **57**(17): p. 5061-5077.
72. Biswas, S., D.-I. Kim, and S. Suwas, Asymmetric and symmetric rolling of magnesium: Evolution of microstructure, texture and mechanical properties. *Materials Science and Engineering: A*, 2012. **550**: p. 19-30.
73. Hamad, K. and Y.G. Ko, A cross-shear deformation for optimizing the strength and ductility of AZ31 magnesium alloys. *Scientific Reports*, 2016. **6**(1): p. 29954.
74. Kim, W.J., et al., Microstructure and mechanical properties of Mg–Al–Zn alloy sheets severely deformed by asymmetrical rolling. *Scripta Materialia*, 2007. **56**(4): p. 309-312.

75. Wu, D., R.S. Chen, and E.H. Han, Excellent room-temperature ductility and formability of rolled Mg–Gd–Zn alloy sheets. *Journal of Alloys and Compounds*, 2011. **509**(6): p. 2856-2863.
76. Huang, X., K. Suzuki, and N. Saito, Textures and stretch formability of Mg–6Al–1Zn magnesium alloy sheets rolled at high temperatures up to 793K. *Scripta Materialia*, 2009. **60**(8): p. 651-654.
77. Huang, X.S., et al., Influences of Rolling Conditions on Texture and Formability of Magnesium Alloy Sheets. *Materials Science Forum*, 2010. **638-642**: p. 1536-1540.
78. Stanford, N. and M.R. Barnett, Fine grained AZ31 produced by conventional thermo-mechanical processing. *Journal of Alloys and Compounds*, 2008. **466**(1): p. 182-188.
79. Xu, Z., et al., Non-conventional hot rolling for improvement of mechanical properties in binary Mg-alloys. *Mechanics of Materials*, 2021. **164**: p. 104111.
80. Doherty, R.D., et al., Current issues in recrystallization: a review. *Materials Science and Engineering: A*, 1997. **238**(2): p. 219-274.
81. Alaneme, K.K. and E.A. Okotete, Recrystallization mechanisms and microstructure development in emerging metallic materials: A review. *Journal of Science: Advanced Materials and Devices*, 2019. **4**(1): p. 19-33.
82. Bailey, J.E., P.B. Hirsch, and N.F. Mott, The recrystallization process in some polycrystalline metals. 1962. **267**(1328): p. 11-30.

83. Ion, S.E., F.J. Humphreys, and S.H. White, Dynamic recrystallisation and the development of microstructure during the high temperature deformation of magnesium. *Acta Metallurgica*, 1982. **30**(10): p. 1909-1919.
84. Beck, P.A. and P.R. Sperry, Strain Induced Grain Boundary Migration in High Purity Aluminum. 1950. **21**(2): p. 150-152.
85. Huang, K. and R.E. Logé, A review of dynamic recrystallization phenomena in metallic materials. *Materials & Design*, 2016. **111**: p. 548-574.
86. Sakai, T., et al., Dynamic and post-dynamic recrystallization under hot, cold and severe plastic deformation conditions. *Progress in Materials Science*, 2014. **60**: p. 130-207.
87. Miura, H., H. Aoyama, and T.J.N.K.G. Sakai, Effect of grain-boundary misorientation on dynamic recrystallization of Cu-Si bicrystals. 1994. **58**(3): p. 267-275.
88. Wusatowska-Sarnek, A.M., H. Miura, and T. Sakai, Nucleation and microtexture development under dynamic recrystallization of copper. *Materials Science and Engineering: A*, 2002. **323**(1): p. 177-186.
89. Perdrix, C., M. Perrin, and F.J.M.E.S.R.M. Montheillet, Mechanical Behavior and structure development of aluminum during Hot deformation With large Amplitude. 1981: p. 309-320.
90. Montheillet, F., Mechanical and structural behaviour of high stacking fault energy materials submitted to large hot deformation, in *Thermomechanical treatments: theory and applications*. 1981.

91. Gourdet, S. and F. Montheillet, An experimental study of the recrystallization mechanism during hot deformation of aluminium. *Materials Science and Engineering: A*, 2000. **283**(1): p. 274-288.
92. Humphreys, F.J.A.M., The nucleation of recrystallization at second phase particles in deformed aluminium. 1977. **25**(11): p. 1323-1344.
93. Humphreys, F. and M.J.O.E. Hatherly, Chapter 7-Recrystallization of Single-Phase Alloys, *Recrystallization and Related Annealing Phenomena*. 2004.
94. Barnett, M.J.J.o.L.M., Influence of deformation conditions and texture on the high temperature flow stress of magnesium AZ31. 2001. **1**(3): p. 167-177.
95. Barnett, M.R.J.M.t., Quenched and annealed microstructures of hot worked magnesium AZ31. 2003. **44**(4): p. 571-577.
96. Barnett, M., et al., Influence of grain size on hot working stresses and microstructures in Mg-3Al-1Zn. 2004. **51**(1): p. 19-24.
97. Beer, A.G. and M.R. Barnett, Influence of initial microstructure on the hot working flow stress of Mg-3Al-1Zn. *Materials Science and Engineering: A*, 2006. **423**(1): p. 292-299.
98. Del Valle, J. and O. Ruano, Influence of texture on dynamic recrystallization and deformation mechanisms in rolled or ECAPed AZ31 magnesium alloy. *Materials Science and Engineering: A*, 2008. **487**: p. 473-480.
99. Galiyev, A., R. Kaibyshev, and G. Gottstein, Correlation of plastic deformation and dynamic recrystallization in magnesium alloy ZK60. *Acta Materialia*, 2001. **49**(7): p. 1199-1207.

100. Nayeb-Hashemi, A.J.A.I., Metals Park, Ohio 44073, USA, . 370, Phase diagrams of binary magnesium alloys. 1988.
101. Villars, P. and L.J.A.S.o.M. Calvert, Cleveland, OH, Pearson's handbook of crystallographic data for intermediate phases. 1985.
102. Clark, J.J.A.M., Age hardening in a Mg-9 wt.% Al alloy. 1968. **16**(2): p. 141-152.
103. Hutchinson, C.R., J.F. Nie, and S. Gorsse, Modeling the precipitation processes and strengthening mechanisms in a Mg-Al-(Zn) AZ91 alloy. Metallurgical and Materials Transactions A, 2005. **36**(8): p. 2093-2105.
104. Bettles, C.J., Effects of trace additions of copper on the ageing behaviour of the magnesium alloy AZ91E. 1998; ; Werkstoff-Informationsgesellschaft mbH, Frankfurt am Main (Germany) %J. Medium: X; Size: Pages: 265-270; (747 p).
105. Celotto, S., TEM study of continuous precipitation in Mg–9 wt%Al–1 wt%Zn alloy. Acta Materialia, 2000. **48**(8): p. 1775-1787.
106. Nie, J.F., et al., Characterisation of precipitate phases in magnesium alloys using electron microdiffraction. Micron, 2001. **32**(8): p. 857-863.
107. Duly, D. and Y.J.A.m.e.m. Brechet, Nucleation mechanism of discontinuous precipitation in Mg–Al alloys and relation with the morphology. 1994. **42**(9): p. 3035-3043.
108. Braszczyńska-Malik, K.N., Discontinuous and continuous precipitation in magnesium–aluminium type alloys. Journal of Alloys and Compounds, 2009. **477**(1): p. 870-876.

109. Duly, D., W.Z. Zhang, and M. Audier, High-resolution electron microscopy observations of the interface structure of continuous precipitates in a Mg-Al alloy and interpretation with the O-lattice theory. *Philosophical Magazine A*, 1995. **71**(1): p. 187-204.
110. Zhang, M., et al., Interpretation of precipitation crystallography of Mg₁₇Al₁₂ in a Mg-Al alloy in terms of singular interfacial structure. 2005. **36**(7): p. 1681-1688.
111. P.V.Padfield, *Metallography and Microstructures*, Vol 9, ASM International. 2004. **3**: p. 281-293.
112. Ma, X.L., et al., Dynamic precipitation and recrystallization in Mg-9wt.%Al during equal-channel angular extrusion: A comparative study to conventional aging. *Acta Materialia*, 2019. **172**: p. 185-199.
113. Celikin, M., et al., Dynamic co-precipitation of α -Mn/Mg₁₂Ce in creep resistant Mg-Sr-Mn-Ce alloys. 2018. **719**: p. 199-205.
114. Guo, F., et al., Strain-induced dynamic precipitation of Mg₁₇Al₁₂ phases in Mg-8Al alloys sheets rolled at 748 K. 2015. **636**: p. 516-521.
115. Xiao, H., et al., Dynamic precipitation in a Mg-Gd-Y-Zr alloy during hot compression. *Materials Science and Engineering: A*, 2015. **645**: p. 241-247.
116. Aboufadel, H., et al., Dynamic strain aging studied at the atomic scale. 2015. **86**: p. 34-42.
117. Prameela, S.E., et al., Deformation assisted nucleation of continuous nanoprecipitates in Mg-Al alloys. 2020. **9**: p. 100583.

118. Köster, U.J.M.S., Recrystallization involving a second phase. 1974. **8**(1): p. 151-160.
119. Hadorn, J.P., et al., Role of solute in the texture modification during hot deformation of Mg-rare earth alloys. 2012. **43**(4): p. 1347-1362.
120. Jin, Z.-Z., et al., Effects of Mg₁₇Al₁₂ second phase particles on twinning-induced recrystallization behavior in Mg–Al–Zn alloys during gradient hot rolling. 2019. **35**(9): p. 2017-2026.
121. Maitland, T. and S. Sitzman, Electron backscatter diffraction (EBSD) technique and materials characterization examples. Vol. 14. 2007: Springer Berlin.
122. Khosravani, A., A. Cecen, and S. Kalidindi, Development of high throughput assays for establishing process- structure-property linkages in multiphase polycrystalline metals: Application to dual-phase steels. *Acta Materialia*, 2017. **123**: p. 55-69.
123. Cho, J.H., et al., Determination of a mean orientation in electron backscatter diffraction measurements. 2005. **36**: p. 3427-3438.
124. Wei, Q., L.J. Kecskes, and K.T. Ramesh, Effect of Low-Temperature Rolling on the Propensity to Adiabatic Shear Banding of Commercial Purity Tungsten. *Materials Science and Engineering A*, 2013. **578**: p. 394-401.
125. Wei, Q. and X. Chen, Heterogeneously stacked multilayered metallic structures with adiabatic shear localization under uniaxial dynamic compression, U.P. Office, Editor. 2020: USA. p. Patent Number: 10718597.

126. Wei, Q. and L.J. Kecskes, Effect of Low-Temperature Rolling on the Tensile Behavior of Commercially Pure Tungsten. *Materials Science and Engineering A*, 2008. **491**: p. 62-69.
127. Chen, Z., et al., Microstructure and helium irradiation performance of high purity tungsten processed by cold rolling. *Journal of Nuclear Materials*, 2016. **479**: p. 418-425.
128. Physical Properties of Metals and the Periodic Table, in *Metallurgy for the Non-Metallurgist*, A.C. Reardon, Editor. 2011, ASM International. p. 0.
129. Ghosh, S. and K.J.A.M. Bhattacharya, Influence of thermomechanical loads on the energetics of precipitation in magnesium aluminum alloys. 2020. **193**: p. 28-39.
130. Robson, J.J.A.m., Modeling competitive continuous and discontinuous precipitation. 2013. **61**(20): p. 7781-7790.
131. Xie, K.Y., et al., Understanding the interaction of extension twinning and basal-plate precipitates in Mg-9Al using precession electron diffraction. *Materialia*, 2021. **15**: p. 101044.
132. Ma, X., et al., Effect of basal precipitates on extension twinning and pyramidal slip: A micro-mechanical and electron microscopy study of a Mg–Al binary alloy. 2020. **189**: p. 35-46.
133. Gharghouri, M., G. Weatherly, and J.J.P.M.A. Embury, The interaction of twins and precipitates in a Mg-7.7 at.% Al alloy. 1998. **78**(5): p. 1137-1149.
134. Máthis, K., et al., Microstructure and mechanical behavior of AZ91 Mg alloy processed by equal channel angular pressing. 2005. **394**(1-2): p. 194-199.

135. Tork, N.B., et al., Microstructure and texture characterization of Mg–Al and Mg–Gd binary alloys processed by simple shear extrusion. 2019. **8**(1): p. 1288-1299.
136. Humphreys, F.J. and M. Hatherly, Recrystallization and related annealing phenomena. 2012: Elsevier.
137. Lennon, A.M. and K.T. Ramesh, A technique for measuring the dynamic behavior of materials at high temperatures. *International Journal of Plasticity*, 1998. **14**(12): p. 1279-1292.
138. Kolsky, H.J.P.o.t.p.s.S.B., An investigation of the mechanical properties of materials at very high rates of loading. 1949. **62**(11): p. 676.
139. Chen, W.W. and B. Song, Split Hopkinson (Kolsky) bar: design, testing and applications. 2010: Springer Science & Business Media.
140. Zhao, H. and G. Gary, On the use of SHPB techniques to determine the dynamic behavior of materials in the range of small strains. *International Journal of Solids and Structures*, 1996. **33**(23): p. 3363-3375.
141. Meyers, M.A., Dynamic behavior of materials by Marc Andre Meyers. 1994, New York: John Wiley & Sons.
142. Wei, Q., et al., Insights from the MEDE program: An overview of microstructure-property linkages in the dynamic behaviors of magnesium alloys. 2021: p. 104084.
143. Yu, X., et al., Microstructure and mechanical behavior of ECAP processed AZ31B over a wide range of loading rates under compression and tension. *Mechanics of Materials*, 2015. **86**: p. 55-70.

144. Shen, J., et al., Effect of strain rate on the mechanical properties of magnesium alloy AMX602. *Materials Science and Engineering a-Structural Materials Properties Microstructure and Processing*, 2016. **649**: p. 338-348.
145. Shen, J., et al., Mechanical Behavior of a Lanthanum-doped Magnesium Alloy at Different Strain Rates. *Materials Science and Engineering A*, 2015. **626**: p. 108-121.
146. Hao, M., et al., Texture evolution induced by twinning and dynamic recrystallization in dilute Mg-1Sn-1Zn-1Al alloy during hot compression. 2020. **8**(3): p. 899-909.
147. Ponge, D. and G.J.A.M. Gottstein, Necklace formation during dynamic recrystallization: mechanisms and impact on flow behavior. 1998. **46**(1): p. 69-80.
148. Barnett, M.R., et al., Influence of grain size on hot working stresses and microstructures in Mg-3Al-1Zn. *Scripta Materialia*, 2004. **51**(1): p. 19-24.
149. Spigarelli, S., et al., Analysis of high-temperature deformation and microstructure of an AZ31 magnesium alloy. *Materials Science and Engineering: A*, 2007. **462**(1): p. 197-201.
150. Zhang, J., et al., An investigation of dynamic recrystallization behavior of ZK60-Er magnesium alloy. 2014. **612**: p. 253-266.
151. Chang, T.-C., et al., Grain refining of magnesium alloy AZ31 by rolling. 2003. **140**(1-3): p. 588-591.
152. Mukai, T., et al., Ductility enhancement in AZ31 magnesium alloy by controlling its grain structure. 2001. **45**(1): p. 89-94.

153. Wang, Y.-p., et al., Effect of extrusion ratio on the microstructure and texture evolution of AZ31 magnesium alloy by the staggered extrusion (SE). *Journal of Magnesium and Alloys*, 2020. **8**(4): p. 1304-1313.
154. Pérez-Prado, M.T. and O.J.S.m. Ruano, Grain refinement of Mg–Al–Zn alloys via accumulative roll bonding. 2004. **51**(11): p. 1093-1097.
155. Wilson, D.J.J.I.M., Ductility of polycrystalline magnesium below 300 K. 1970. **98**(5): p. 133-143.
156. Liu, H., et al., Texture of AZ31B magnesium alloy sheets produced by differential speed rolling technologies. 2012. **31**(5): p. 415-419.
157. Ren, X., et al., Evolution of microstructure, texture, and mechanical properties in a twin-roll cast AA6016 sheet after asymmetric rolling with various velocity ratios between top and bottom rolls. 2020. **788**: p. 139448.
158. Ren, X., et al., Influence of shear deformation during asymmetric rolling on the microstructure, texture, and mechanical properties of the AZ31B magnesium alloy sheet. 2021. **800**: p. 140306.
159. Liu, X. and J.J.S.r. Wang, Low-energy, mobile grain boundaries in magnesium. 2016. **6**(1): p. 1-8.
160. Al-Samman, T., G.J.M.S. Gottstein, and E. A, Dynamic recrystallization during high temperature deformation of magnesium. 2008. **490**(1-2): p. 411-420.
161. Li, B., et al., Structure of grain boundaries with $30^\circ[0\ 0\ 0\ 1]$ misorientation in dynamically recrystallized magnesium alloys. 2015. **101**: p. 175-180.

162. Barnett, M.R., et al., Texture selection mechanisms in uniaxially extruded magnesium alloys. *Scripta Materialia*, 2010. **63**(7): p. 721-724.
163. Jiang, M., et al., Unveiling the formation of basal texture variations based on twinning and dynamic recrystallization in AZ31 magnesium alloy during extrusion. 2018. **157**: p. 53-71.
164. Jiang, M., et al., Twinning, recrystallization and texture development during multi-directional impact forging in an AZ61 Mg alloy. 2015. **650**: p. 399-409.
165. Martin, É. and J.J.J.A.M. Jonas, Evolution of microstructure and microtexture during the hot deformation of Mg–3% Al. 2010. **58**(12): p. 4253-4266.
166. Zhao, F., et al., Dynamic compressive behavior and damage mechanism of cast magnesium alloy AZ91 [J]. 2009. **19**(7): p. 1163-1168.
167. Zhao, F., et al., Compressive deformation behavior of AZ31 magnesium alloy under quasi-static and dynamic loading. *Transactions of Nonferrous Metals Society of China*, 2010. **20**(7): p. 1316-1320.
168. Ulacia, I., et al., Tensile characterization and constitutive modeling of AZ31B magnesium alloy sheet over wide range of strain rates and temperatures. 2011. **211**(5): p. 830-839.
169. Barnett, M.J.M.S. and E. A, Twinning and the ductility of magnesium alloys: Part I:“Tension” twins. 2007. **464**(1-2): p. 1-7.
170. Korla, R. and A.H.J.S.M. Chokshi, Strain-rate sensitivity and microstructural evolution in a Mg–Al–Zn alloy. 2010. **63**(9): p. 913-916.

171. Karimi, E., et al., Instantaneous strain rate sensitivity of wrought AZ31 magnesium alloy. 2013. **49**: p. 173-180.
172. Zhao, X., et al., An Investigation on Microstructure, Texture and Mechanical Properties of AZ80 Mg Alloy Processed by Annular Channel Angular Extrusion. 2019. **12**(6): p. 1001.
173. Meyers, M., O. Vöhringer, and V.J.A.m. Lubarda, The onset of twinning in metals: a constitutive description. 2001. **49**(19): p. 4025-4039.
174. Chaudhuri, A., et al., Understanding the Mechanism of Dynamic Recrystallization During High-Temperature Deformation in Nb-1Zr-0.1 C Alloy. 2019. **28**(1): p. 448-462.
175. Rey, C. and A.J.A.M. Zaoui, Grain boundary effects in deformed bicrystals. 1982. **30**(2): p. 523-535.
176. Šittner, P. and V.J.A.M. Paidar, Observation and interpretation of grain boundary compatibility effects in Fe-3.3 wt% Si bicrystals. 1989. **37**(7): p. 1717-1726.
177. Takasugi, T., O. Izumi, and N.J.J.o.M.S. Fat-Halla, Activated slip systems during yielding of α - β brass two-phase bicrystals. 1978. **13**(9): p. 2013-2021.
178. Kobayashi, T., et al., Grain size dependence of active slip systems in an AZ31 magnesium alloy. 2003. **67**(4): p. 149-152.
179. Koike, J.J.M. and M.T. A, Enhanced deformation mechanisms by anisotropic plasticity in polycrystalline Mg alloys at room temperature. 2005. **36**(7): p. 1689-1696.

180. Somekawa, H., T.J.M. Mukai, and M.T. A, Hall–Petch breakdown in fine-grained pure magnesium at low strain rates. 2015. **46**(2): p. 894-902.
181. Huang, K., et al., The double-edge effect of second-phase particles on the recrystallization behaviour and associated mechanical properties of metallic materials. 2018. **92**: p. 284-359.
182. Nes, E., N. Ryum, and O.J.A.M. Hunderi, On the Zener drag. 1985. **33**(1): p. 11-22.
183. Watanabe, H., et al., Grain Size Control of Commercial Wrought Mg-Al-Zn Alloys Utilizing Dynamic Recrystallization. MATERIALS TRANSACTIONS, 2001. **42**(7): p. 1200-1205.
184. Dogan, E., et al., Dynamic precipitation in Mg-3Al-1Zn alloy during different plastic deformation modes. 2016. **116**: p. 1-13.
185. Mabuchi, M., K. Kubota, and K.J.M.T. Higashi, JIM, New recycling process by extrusion for machined chips of AZ91 magnesium and mechanical properties of extruded bars. 1995. **36**(10): p. 1249-1254.
186. Lai, W.-J., et al., Aging behaviour and precipitate morphologies in Mg–7.7 Al–0.5 Zn–0.3 Mn (wt.%) alloy. 2009. **476**(1-2): p. 118-124.
187. Humphreys, F.J. and M.G. Ardakani, Grain boundary migration and Zener pinning in particle-containing copper crystals. Acta Materialia, 1996. **44**(7): p. 2717-2727.
188. Peng, P., et al., Role of second phases and grain boundaries on dynamic recrystallization behavior in ZK60 magnesium alloy. 2021. **861**: p. 157958.

189. Changizian, P., et al., On the recrystallization behavior of homogenized AZ81 magnesium alloy: The effect of mechanical twins and γ precipitates. 2012. **558**: p. 44-51.
190. Watanabe, H., et al., Grain size control of commercial wrought Mg-Al-Zn alloys utilizing dynamic recrystallization. 2001. **42**(7): p. 1200-1205.
191. Xu, S., et al., Dynamic microstructural changes in Mg-9Al-1Zn alloy during hot compression. 2009. **61**(3): p. 249-252.
192. Zener, C.J.T.A., quoted by CS Smith. 1948. **175**: p. 15.
193. Chun, Y., C.J.M.S. Davies, and E. A, Twinning-induced negative strain rate sensitivity in wrought Mg alloy AZ31. 2011. **528**(18): p. 5713-5722.
194. Prasad, K.E., et al., The dynamic flow and failure behavior of magnesium and magnesium alloys. 2014. **66**(2): p. 291-304.
195. Hollomon, J.H.J.A.T., Tensile deformation. 1945. **12**(4): p. 1-22.
196. Chino, Y., et al., Mechanical anisotropy due to twinning in an extruded AZ31 Mg alloy. 2008. **485**(1-2): p. 311-317.
197. Proust, G., et al., Modeling the effect of twinning and detwinning during strain-path changes of magnesium alloy AZ31. 2009. **25**(5): p. 861-880.
198. Tahreen, N., et al., Effects of aluminum content and strain rate on strain hardening behavior of cast magnesium alloys during compression. 2014. **594**: p. 235-245.
199. Wright, T.W. and J.W. Walter, On stress collapse in adiabatic shear bands. *Journal of the Mechanics and Physics of Solids*, 1987. **35**(6): p. 701-720.

200. Lentz, M., et al., Strength and ductility with $\{10\bar{1}1\}$ — $\{10\bar{1}2\}$ double twinning in a magnesium alloy. 2016. **7**(1): p. 1-7.
201. Basu, I. and T.J.A.M. Al-Samman, Twin recrystallization mechanisms in magnesium-rare earth alloys. 2015. **96**: p. 111-132.
202. Guan, D., et al., Twin recrystallization mechanisms and exceptional contribution to texture evolution during annealing in a magnesium alloy. 2017. **126**: p. 132-144.
203. Molodov, K.D., et al., Mechanisms of exceptional ductility of magnesium single crystal during deformation at room temperature: Multiple twinning and dynamic recrystallization. 2014. **76**: p. 314-330.
204. Allain-Bonasso, N., et al., A study of the heterogeneity of plastic deformation in IF steel by EBSD. *Materials Science and Engineering: A*, 2012. **548**: p. 56-63.
205. Cao, Y., et al., An electron backscattered diffraction study on the dynamic recrystallization behavior of a nickel–chromium alloy (800H) during hot deformation. 2013. **585**: p. 71-85.
206. Mandal, S., et al., A study on microstructural evolution and dynamic recrystallization during isothermal deformation of a Ti-modified austenitic stainless steel. 2011. **42**(4): p. 1062-1072.
207. Miller, V.M., T.M.J.M. Pollock, and M.T. A, Texture modification in a magnesium-aluminum-calcium alloy during uniaxial compression. 2016. **47**(4): p. 1854-1864.

208. Yin, X.-Q., et al., Mechanism of continuous dynamic recrystallization in a 50Ti-47Ni-3Fe shape memory alloy during hot compressive deformation. 2017. **693**: p. 426-431.
209. Hadadzadeh, A., et al., A new grain orientation spread approach to analyze the dynamic recrystallization behavior of a cast-homogenized Mg-Zn-Zr alloy using electron backscattered diffraction. 2018. **709**: p. 285-289.
210. Asgari, H., et al., Texture evolution and dynamic mechanical behavior of cast AZ magnesium alloys under high strain rate compressive loading. 2014. **61**: p. 26-34.
211. Baker, I. and J.J.J.o.M.S. Martin, The effect of particle size and spacing on the retardation of recrystallization in two-phase copper crystals. 1980. **15**(6): p. 1533-1538.
212. Chan, H.M. and F.J. Humphreys, The recrystallisation of aluminium-silicon alloys containing a bimodal particle distribution. *Acta Metallurgica*, 1984. **32**(2): p. 235-243.
213. Nes, E., On the effect of finely dispersed second-phase particles on nucleation in recrystallization. *Scripta Metallurgica*, 1976. **10**(11): p. 1025-1028.
214. Wert, J.A. and L.J.M.T.A. Austin, Modeling of thermomechanical processing of heat-treatable aluminum alloys. 1988. **19**(3): p. 617-625.
215. Robson, J.D., N. Stanford, and M.R.J.A.m. Barnett, Effect of precipitate shape on slip and twinning in magnesium alloys. 2011. **59**(5): p. 1945-1956.

216. Nie, J.-F.J.M. and M.T. A, Precipitation and hardening in magnesium alloys. 2012. **43**(11): p. 3891-3939.
217. Nie, J.F.J.S.M., Effects of precipitate shape and orientation on dispersion strengthening in magnesium alloys. 2003. **48**(8): p. 1009-1015.
218. Rabkin, E., W. Gust, and Y. Estrin, On dynamic segregation in the discontinuous precipitation reaction. *Scripta Materialia*, 1997. **37**(1): p. 119-124.
219. Wang, F., et al., Effect of precipitate shape and orientation on Orowan strengthening of non-basal slip modes in hexagonal crystals, application to magnesium alloys. 2016. **666**: p. 114-122.
220. Sabzi, H.E., et al., The sequential twinning-transformation induced plasticity effects in a thermomechanically processed high Mn austenitic steel. 2018. **725**: p. 242-249.
221. Cizek, P. and M.R. Barnett, Characteristics of the contraction twins formed close to the fracture surface in Mg–3Al–1Zn alloy deformed in tension. *Scripta Materialia*, 2008. **59**(9): p. 959-962.
222. Jain, A., et al., Grain size effects on the tensile properties and deformation mechanisms of a magnesium alloy, AZ31B, sheet. 2008. **486**(1-2): p. 545-555.
223. Prakash, G., et al., Tensile, Compressive, and Flexural Behaviors of Al5052-H32 in a Wide Range of Strain Rates and Temperatures. 2020. **32**(5): p. 04020090.

224. Yu, X., et al. Quasi-static and Dynamic Compressive Properties of AZ31 Magnesium Alloy Processed by Equal Channel Angular Pressing. in *Applied Mechanics and Materials*. 2014. Trans Tech Publ.
225. Wang, H., et al., Strain rate sensitivities of deformation mechanisms in magnesium alloys. *International Journal of Plasticity*, 2018. **107**.
226. Klinger, L., Y. Brechet, and G.J.A.m. Purdy, On velocity and spacing selection in discontinuous precipitation—I. Simplified analytical approach. 1997. **45**(12): p. 5005-5013.
227. Klinger, L., Y. Bréchet, and D. Duly, On the influence of non-steady state velocity on interlamellae concentration profiles in discontinuous precipitation. *Scripta Materialia*, 1997. **37**(8): p. 1237-1242.